Nanoscale nonlinear optics with $LaAlO_3/SrTiO_3$ junctions

by

Erin Sheridan

Bachelor of Science in Physics and Mathematics, Boston College, 2016

Submitted to the Graduate Faculty of the

Dietrich School of Arts and Sciences in partial fulfillment

of the requirements for the degree of

Doctor of Philosophy

University of Pittsburgh

2021

UNIVERSITY OF PITTSBURGH

DIETRICH SCHOOL OF ARTS AND SCIENCES

This dissertation was presented

by

Erin Sheridan

It was defended on

November 16, 2021

and approved by

Susan Fullerton, Associate Professor, Department of Chemical and Petroleum Engineering

Hrvoje Petek, Mellon Professor, Department of Physics and Astronomy

Andrew Mugler, Assistant Professor, Department of Physics and Astronomy

Arthur Kosowsky, Professor, Department of Physics and Astronomy

Dissertation Director: Jeremy Levy, Distinguished Professor, Department of Physics and Astronomy

Nanoscale nonlinear optical spectroscopy with junctions defined at the $LaAlO_3/SrTiO_3$ interface

Erin Sheridan, PhD

University of Pittsburgh, 2021

Continued progress in nanometer-scale research and technologies relies on our ability to characterize and control the optical and electronic behaviors of nanometer-scale objects over a broad range of frequencies. This thesis focuses on the development of a one-of-a-kind molecular-scale nonlinear optical platform that can electronically contact nanoscale analytes and probe their optical responses over an extremely large range of frequencies. These devices consist of 10-nanometer scale nanojunctions situated within the interface of the $LaAlO_3/SrTiO_3$ (LAO/STO) heterostructure.

This dissertation begins with an introduction to LAO/STO in Chapter 1.0. This is followed by a review of the experimental setup and methods used in this work in Chapter 2.0. Chapter 3.0 lays out an overview of the optical response of LAO/STO nanojunctions, and includes the first original work of this thesis (Section 3.2), wherein I describe two-wave-mixing experiments utilizing a ultrafast pulse shaping setup. A difference frequency generation response ranging from 1 to >100 THz is observed, demonstrating the ultra-broadband generation and detection capabilities of LAO/STO nanojunctions.

Next, I describe results obtained when these devices are used to probe the nonlinear optical response of graphene (Chapter 4.0) and graphene nanoribbons (Chapter 5.0). Time-domain photovoltage measurements reveal >99.9% absorption of light in graphene in the visible-to-near infrared range of the electromagnetic spectrum, where undoped graphene is typically transparent. When these absorption features appear, the nonlinear optical response of the graphene is greatly enhanced, suggesting the existence of high-energy plasmons. Similar results are observed in

graphene nanoribbons that are deposited on LAO using an AFM tip then integrated into a nanojunction device, revealing the confined nature of the graphene response. Finally, in Chapter 6.0. I briefly describe experiments probing the interaction of two graphene/LAO/STO nanojunctions. The work of this dissertation paves the way for new experiments, outlined in Chapter 7.0.

Table of Contents

List of Tables

List of Figures

List of Equations

Preface

— To my husband, Peter —

I joined the Levy Lab to begin my doctoral research on 31 May 2016, just one week after I graduated from college. I moved from Boston to Pittsburgh immediately— almost impulsively— as I couldn't wait to begin. And no wonder. These five and a half years have been filled to the brim with more challenges, more learning, more fun, more love, and more growth than any other years of my life. I came to this city a hesitant college kid, and I leave it a confident woman, a physicist, a wife and a mother. Pittsburgh has become my home, and it breaks my heart to leave.

We human beings are made to live in community with one another, and no great accomplishment is achieved without the support of a community. As such, I owe my success to a multitude of people. First, I thank my lab-mates, who trained me, provided me with samples, and extended countless kindnesses over the years; my doctoral advisor, Jeremy, who built what is the most unique physics research program that I have ever known; and my "mini boss" Patrick, whose daily efforts keep equipment operational and experiments running, and whose kind demeanor calms even the most anxious grad student. I thank my fellow graduate students who have helped me survive the rigors of the program, and the department faculty and staff for teaching and guiding me, especially Leyla Hirschfeld and my PhD committee members. As the daughter of a janitor, I cannot forget to thank the maintenance and facilities staff who provide us all with an environment in which to do science and keep it clean and operational.

Special thanks are due to Ken Burch, my undergraduate research advisor, who introduced me to physics research and provided me with the experiences and opportunities which allowed me to go to graduate school. He remains a dear friend and mentor.

I wish to thank my family: my parents, Pam and Bill; my stepfather Harry; my stepmother Mary; my brother Will and sister Maegan; my grandparents, Mary Jane, Jack (deceased), Bill (deceased), Lorraine, Nora and Paul (deceased); my aunts and uncles, cousins, and in-laws, in particular Auntie Jackie, Uncle Pat and Uncle Jimmy, and Rick (deceased), Rachael, Sara, Kevin, and Aunt Pat. You raised me and made me who I am.

I do not count myself among the social butterflies, and I hold only few friends dear, the foremost of whom are Abby, Justin, Aditi, Anna, Aja and Alec. It takes great virtue to endure as a friend of mine. I also thank those not listed here for the sake of brevity, and in a special way my friends and the clergy of the Roman Catholic community of Pittsburgh. I also wish to thank my pets: first, my cats, Porthos and Athos, and my dog Savannah (deceased).

No acknowledgement compares to that deserved by my husband, Peter. Not only has he supported my physics ambitions from the beginning; he relocated to Pittsburgh to build a life with me as I worked my way through graduate school. He married me and raised a son with me. Even when the COVID-19 pandemic shut the world down two weeks before— and lost him his job just a week before — my son was born. Peter has made many sacrifices so that we could build a family while I finished school; from nights and weekends spent apart as I worked, to caring for my son so that I could analyze data or run to the lab and realign my laser. He has read many drafts of manuscripts and listened to numerous practice talks given on the living room TV. He has talked me through anxiety attacks and fears that I'd never be able to finish school. He woke up early and worked long days to financially support my family, and also found a way to do most of the

household cooking, so that I could fulfill my childhood dream. I wish that this PhD could be awarded to him as well. Peter: I could never properly thank you. You are the best man that I have ever known.

On that note, I want to thank my son, Richard: for being alive, for being you, and for the purest love. You taught me how to be strong, humble, flexible and resilient. Becoming a mother while in grad school has been incredibly difficult and isolating, but I would never, ever, ever do it differently. My beautiful boy; you are the light of my life. I am so very proud of you, and I am so thankful for the opportunity to be your mother and to watch you grow. I love you.

For a Catholic, no acknowledgement is complete without expressing thanks to God—Father, Son and Holy Spirit— to Jesus Christ, his Church, and to His communion of angels and saints, and to all of those who have leant me their prayers. In a special way I dedicate to this work to my guardian angel, to the Most Blessed Virgin Mary, to Saint Thomas Aquinas, the patron of students, and finally to Saint Albert the Great, the patron of scientists, to whom I pray as I began experiments each day, and whose image I've worn around my neck for five years. I am a poor sinner, and all of my virtues and accomplishments come to me as gifts from God.

1.0 Introduction

The aim of this large introduction chapter is to provide an overview of the properties of the $LaAlO_3/SrTiO_3$ heterostructure.

1.1.1 $SrTiO_3$ Crystal Structure

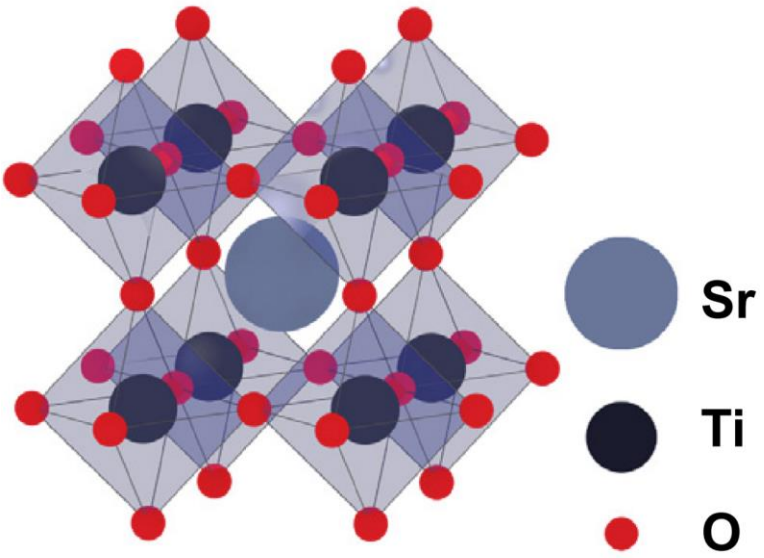

Figure 1: STO crystal structure. Adapted from Pai *et al.*[1]

Strontium titanate, $SrTiO_3$ (STO), is a complex oxide material that has a perovskite crystal structure. Each unit cell has strontium (Sr) atoms at its corners, a titanium (Ti) atom in the center, and oxygen (O) atoms located in the center of each face of the Sr cube which form an octahedral cage. At room temperature, $SrTiO_3$ has an idealized cubic structure (space group $Pm\bar{3}m$) with lattice parameter a = 0.3905 nm, as shown in Figure 2. Under stress or change of temperature, the $SrTiO_3$ lattice can deform from the ideal cubic structure. Bulk STO is a band insulator with an

indirect bandgap transition from R → Γ of 3.25 eV and a direct bandgap from Γ → Γ of 3.75 eV[2] in momentum space, making the pristine crystal transparent and colorless. Because of its cubic structure, almost identical refractive index and more than four-fold higher dispersion compared to diamond, STO was once a widely used substitute gemstone.

At 105 K, STO undergoes a cubic-to-tetragonal antiferrodistortive (AFD) transition, where nearby oxygen octahedra rotate in opposite directions, leading to a reduced-symmetry tetragonal lattice structure[3-6]. Domains with tetragonal orientations along x-, y- or z-axis can form within the bulk STO, resulting in ferroelastic domain boundaries. These domains disappear as the sample is warmed above T_{AFD} and typically form a different domain pattern upon temperature cycling. The cubic-to-tetragonal transition can also be triggered by stress and pressure and can be affected by both defects[7] and doping[8]. Recent studies have suggested that these naturally formed domain boundaries could potentially play an important role in the inhomogeneous transport properties of STO[9,10].

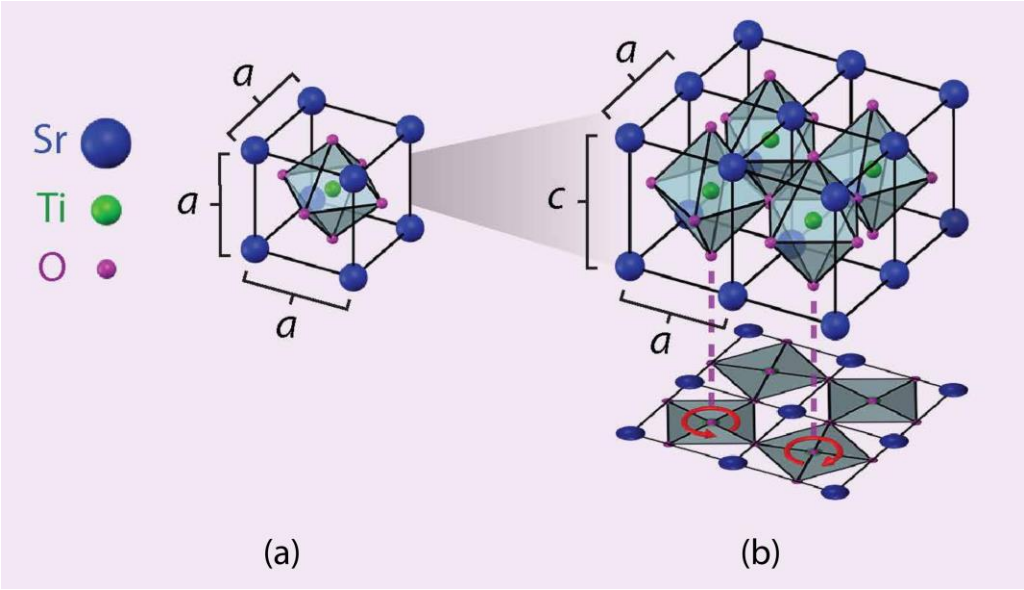

Figure 2: Ferroelstaic transition in STO. (a) Cubic structure and (b) distortion whch causes the cubic-to-tetragonal transition. Adapred from Pai et al.[1]

1.1.2 $SrTiO_3$ Electronic Structure

STO is a band insultor, as described above. It can be n-type doped with Nb, La, or oxygen vacancies. Its valence band is mainly composed of the $2p$ orbitals of oxygen atoms, while the conduction band is mainly composed of the Ti $3d$ orbitals[11]. In the cubic structural phase, the $3d$ orbitals split into t_{2g} and e_g,. DFT calculations of the band structure reveal[12] that the d_{xy}, d_{yz}, and d_{xz} orbitals of the t_{2g} bands are degenerate at the conduction band minimum, i.e. the Γ point. The t_{2g} manifold is expected to split further, due to the AFD transition and atomic spin–orbit coupling, with an expected energy scale ranging from a few meV to tens of meV. The details of the band structure are still difficult to obtain experimentally, in part because important features have energy scales of about a few meV, which is too small for the usual techniques, such as ARPES, to resolve.

1.1.2.1 **STO optical properties**

In addition to many intriguing electronic properties, STO exhibits interesting and important optical properties as well. Bulk STO is centrosymmetric, and thus has a zero second-order nonlinear susceptibility unless the inversion symmetry is broken. Symmetry breaking can occur at the surface or interfaces, for example. The third-order nonlinear susceptibility in STO has been reported to be exceedingly large, likely the largest among many solid-state materials[13], making STO a promising platform for realizing nonlinear optical applications.

1.1.3 STO- based heterostructures and nanostructures

STO has a lattice constant that is closely matched lattice to most perovskite oxides. This property enables STO to serve as a universal substrate for growing various complex oxide heterostructures. Emergent properties rising from the confinement at the oxide interfaces, as well as the inherited rich and exotic physics from the STO substrate, have attracted intense research interest in the past few decades. As such, STO-based heterostructures and nanostructures marry two major fields of study within condensed matter physics: those of complex oxides and of semiconductor interfaces and nanostructures[1].

The demonstration of $LaTiO_3/SrTiO_3$ (LAO/STO) heterostructures grown with unit-cell precision[14] represented a big step forward in the field. $SrTiO_3$-based heterostructure growth was also advanced by the crucial development of surface termination engineering techniques. These enabled growth of a wide variety of oxide thin films derived from bulk precursors[15]. Additional examples of STO-based heterostructures include $CaZrO_3/SrTiO_3$[16,17], γ-$Al_2O_3/SrTiO_3$[18], $SrRuO_3/SrTiO_3$[19] and $GdTiO_3/SrTiO_3$[20], among others.

1.1.4 LAO/STO Heterostructure

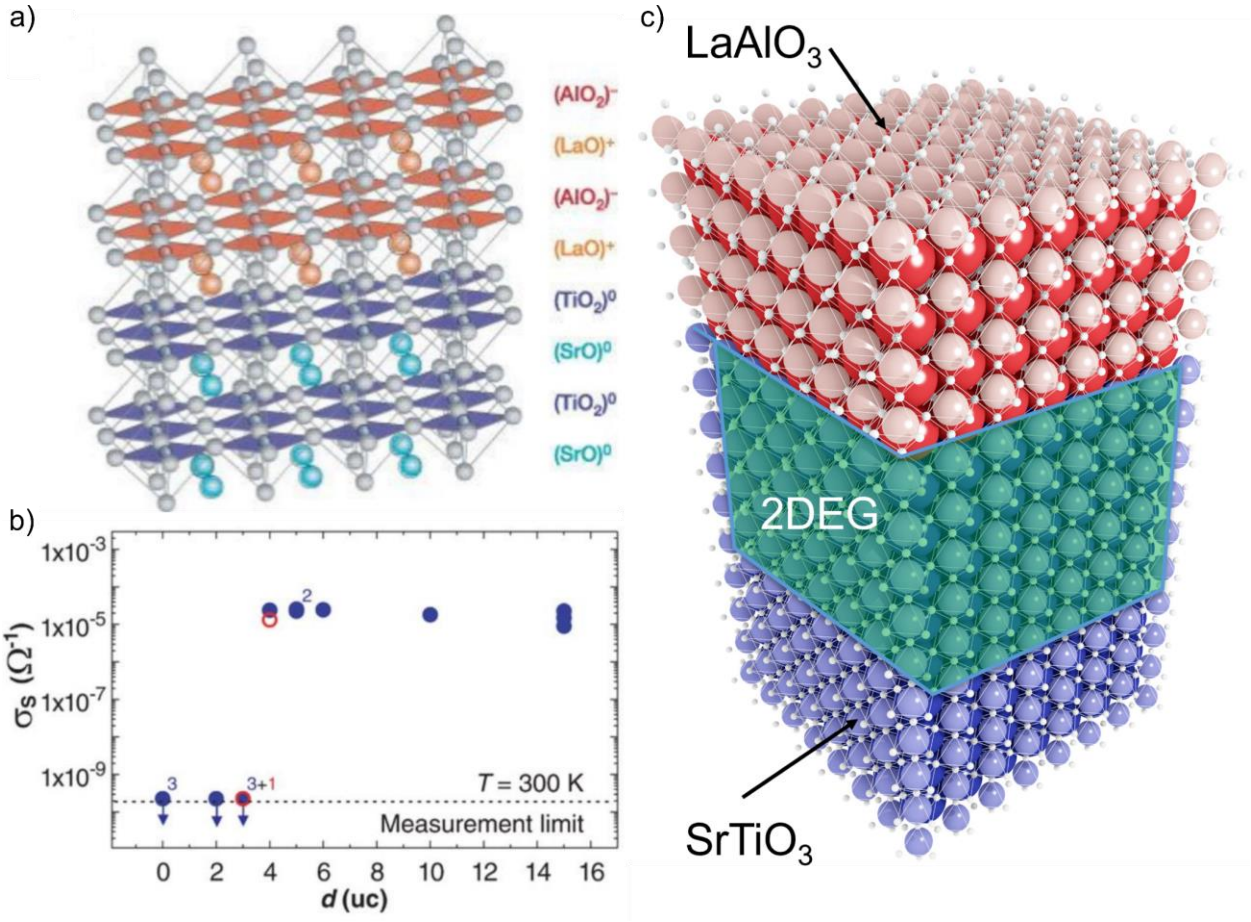

Figure 3: LAO/STO heterostructure. (a) Side view of heterostructure composition. (b) Measured conductivity of the interface as a function of the Lao layer thickness, showing a sharp jump at 4 unit cells. (c) Perspective of heterostructure with the 2DEG shown emerging ~10 nm into the STO layer.

Lanthanum aluminate, $LaAlO_3$ (LAO) is a perovskite oxide with a lattice constant of 3.789 Å, which is closely matched to STO. When LAO is grown on (001) TiO_2-terminated STO by pulsed laser deposition (PLD), a metallic interface can emerge[21]. As shown in Figure 3(b), there is a critical LAO thickness of about four unit cells, above which the interface becomes conducting. It is noteworthy that both strain and surface chemistry changes can shift the critical thickness.

(111) or (110) orientated LAO/STO can also exhibit a conducting interface, but with a different critical thickness of nine or seven unit cells, respectively[1].

Ohtomo and Hwang reported a high-mobility electron gas at the interface between $SrTiO_3$ and $LaAlO_3$[21] in 2004. This conducting region extends into the STO layer and has been experimentally shown to be confined within around 10 nm. Typical carrier densities reported in this system are around 5×10^{13} cm^{-2}, and the carrier mobility is on the order of 10 $cm^2/V \cdot s$ at room temperature. High mobilities exceeding 10^4 $cm^2/V \cdot s$ have been reported at low temperatures for systems with reduced dimensionality[22-24].

When the LAO layer is slightly below the critical thickness, the interface is insulating but highly tunable. The interface can undergo a metal-insulator phase transition at room temperature, as shown in Figure 3(c), by applying ±100 V to the back of the STO substrate. The conducting or insulating behavior persists even after the back gate voltage is removed[25]. Conductive atomic force microscope (c-AFM) lithography can locally control the metal-insulator transition with nanometer-scale precision[26], and will be discussed in Section 2.1.4.

2.0 Experimental Methods

2.1 $LaAlO_3/SrTiO_3$ Sample Growth and Patterning

2.1.1 Sample Growth

LAO/STO samples are grown via pulsed laser deposition (PLD) by our collaborators, Sangwoo Ryu, Hyungwoo Lee, Jung-Woo Lee, Ki-Tae Eom, and Chang-Beom Eom at the University of Wisconsin-Madison.

2.1.1.1 STO Pre-growth treatment

STO (001) substrates are purchased from a commercial crystal supplier. Before deposition, low miscut (<0.10°) $SrTiO_3$ substrates are etched using buffered HF acid for 60 seconds to remove SrO and maintain Ti termination, and the substrates are annealed in oxygen at 1000°C for six hours to create atomically smooth surfaces with single unit cell height steps. The mis-cut angle is carefully controlled, so that the width atomic terraces on STO surface is about 500 nm.

2.1.1.2 LAO Deposition

In pulsed laser deposition (PLD), pulses from a KrF excimer laser ($\lambda = 248$ nm) are focused on a LAO target, and plumes of target material are deposited on pre-heated STO substrates. Specific temperature and pressure conditions must be met for proper LAO/STO sample growth. A thin film (3.4 or 8 unit cells) of LAO is deposited epitaxially on a (001) TiO_2-terminated STO substrate at 550 °C and an oxygen pressure of 10^{-3} mbar, with its thickness monitored in situ via

high-pressure reflection high-energy electron diffraction (RHEED). The substrate is then cooled to room temperature in 1 atm (10^3 mbar) oxygen. The sample temperature is monitored by a K-type thermocouple, which is located inside of a heater attached the sample with silver paste. Representative RHEED patterns, in-situ RHEED oscillations and X-ray diffraction patterns for the samples are included in Figure 4.

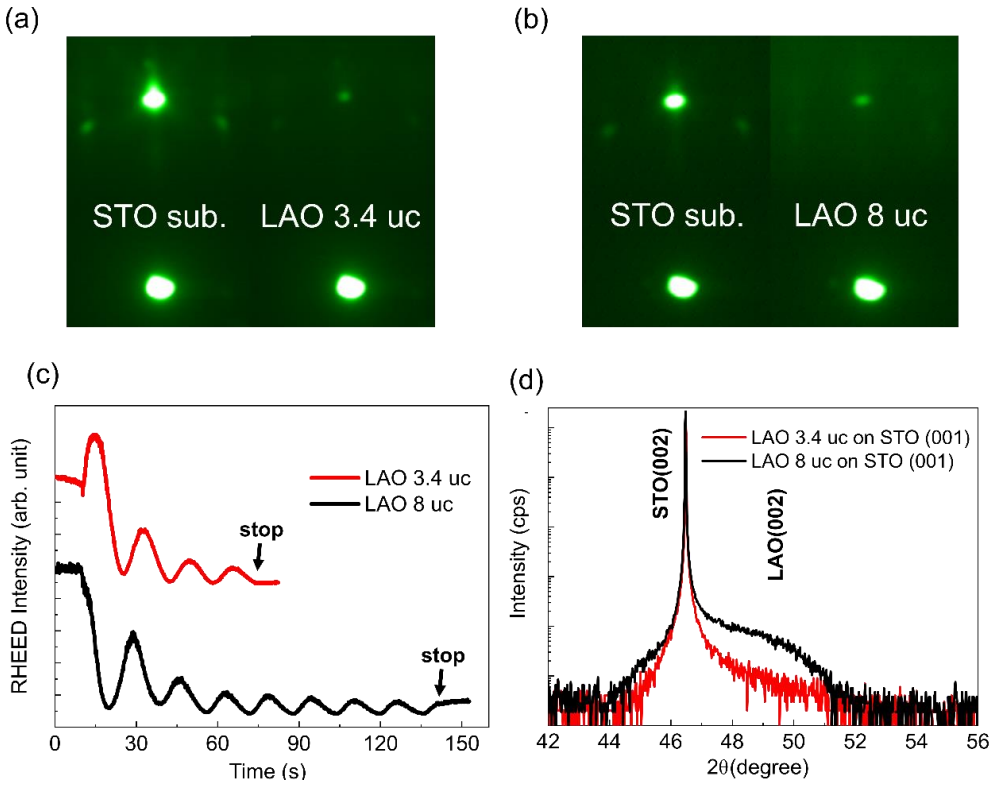

Figure 4: LAO/STO Sample Growth. (a) (b) RHEED patterns obtained before and after LAO growth at thicknesses of (a) 3.4 unit cells and (b) 8 unit cells. (c) In-situ RHEED oscillation obtained during the growth of LAO film on STO substrate. (d) $\theta - 2\theta$ Out-of-plane X-ray diffraction patterns around the STO (002) peak for both 3.4 and 8 unit cell LAO. Measurements obtained by our collaborator Ki-Tae Eom.

After the graphene integration process (described in the next section) the LAO/STO samples can become highly insulating, which makes it difficult to perform c-AFM lithography. To

address this issue, we have performed experiments on samples with a thicker LAO layer. 8 unit cell graphene/LAO/STO samples allow for effective c-AFM lithography through the graphene while maintaining an insulating LAO/STO interface. The phenomena observed in Chapter 4.0 have been observed in multiple samples with different LAO thicknesses, and show no dependence on this parameter.

2.1.2 Sample Patterning

When working with the LAO/STO interface, one of the challenges that arises is creating good electrical contact between the interface and bonding pads located at the LAO surface. Sample processing methods have to be carefully chosen so that the interfacial properties, in particular its insulating-to-conducting transition, will not be affected. Sample cleanness is another concern, as nano-particles introduced during processing might affect the quality of nanoscale devices created in the sample. To that end, our group's custom sample patterning process has been developed. In summary, electrical contacts to the LAO/STO interface are fabricated via conventional photolithography, where lithographically predefined regions are etched via Ar+ ion milling to a depth of 30 nm. Etched regions are filled with a 4 nm-thick Ti layer, then a 25 nm-thick Au layer, to create electrical contacts to the interface. A second layer of Ti/Au is added on top of the LAO surface to allow for wire-bonding. *See Jianan Li's doctoral dissertation[27] for complete details.*

2.1.3 Graphene Growth and Patterning

The graphene used in this work is grown via chemical vapor deposition (CVD) on copper substrates. CVD is a dynamic process of etching and growth, in which a substrate placed in a vacuum chamber is exposed to one or more volatile precursors, which react with the substrate surface to produce the desired material, such as graphene.

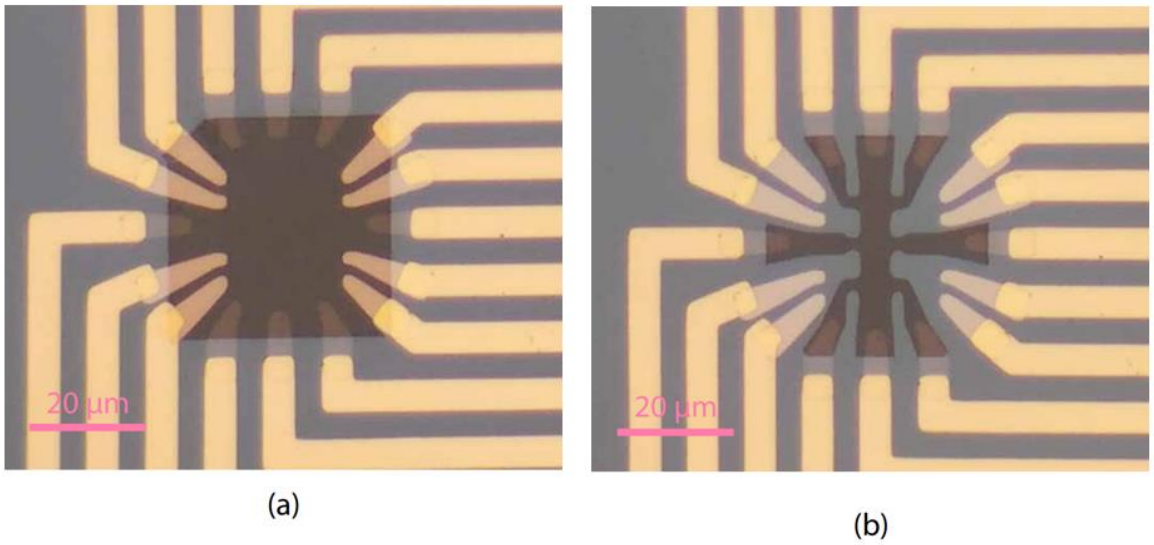

Figure 5: Optical Microscope Image of Graphene/LAO/STO canvas. (a) After graphene transfer and (b) after photolithography patterning.

Wafer-scale graphene sheets can be grown on Cu, then easily transferred to other substrates. The transfer method used to create graphene/LAO/STO heterostructures is referred to as wet transfer. In this process, a spin-coated polymer layer is deposited to protect the graphene, while the metallic growth substrate is etched away. Polymethyl methacrylate (PMMA) is typically used as the graphene protection polymer. However, residue formed by PMMA during graphene transfer has limited graphene device performance. We replace PMMA with Hyflon to reduce the

presence of harmful residues. Hyflon is a perfluorinated polymer that is both highly hydrophobic and chemically inert.

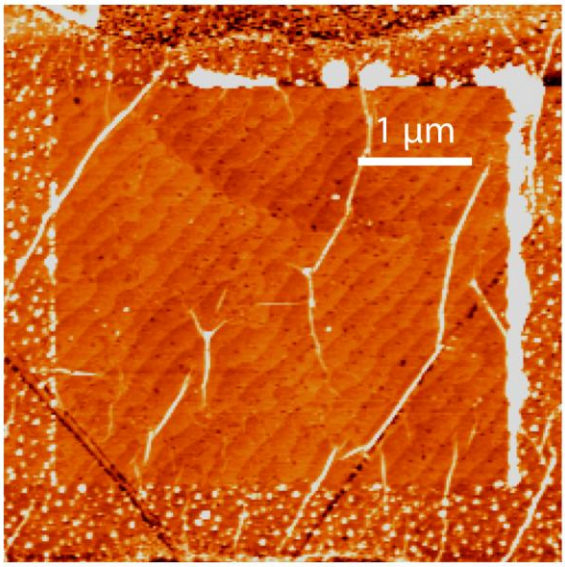

Figure 6: Cleaning graphene with AFM tip. The center, cleaned region shows graphene (with some wrinkles) directly on top of the LAO surface. The region between the LAO and graphene is extremely clean, as evidenced by the visibility of clean terraces on the LAO surface.

After etching, the graphene is rinsed and transferred onto a pre-patterned LAO/STO substrate, and soft-baked to remove any water stuck between graphene and LAO. The transferred graphene is patterned into Hall bars via photolithography. The patterned graphene/LAO/STO sample is rinsed with acetone to remove the photoresist, and then Hyflon is removed. Finally, residue particles left on the patterned graphene/LAO surface are cleaned away by an AFM tip in contact mode. Each graphene/LAO/STO canvas consists of a graphene Hall bar with eight connections, and eight connections to the LAO/STO interface, as shown in Figure 5. Atomic force microscope images of graphene patterned onto LAO in this manner reveal a clean interface

between the two materials, as shown in Figure 6. *Full details can be found in Jianan Li's dissertation*[27].

2.1.4 Conductive AFM lithography

2.1.4.1 **Lithography Process**

In 2008, Cen *et al.* reported the ability to create and erase nanoscale conducting regions at the interface of LAO/STO using the c-AFM lithography technique[26].

The device fabrication process typically begins with a heterostructure of 3.4 unit cells of LAO on STO, which is just below the critical thickness discussed in Section 1.1.4. The LAO/STO interface is therefore insulating, yet its conductivity is highly tunable via an applied electric field. The conductance between two interface electrodes is measured *in situ* during the writing process. As shown in Figure 7, when a positively biased AFM tip (made of doped silicon) is scanned in contact mode across the LAO surface, with a typical writing speed of $0.5 - 1\ \mu m/s$, it connects one interface electrode to another and creates a conducting nanowire at the LAO/STO interface.

An alternating current (AC) voltage of ±100 mV is applied to the source electrode, while the drain electrode is connected to an ammeter to measure conductance. The associated change in conductivity is confirmed by a significant jump in the two-terminal conductance once the tip reaches the second electrode and completes the circuit. It is important to note that during writing, a protective resistor is connected in series between the tip and voltage source, to protect the sample from damage. The resistor value can be controllably switched to values ranging from $100\ k\Omega$ to $1\ G\Omega$. The resistance of a conducting nanowire is typically about $200\ k\Omega/\mu m$.

The lithography process is reversible; when a negatively biased AFM tip scanned across an existing conducting nanowire, it restores the interface back to an insulating state. A corresponding conductance drop is observed as the tip erases the nanowire. The width of the nanowire can be estimated by cutting a nanowire with a negative voltage and fitting the measured drop in conductance. It has been shown that the nanowire width at the LAO/STO interface depends sensitively on the writing voltage [28]. At +3 V, a wire width of 2~3 nm can be reached; as the writing voltage increases, the nanowire width increases monotonically. With the most commonly used writing voltages (+10~15 V), the wire width is typically around 10 nm. Once a nanostructure is fabricated, it can persist indefinitely in vacuum. In ambient conditions, however, the structures decay on the order of hours. The decay process can be understood by considering the physical mechanism which enables c-AFM lithography, described next. Research is currently underway with the goal of extending the structures' lifetimes in the ambient environment.

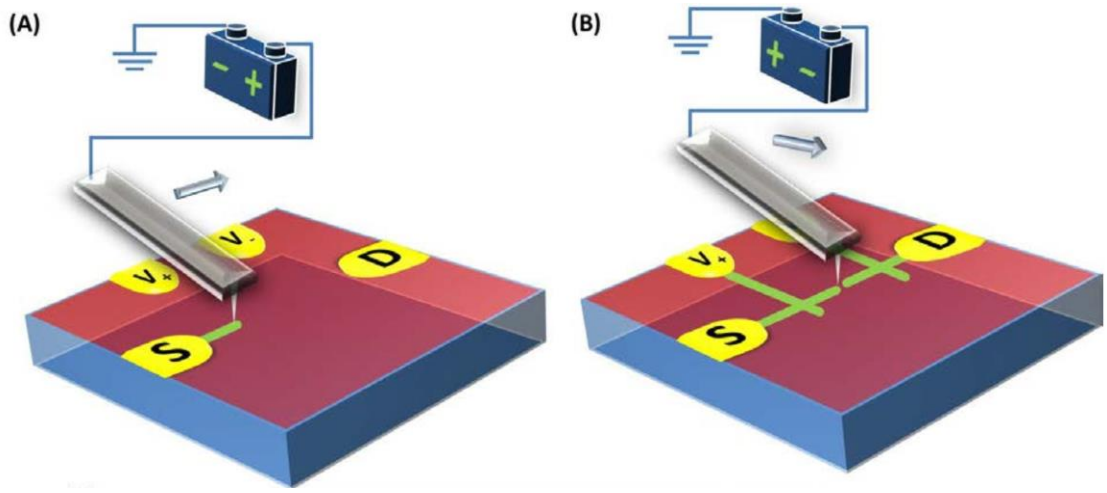

Figure 7: C-AFM Lithography Process. (a) Creating conducting nanostructures with a positively biased tip and (b) erasing them with a negatively biased tip. Adapted from Cen *et al.*[28].

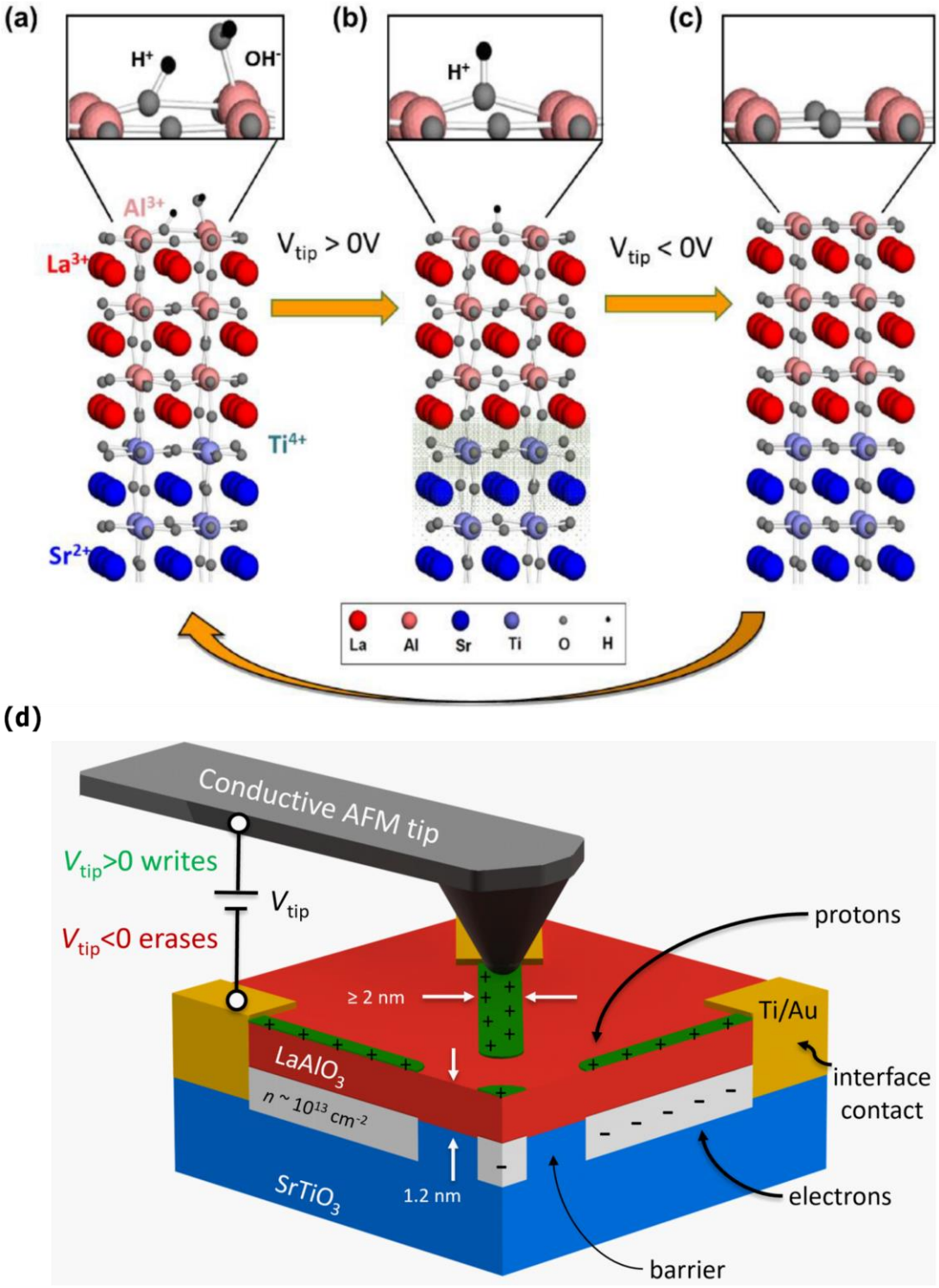

Figure 8: Water cycle mechanism for c-AM lithography. (a-c) Diagram of "water cycle" adapted from Bi *et al*[29]. (d) Diagram of surface protonation during c-AFM lithography.

2.1.5 Creating LAO/STO Nanojunctions

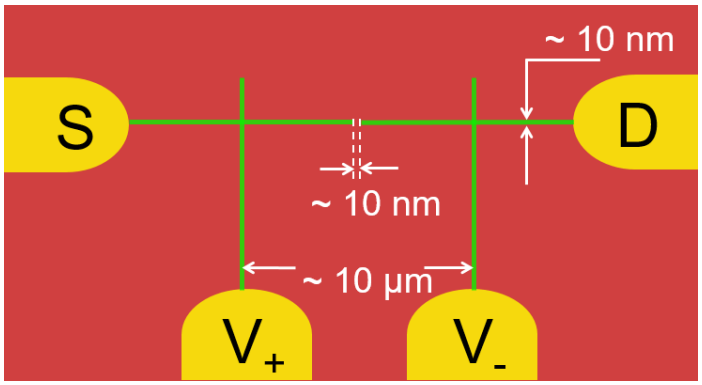

Figure 9: Top-Down view of a four-terminal nanojunction.

A nanojunction device is defined as a conducting wire with a nanoscale ($\sim$10 nm) gap. These devices are typically designed in a four-terminal geometry, where the nanowire is connected to source and drain electrodes, in addition to two voltage sensing leads. To create an LAO/STO nanojunction, a nanowire is defined by scanning the c-AFM tip on the LAO surface with a positive voltage ($10 - 20$ V). The nanoscale insulating gap, or junction, is defined by applying a negative voltage (-10 V) to the AFM tip and drawing a "cut" wire across the conducting wire.

As compared to c-AFM defined LAO/STO quantum dots and barriers, nanojunction gaps are larger, in the sense that the barrier to current flow is larger. Current-voltage (I-V) curves determine a threshold voltage on the order of $0.1 - 1$ V before significant current flows through the nanowire. These larger gaps allow for faithful operation under illumination; this is important because nanojunctions' primary use is time-domain photovoltage spectroscopy. See example I-V curves for nanojunction devices both in the dark and illuminated in Figure 10. A DC bias voltage V_{SD} is applied to the LAO/STO nanojunction through the source electrode S via a 50-Ω-impedance analog output port, while the drain electrode D is grounded. The four-terminal voltage is defined

as the voltage difference $\Delta V = V_+ - V_-$ between the two voltage sensing electrodes, and is measured by a differential voltage amplifier (DVA) with 0.1 MΩ input impedance. Two-terminal current is measured between the source and drain electrodes versus source voltage in Figure 10 (a), whereas the current is measured between the source and drain electrodes versus the differential voltage between the V+ and V- electrodes is measured in Figure 10 (b,c).

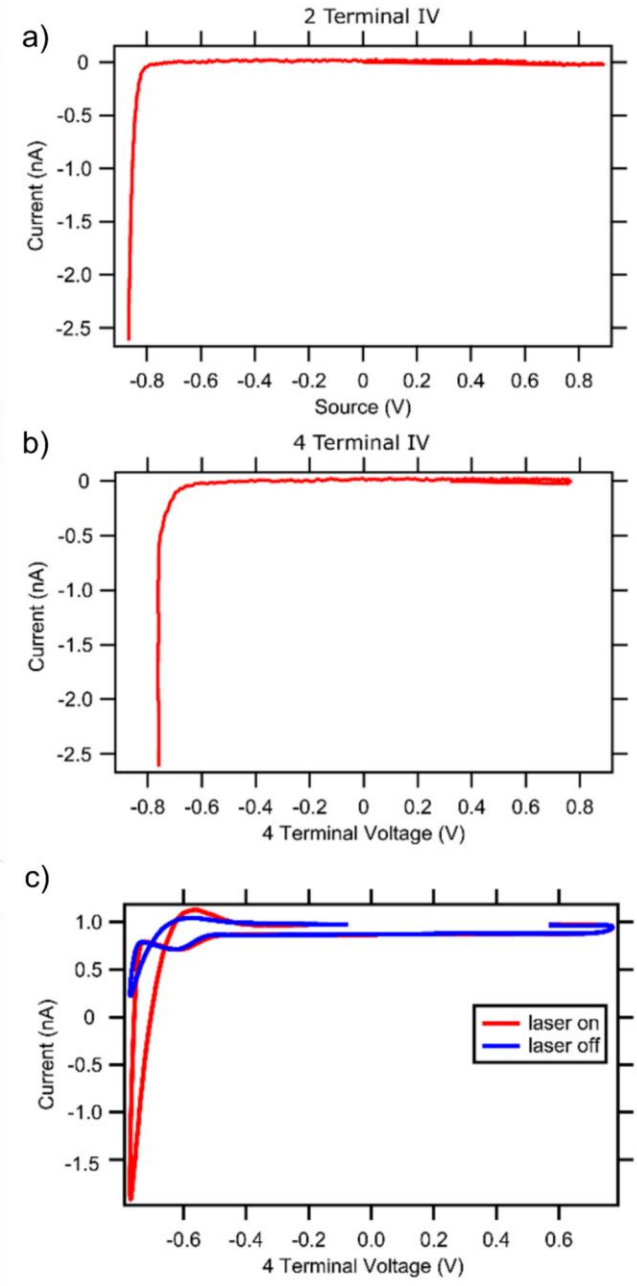

Figure 10: Nanojunction IV curves. (a) Two-terminal IV curves measured between source and drain connections and (b) four-terminal IV curves with the four-terminal voltage measured between V+ and V- connections across a graphene/LAO/STO nanojunction at $T = 80$ K and 12 μW input power from broadband VIS-NIR pulses. (c) Four-terminal I-V curves for a separate device, both with and without laser illumination, at $T = 5$ K, 11.88 μW input power.

2.1.5.1 **Phenomena observed in LAO/STO nanostructures**

The reconfigurable and versatile c-AFM technique has made LAO/STO a fruitful platform for studying correlated electron interactions, as well has realizing nanoscale electronic and photonic devices with various functionalities. A large number of nanostructures, such as field-effect transistors, electric rectifiers[30], quantum dots, single-electron transistors[31], ballistic electron waveguides, Hall crosses, photodetectors[32], broadband THz sources and detectors[33], etc. have been created and studied. In addition to observations of frictional drag[34], quantum oscillations[35], superconductivity[36,37] and electron pairing without superconductivity[38] in LAO/STO nanostructures, this system has been shown to host a new, exotic phase of fermionic matter. Quantized conductance steps were observed in electron waveguides, where the conductance follows a characteristic sequence within Pascal's triangle: $(1,3,6,10,15\ldots)\cdot e^2/h$ (where e is the electron charge and h is the Planck constant.) This behavior is consistent with the existence of a family of degenerate quantum liquids formed from bound states of , $n = 2,3,4$ ... electrons[39].

Finally, LAO/STO nanostructures constitute a potential platform for quantum simulation. Artificial superlattice potentials can be imposed on waveguide devices, with a superlattice spacing that can be made comparable to the mean separation between electrons[40]. The imposed superlattice potential modifies the electronic band structure of the device, and the engineered spin–orbit interaction in the superlattice contributes to the enhanced electron pairing. These findings demonstrate the ability to design new families of quantum materials with emergent properties and solid-state one-dimensional quantum simulation platforms.

2.2 Creation of Graphene/LAO/STO Nanostructures

2.2.1 C-AFM Lithography with Graphene

Graphene/LAO/STO heterostructures are created and patterned as detailed in Section 2.1.3. Because single layer graphene is less than one nanometer thick, c-AFM lithography can be performed through the layer, as shown in Figure 11, without making many significant changes to the process.

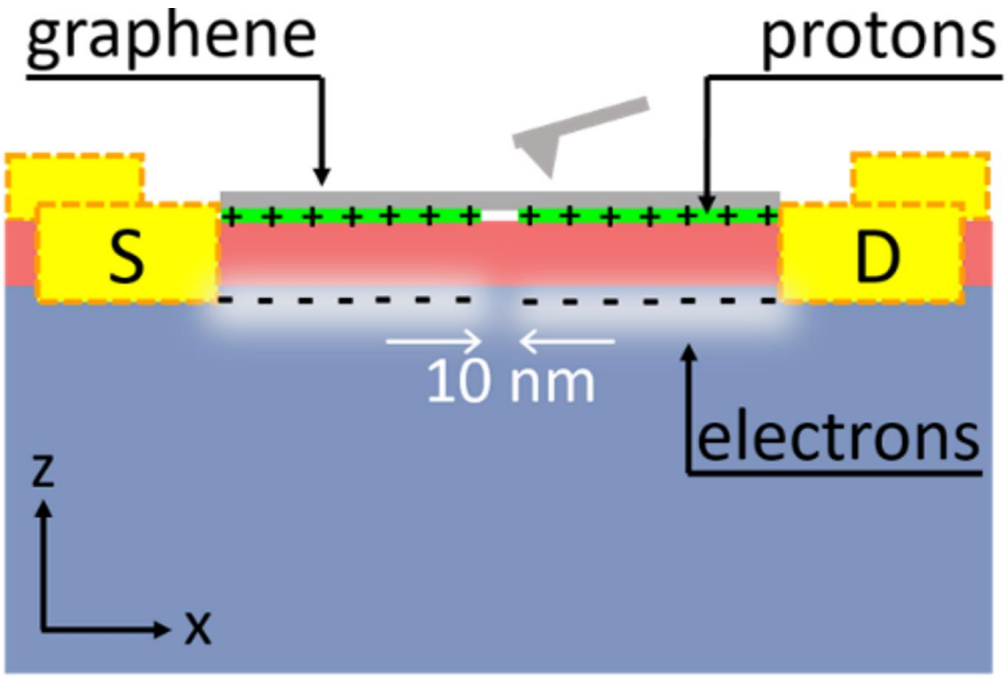

Figure 11: LAO/STO nanojunction defined underneath single layer graphene.

When a conducting nanowire is defined as above, except through a graphene layer, piezo-force microscopy (PFM) imaging reveals a distinct nanowire feature (see Figure 12.) A corresponding conductance jump is observed between the interface electrodes, confirming the presence of a

nanostructure directly beneath the graphene. See Huang *et al*.[41] for more details on PFM imaging of LAO/STO nanostructures.

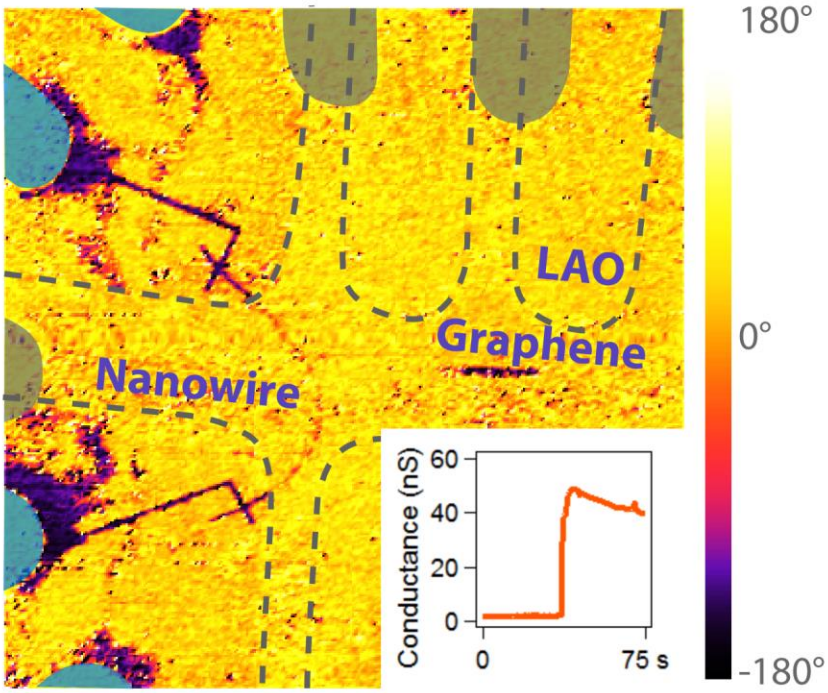

Figure 12: PFM image of graphene/LAO/STO nanowire. Inset: measured conductance jump between LAO/STO interface leads through the nanowire.

2.2.2 Graphene/LAO/STO Nanojunctions

To create a graphene/LAO/STO nanojunction, a nanowire is defined by scanning the c-AFM tip in a region where the graphene covers the LAO surface with a positive voltage, and the nanoscale insulating gap, or junction, is defined by applying a negative voltage (-8 V) to the AFM tip and pressing down for three seconds at a point along the nanowire. This method, as opposed to sketching a negative "cut" nanowire, is more gentle, in order to avoid damaging the graphene with the AFM tip.

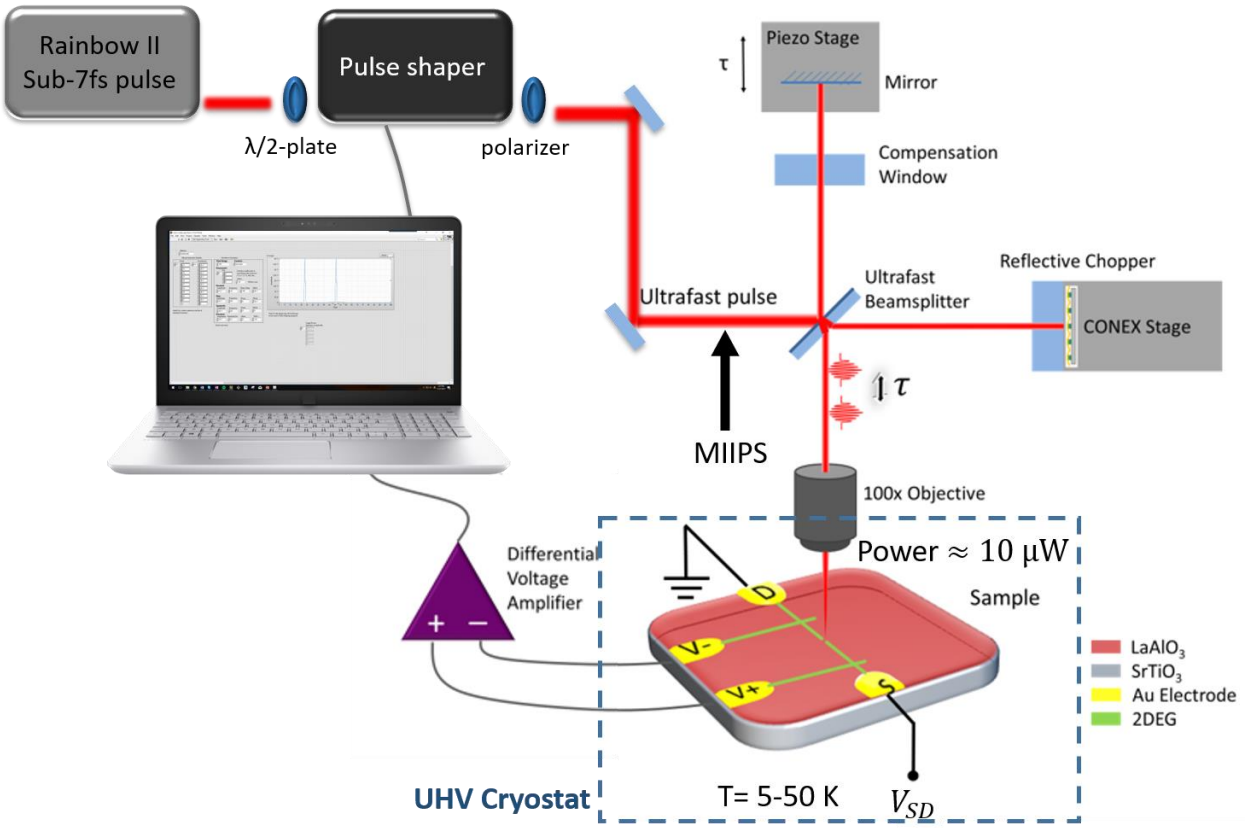

Figure 13: Overall Experimental setup. Main components include a femtosecond Ti:Sapphire laser, a Fourier pulse shaper, a Michelson interferometer and an optical cryostation at ultra-high vacuum (UHV). Multiphoton intrapulse interference phase scan (MIIPS) compensation is obtained with nonlinear crystal and spectrometer placed where MIIPS is labeled.

2.3 Optical experimental setup

The main components of the experimental setup used in this work are a femtosecond Ti:Sapphire laser, a Fourier pulse shaper, a Michelson interferometer and an optical cryostation. A diagram of the overall setup is shown in Figure 13. Individual components are discussed in detail in the following sections.

2.3.1 Ultrafast laser

The ultrafast laser used in this work is a Spectra Physics Rainbow 2 Ti:Sapphire laser. It is an ultra-broadband few-cycle pulse oscillator system, which uses dispersive mirrors for intracavity GVD dispersion. An additional cavity dispersion control unit provides precise dispersion control, so that the system can output nearly bandwidth-limited sub 7-fs pulses with a spectral bandwidth of over 300 nm and a 75 MHz repetition rate. The system also has low noise and can maintain mode-lock for days at a time, and can achieve maximum mode-locked power between 550-600 mW. The output field is p-polarized (or horizontal).

2.3.2 Compact Michelson Interferometer

The primary component of our optical setup is a home-built compact Michelson interferometer, which allows us to measure the ultra-fast time-domain response of LAO/STO nanojunction devices. A three-dimensional CAD diagram of the interferometer design is shown in Figure 14. A plane mirror directs input laser pulses to a 50/50 ultrafast beam splitter. The transmitted beam is sent to the back arm, while the reflected beam is sent to the upper arm. The upper arm contains an optical delay line, which consists of a reflective chopper mounted to a piezo nano-positioning stage. The time delay zero location is calibrated by measuring the autocorrelation signal of an LAO/STO nanojunction while the mechanical stage is translated. The constituent components of the interferometer are discussed in detail below.

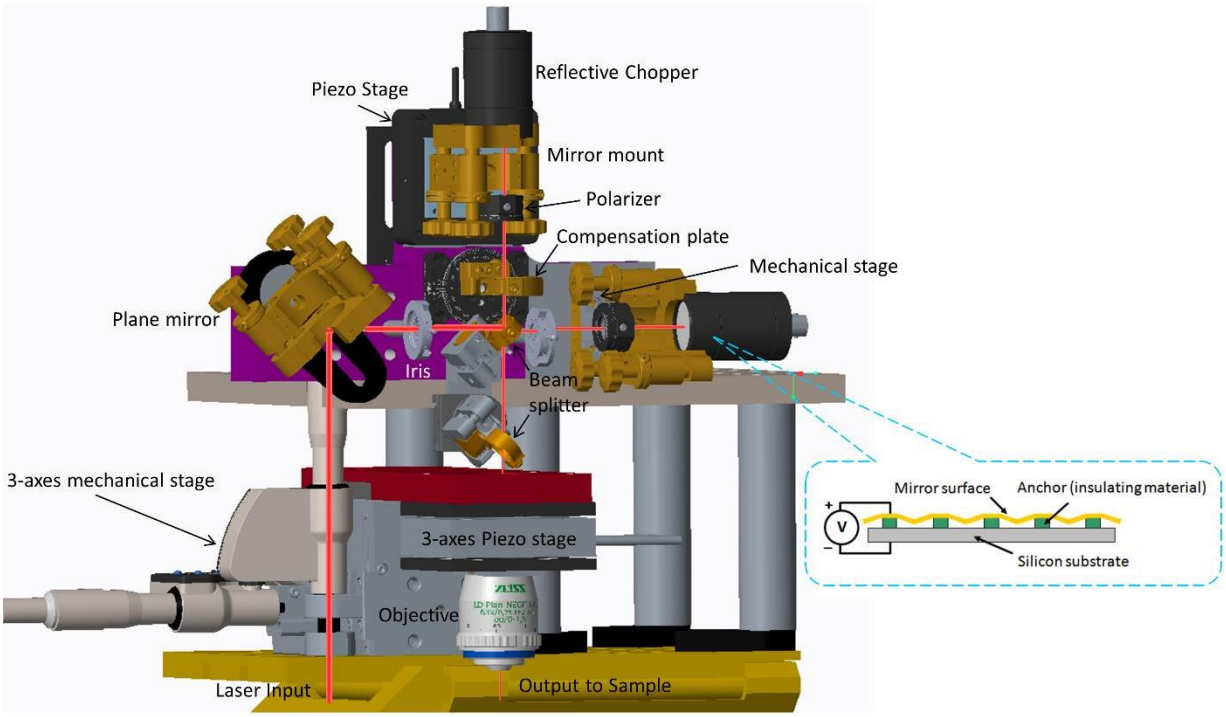

Figure 14: CAD Image of Michelson Interferometer.

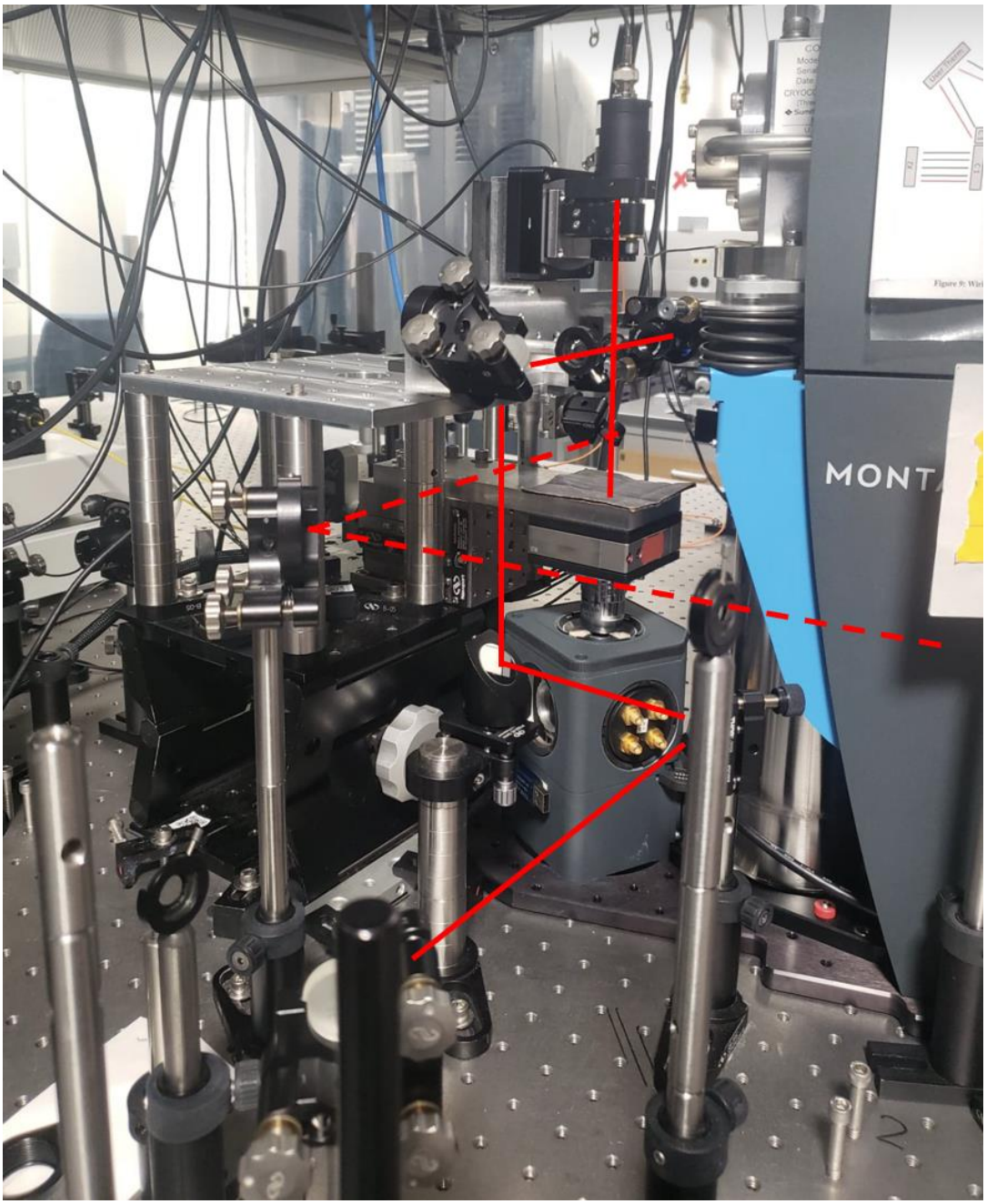

Figure 15: Photo of Michelson interferometer. The input beam path to the sample is shown in solid red, whereas the output reflection beam path is shown in dashed red.

2.3.2.1 **Optical Delay Line**

Piezoelectricity is an electrical charge that is produced in certain materials when the material is subjected to an applied mechanical stress or pressure. This is known as the direct piezoelectric effect. The converse or inverse piezoelectric effect, or the application of an electric field to induce strain, enables piezoelectric materials to be used in positioning applications. Piezo actuators exhibit hysteresis and non-linearity when operated in open-loop mode. When operating our Aerotech piezo actuator in closed-loop mode, the non-repeatabilities due to hysteresis are eliminated.

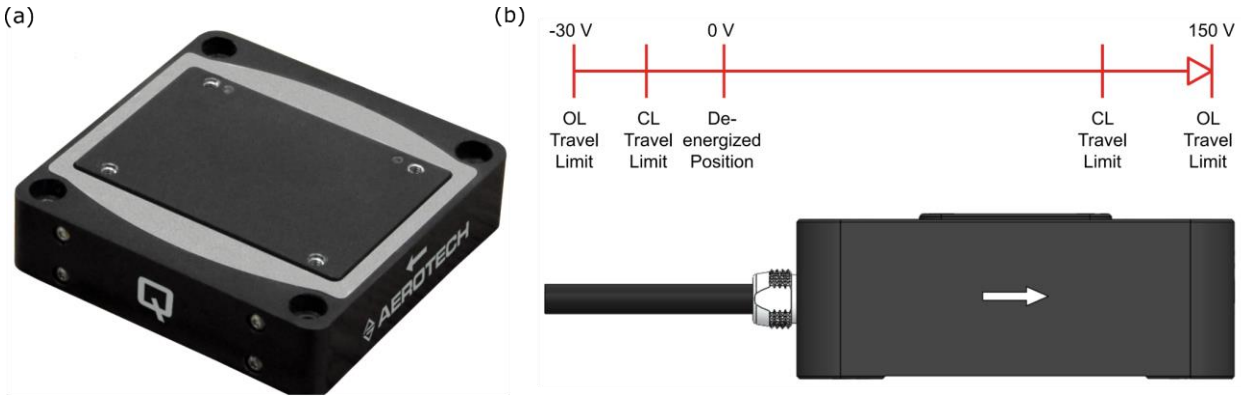

Figure 16: Aerotech piezo stage. (a) Aerotech Q-series nanopositioning piezo stage. (b) Diagram showing voltage-posiiton realtionship for the stage in both open and closed-loop modes.

2.3.2.2 **Reflective Chopper**

Boston Micromachines Corporation MEMS grating modulators are mounted at the end of each arm of the Michelson interferometer. These “reflective optical choppers” are used, both as mirrors and as choppers to modulate the optical signal at a specified frequency. The MEMS Grating Modulator is a reflective diffraction grating with controllable groove depth. It modulates intensity by switching between an unpowered flat mirror state and a powered diffractive state. By

simply adjust the maximum depth of deflection, one can modulate the central intensity of an input beam with high levels of extinction, achieving broadband intensity modulation.

The device consists of a gold-coated membrane which enables wavelength modulation from the visible to the far infrared (FIR), with peak extinction in the visible and near infrared (NIR) and lower extinction in the FIR. To attain peak modulation of an incident beam up to 6mm in diameter, one can simply tune the deflection at a given wavelength by using a high voltage source. The MEMS grating modulator has a response time as small as 2.5 μs. It has a full-modulation a frequency range from DC to 200kHz, and can operate at even higher speeds when used for partial modulation. Compared to alternative acousto-optical modulators, it has the advantage of being dispersionless, in addition to delivering high spatial resolution.

2.3.3 Scanning Reflection and Photovoltage Measurement

The interferometer's focusing microscope objective (100X, NA = 0.73) is fixed on a closed-loop 3-axis piezo stage (Piezosystem Jena Tritor T-401-1), which is digitally controlled to move the objective and focus the light onto each spot along the sample surface. At each point, the sample reflection and the photovoltage signal from a biased LAO/STO nanojunction are measured simultaneously. Overlaying these images allows a precise measurement of the location of a nanojunction device, so that the focused laser spot can be positioned directly over it. An example measurement on a graphene/LAO/STO nanojunction device is summarized in Figure 17.

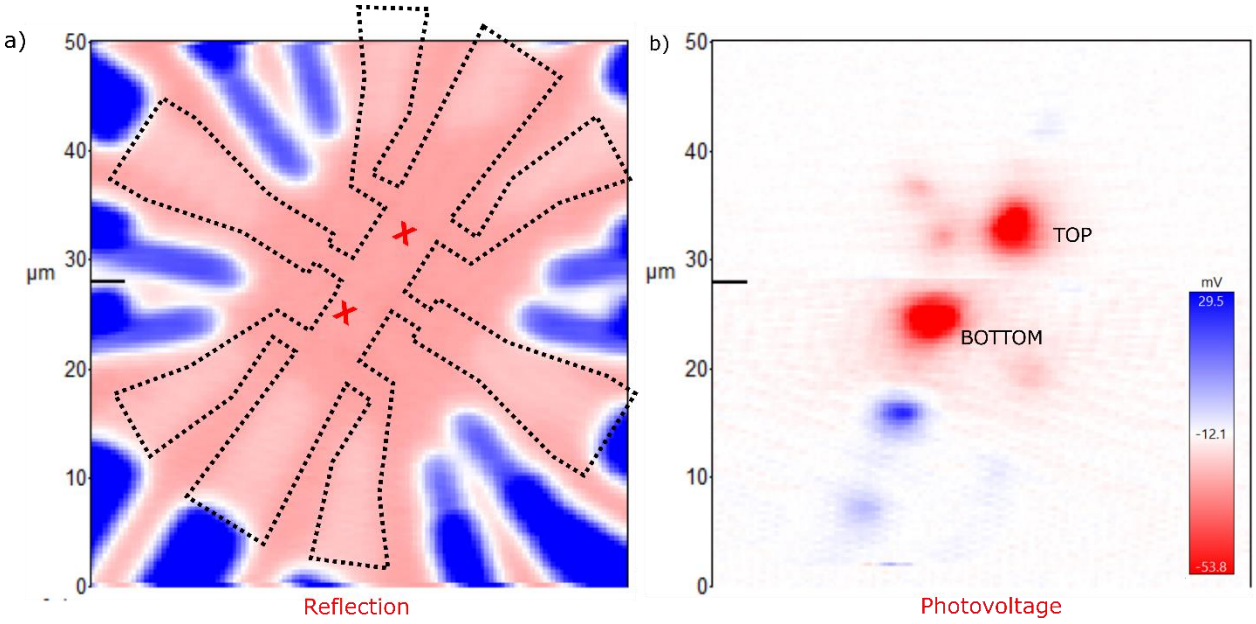

Figure 17: Scanning reflection and photvoltage signals. Superimposed (a) reflection and (b) photovoltage images for each of the two graphene/LAO/STO nanojunctions. A black outline marks the approximate location of the graphene Hall bar. The superposition of the two images leads to a slight x-offset between them here. Data taken at $T = 20$ K, graphene global gate $V_G = 0\ V, V_{SD}^{top} = V_{SD}^{bottom} = -1\ V$ and input power 10 μW.

2.3.4 Time-Domain Photovoltage Measurement

During a time-domain photovoltage measurement, the optical delay line is scanned continuously from negative to positive time delay values. A DC bias voltage V_{SD} is applied to an LAO/STO nanojunction device through the source electrode S via a 50-Ω-impedance analog output port, while the drain electrode D is grounded. The photovoltage signal is defined as the voltage difference $\Delta V = V_+ - V_-$ between the two voltage sensing electrodes, and is measured by a differential voltage amplifier (DVA) with 0.1 MΩ input impedance and recorded as a function of τ.

2.4 Ultrafast Pulse Shaping

2.4.1 Pulse Shaping Overview

Femtosecond pulses consist of a large number of phase-locked frequency components. The relative phases between each of the frequency components can be altered; modulating the amplitude and phase of each different frequency component is referred to as Fourier transform pulse shaping[42]. By appropriately manipulating the spectral phase of an ultrashort excitation pulse, one can readily control ground state and excited state molecular dynamics, or cause chemically selective molecular excitation (ex. enhancing or suppressing multiphoton transitions). In particular, nonlinear optical processes, such as two photon absorption and second harmonic generation, are sensitive to the spectral phase of excitation laser pulses.

2.4.1.1 **Fourier transform pulse shaping**

A pulse shaper acts as a linear filter for pulses. In the time domain, the filter is characterized by a linear response function, where the output of the filter is the convolution of its impulse response function $h(t)$ and the input fields:

$$e_{out}(t) = e_{in}(t) * h(t) = \int dt' e_{in}(t') h(t - t'). \qquad \textbf{Equation 1}$$

For a sufficiently short input pulse, generating a specific output pulse shape is equivalent to engineering a linear filter with the desired impulse response function. In the frequency domain, the convolution becomes simple multiplication of the Fourier-transformed quantities. The output field $E_{out}(\omega)$ is now

$$E_{out}(\omega) = E_{in}(\omega)H(\omega), \qquad \textbf{Equation 2}$$

so that the desired output pulse is accomplished by implementing a filter with the required frequency response. We will be reviewing pulse shaping in this more natural frequency domain.

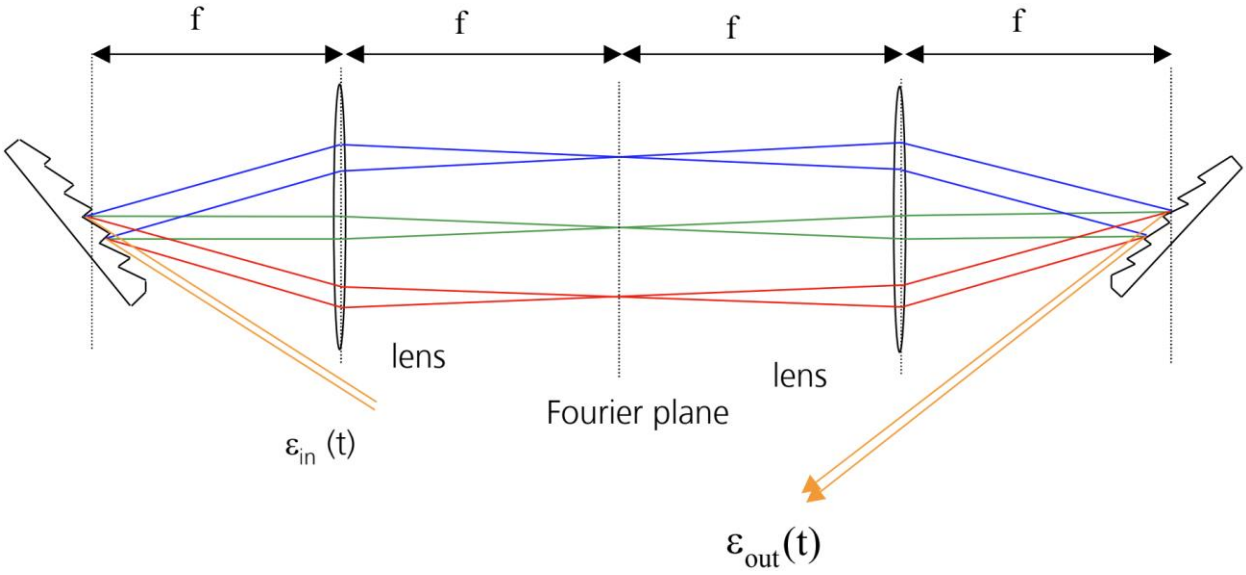

Figure 18: 4f Fourier pulse shaper in transmission mode. f represents the focal length of the lenses.

2.4.1.2 **4f Configuration**

In a 4f pulse shaper, as shown in Figure 18, an incident femtosecond pulse is first decomposed into its constituent spectral components by a spectral disperser (usually a grating) then focused using a lens or a curved mirror with a focal length f. A basic pulse shaper consists of a pair of diffraction gratings and lenses and a pulse-shaping mask. The spectral components of the input pulse are spatially spread by the first grating and focused onto the mask via a lens (or curved mirror.) The lens effectively performs a Fourier transform to convert the angular dispersion from the grating to a spatial separation at the focal plane. A spatially patterned mask then modulates the phase and amplitude, and sometimes the polarization, of the spatially dispersed spectral components. A second lens directs the wavelength components to the second grating, which

recombines them into a collimated output beam. The output pulse shape is given by the Fourier transform of the pattern transferred by the mask onto the spectrum, is collimated, and ready to use in experiments. The 4f pulse shaping arrangement is ideally free of temporal dispersion; therefore, in the absence of a pulse shaping mask, the output pulse is nearly identical to the input. This technique has been successfully applied to pulses with widths ranging from femtoseconds to nanoseconds[42].

In this configuration, if the lens-mask separation is > f, the system provides a negative phase dispersion, i.e., it acts as a pulse compressor. If the separation is < f, on the other hand, a positive dispersion is added to the input pulse, so now the system is a pulse stretcher.

2.4.2 Spatial Light Modulators

While fixed spatial masks may be inserted into the Fourier plane, programmable pulse shaping is a much more powerful method, as it allows for computer control of the pulse shaper and enables algorithmic processes. A programmable pulse shaper can be realized by inserting an active phase mask in the Fourier plane, commonly referred to as a spatial light modulator (SLM). In principle, a single-mask SLM can achieve either phase or amplitude modulation of the pulse, while a dual mask SLM has full access to both phase and amplitude degrees of freedom. Arbitrary complex waveforms thus can be generated by programming a double-layer SLM. Liquid-crystal based SLMs take advantage of optical birefringence to achieve amplitude and phase control, as discussed next.

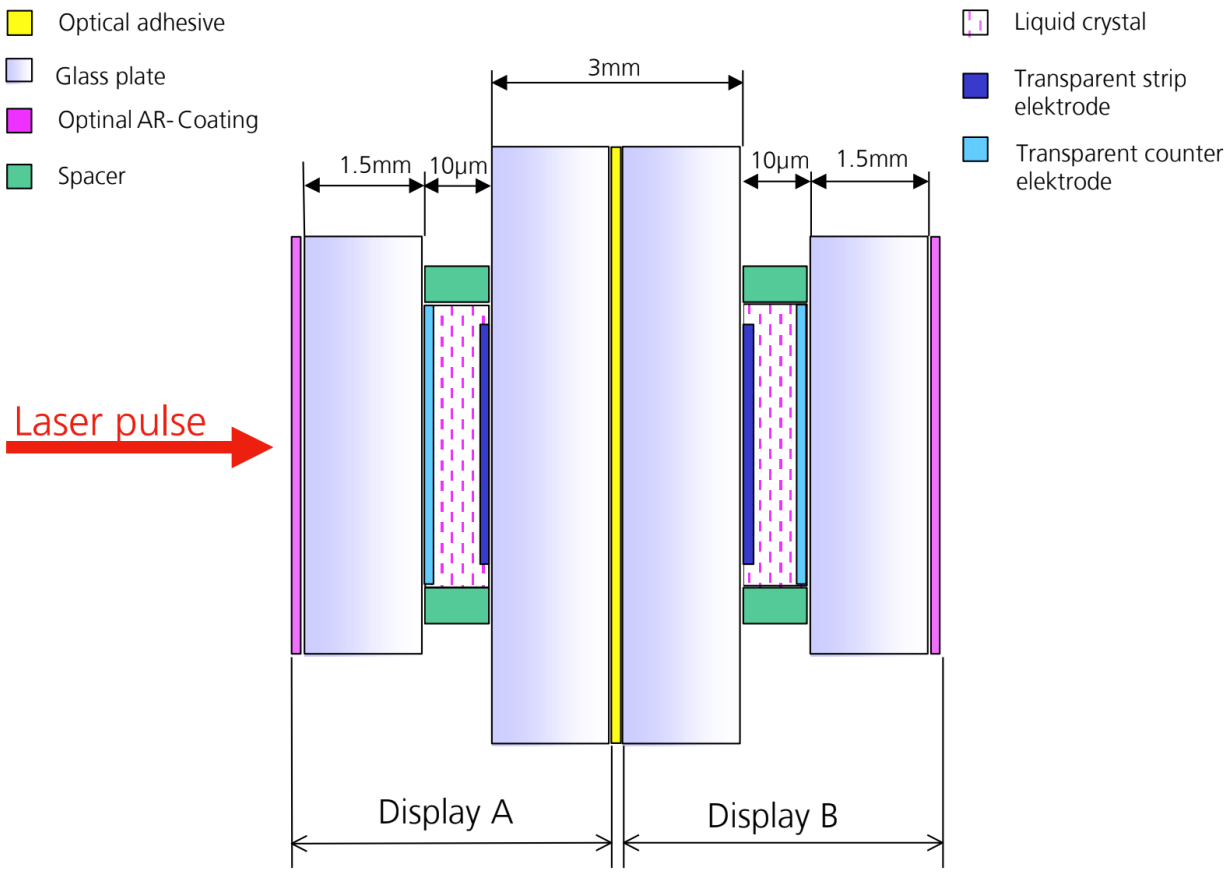

Figure 19: Dual-mask SLM liquid crystal display. Adapted from Kalkbrenner[43].

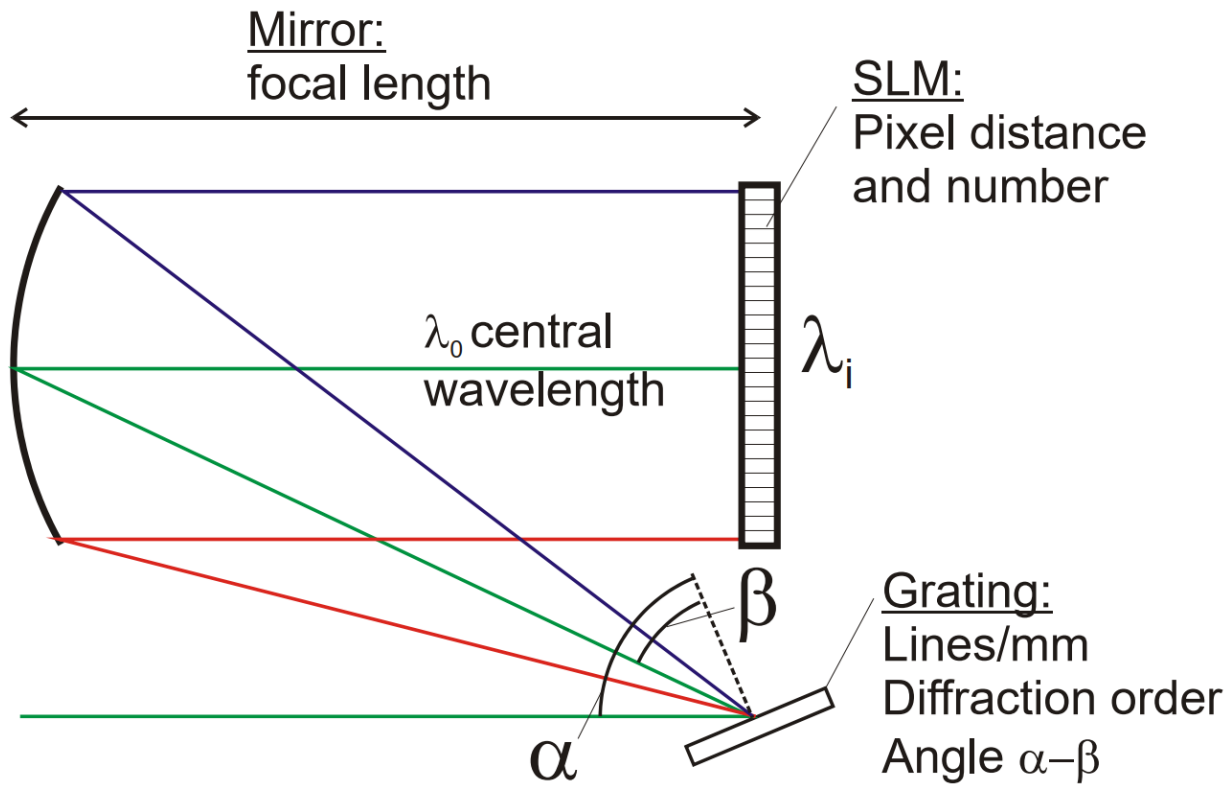

Figure 20. The role of a grating witihn a pulse shaper.Adapted from Kalkbrenner[43].Home-Built Pulse Shaper in Reflection Mode

The system used in this work, shown in Figure 22, is a 4f pulse shaper in reflection mode. A dual-mask spatial light modulator is used to control the spectral amplitude and phase across broadband ultrafast pulses. In our home-built pulse shaper setup, the optical axis of the first mask in the SLM (Display A) is at +45° from the x-axis, while the second mask (Display B) is at -45° from the x-axis. See Figure 21 for a polarization diagram.

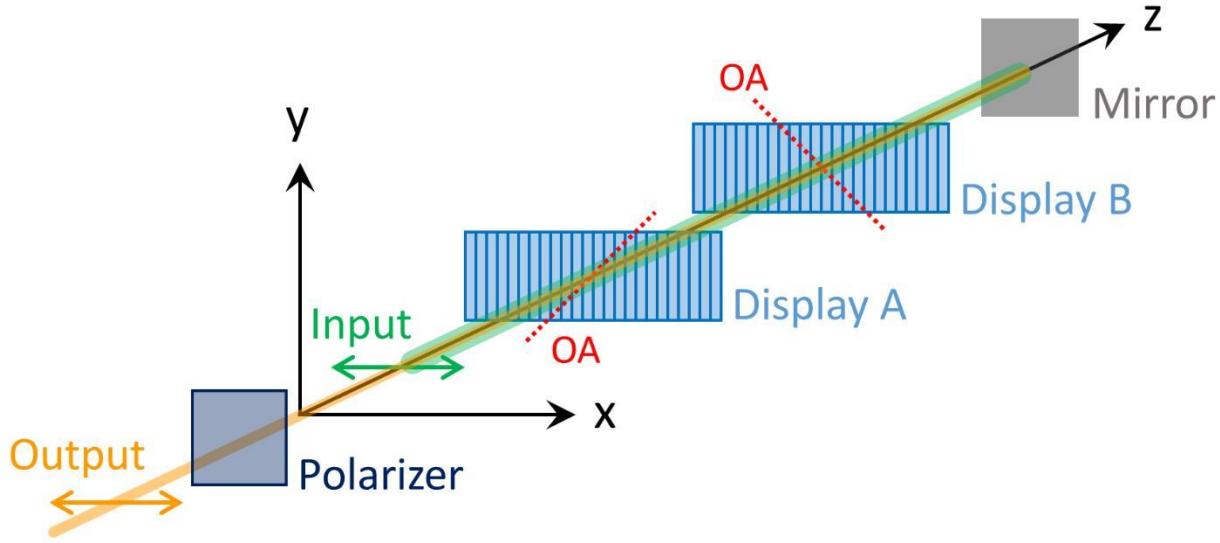

Figure 21: Dual-Mask SLM Polarization. The input beam is incident on Display A then Display B. After being reflected off of a mirror, the beam travels through Display B then Display A for a second time before being sent out of the pulse shaper.

The SLM works in a reflection mode, which means light gets reflected back after Display B and re-enters Display B and Display A consecutively. The input light has a linear polarization parallel to the x-axis and a linear polarizer that passes the horizontal polarization is placed after the pulse shaper. In this configuration, the output light can be described as follows:

$$E_{out} = \frac{1}{2} e^{i(2\Delta\phi_A + 2\Delta\phi_B)} \cdot \begin{pmatrix} 1 \\ 0 \end{pmatrix}$$

$$= \cos(\Delta\phi_A - \Delta\phi_B)\, e^{i(\Delta\phi_A + \Delta\phi_B)} \cdot \begin{pmatrix} 1 \\ 0 \end{pmatrix}$$

Equation 3

where the amplitude and phase of the output light are, respectively,

$$A = \cos(\Delta\phi_A - \Delta\phi_B)$$

$$\phi = \Delta\phi_A + \Delta\phi_B$$

Equation 4

By controlling the phase retardation in mask A and mask B via an applied voltage, both amplitude and phase of the output beam can be controlled. Note that what is actually being experimentally

measured at the output of the pulse shaper is the transmission, i.e., the intensity of the output light ($I = A^2$). Pure amplitude modulation can be achieved by changing both $\Delta\phi_A$ and $\Delta\phi_B$ in a way that $\Delta\phi_A + \Delta\phi_B = constant$, and purse phase modulation can be achieved by keeping (or $\Delta\phi_A - \Delta\phi_B = constant$). Writing out the phase retardation for each mask specifically yields

$$\phi_A = \frac{1}{2}(\phi + \arccos(A))$$

$$\phi_B = \frac{1}{2}(\phi - \arccos(A)).$$

Equation 5

For a pulse shaper in transmission mode, where the light passes through each display only once, the amplitude and phase of the output light are defined as

$$A = \cos\left(\frac{\Delta\phi_A - \Delta\phi_B}{2}\right)$$

$$\phi = \frac{\Delta\phi_A + \Delta\phi_B}{2}.$$

Equation 6

Instructions on how to calibrate the SLM are included in Appendix A.

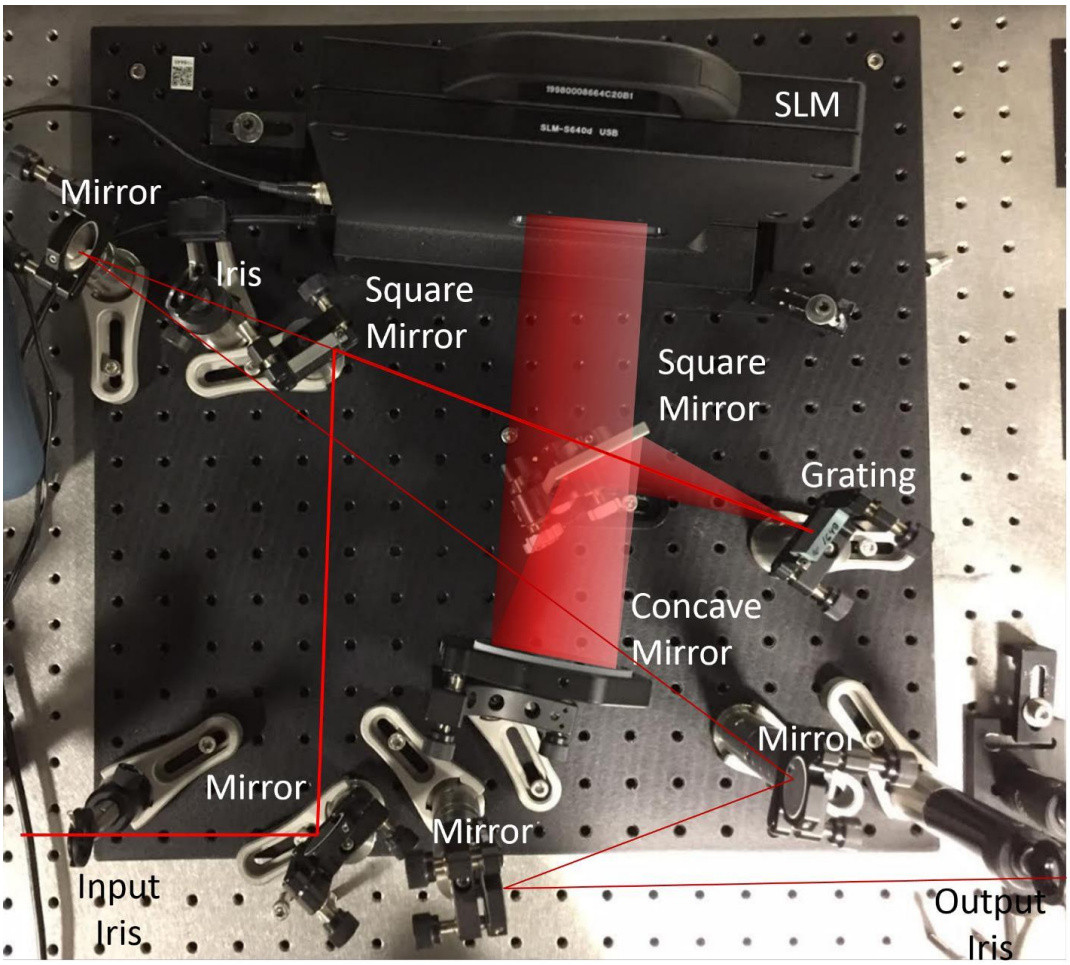

Figure 22: Home-Built Pulse Shaper in Reflection Mode.Demonstrated amplitude and phase control

Using the SLM calibration and control programs that I have built, the spectral amplitude of the ultrafast pulse can be shaped to fit an arbitrary function. A few examples of amplitude pulse shaping are shown in Figure 23, where the green line marks the input desired shape, and the blue line is the pulse amplitude measured by a spectrometer. Indeed, as discussed above, the dual-mask SLM allows for simultaneous phase and amplitude shaping. In Figure 23(d), the amplitude and phase (red curve) are set simultaneously.

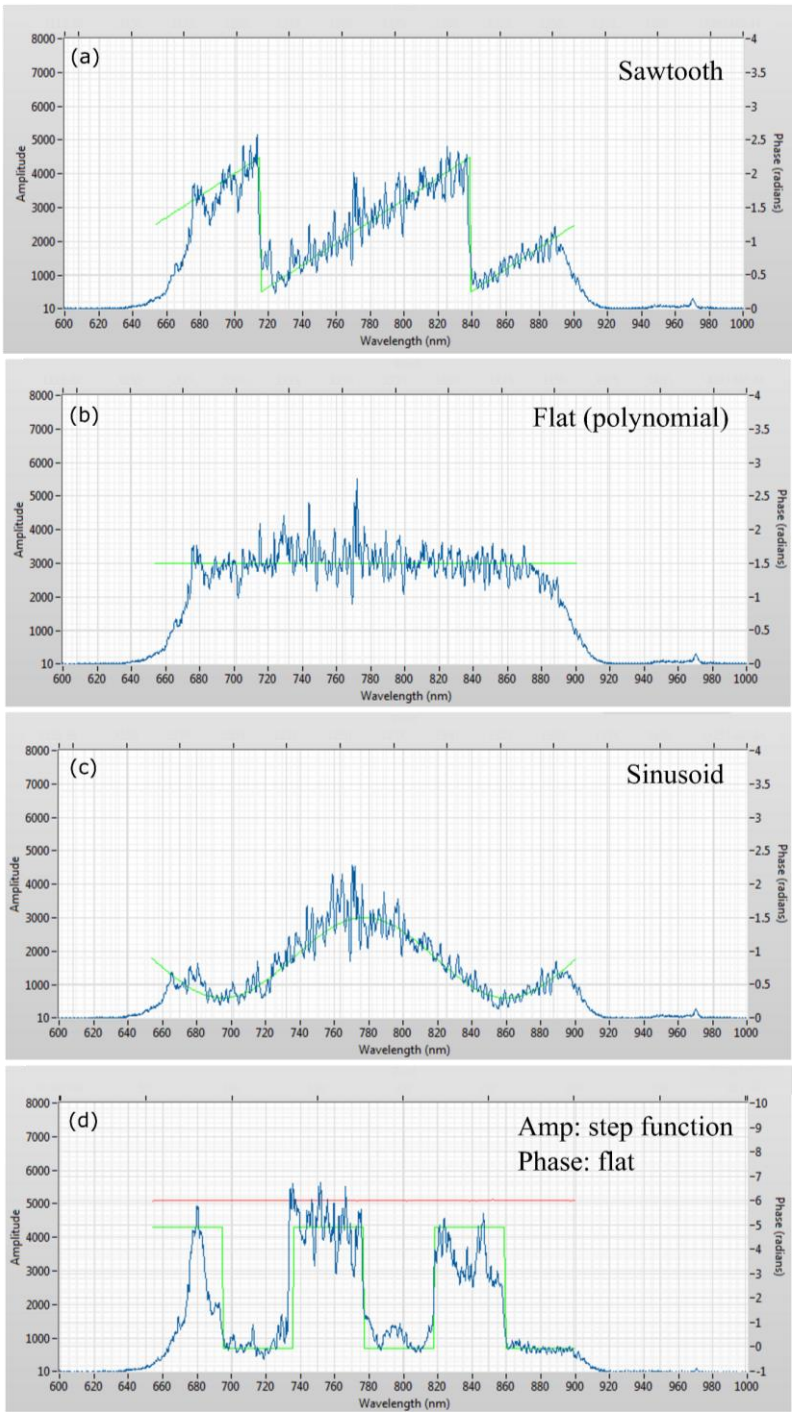

Figure 23: Amplitude and phase pulse shaping.

2.4.4 Pulse compensation

When a transform-limited ultrafast pulse leaves a laser cavity and travels through air and various optical components, such as lenses and windows, its spectral phase becomes distorted due to the frequency dependent refractive index of these media. Such distortions can have drastic effects on ultrafast pulse duration, peak intensity, and other pulse properties, which can be detrimental for many experiments or applications. To make matters worse, shorter pulses suffer more from the same amount of distortion than longer pulses, making pulse compensation absolutely essential when working with sub-10 fs pulses.

The group velocity dispersion (GVD) introduced by optical elements is usually positive for visible to near-infrared wavelengths, which means longer wavelengths arrive earlier than shorter wavelengths in an ultrafast pulse (positive chirp). To compensate for this distortion, a negative chirp needs to be introduced. The negative GVD will cause the longer wavelengths to travel along an additional optical path, so eventually, they arrive at the same time as the shorter wavelengths. In this way, negatively chirped components, such as prisms and mirrors, compensate phase dispersion. In many cases, more than one compensation scheme is adopted. For example, negatively chirped mirrors often work with a pair of thin prisms to achieve a continuous tuning of the introduced negative dispersion.

When pulse duration reduces below 30 fs, not only the second-order dispersion but also higher-order dispersion needs to be carefully compensated. More sophisticated compensation requires an accurate measure of the pulse phase using one of the aforementioned pulse characterization techniques. Then a proper compensation scheme (or a combination of schemes) can be engineered to provide the necessary negative dispersion. The multiphoton intrapulse

interference phase scan (MIIPS) system, on the other hand, has a built-in functionality to compress the pulse back to its transform-limited width while measuring the pulse characteristics, which can be convenient for experiments where consistent pulse duration is required.

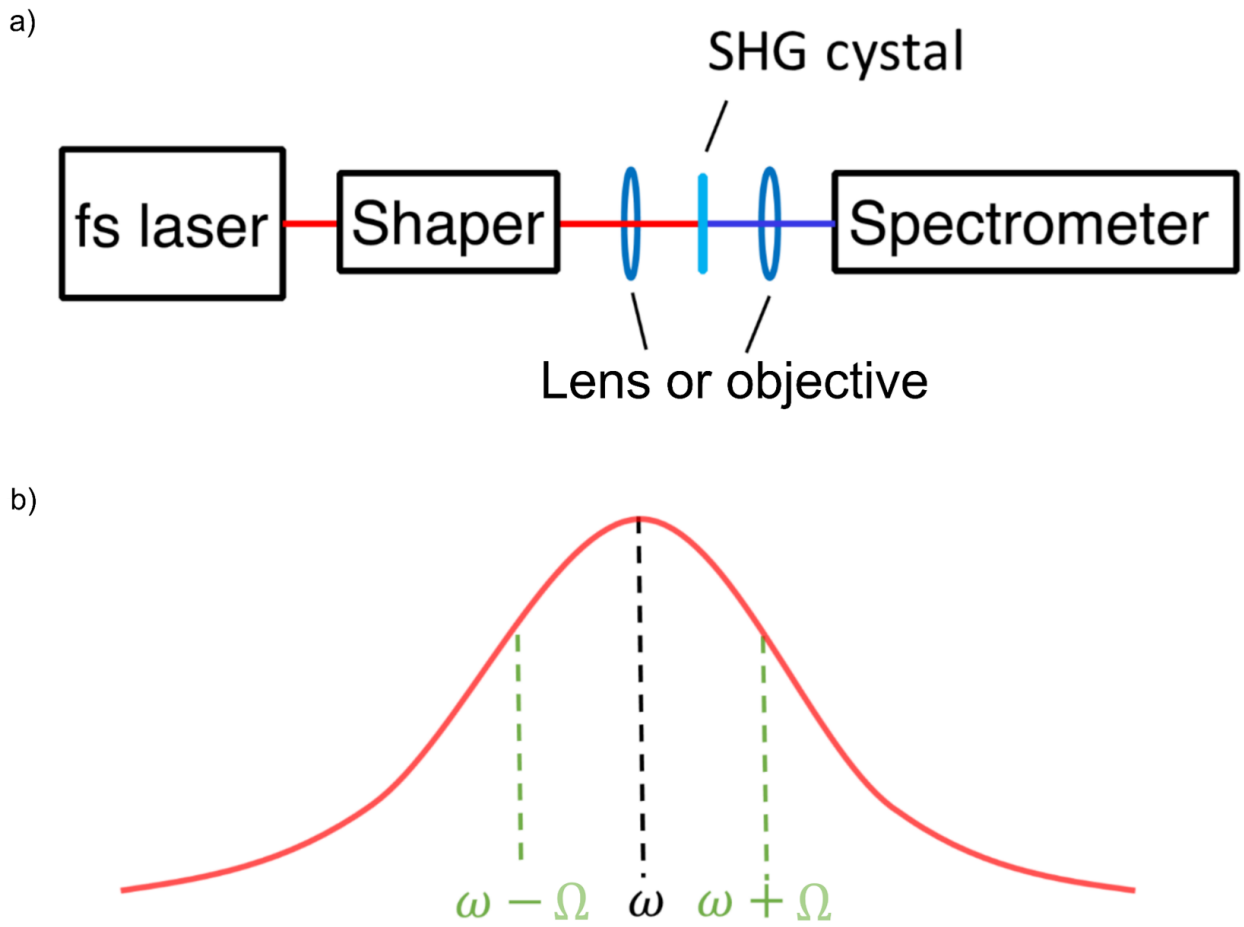

Figure 24: Summary of multiphoton intrapulse interference phase scan (MIIPS) setup. (a) Diagram of MIIPS setup. In this work, objectives are used instead of lenses. (b) Interference between different frequency modes of the SHG spectrum.

2.4.4.1 **MIIPS Compensation Algorithm**

MIIPS, or multiphoton intrapulse interference phase scan, is a recently developed and popular method for both characterizing and compensating ultrafast pulses[44,45]. As compared to other pulse compensation methods, such as FROG (frequency-resolved optical gating[46]) and SPIDER (spectral phase interferometry for direct electric field reconstruction[47]) MIIPS offers the advantage of being a single-beam method, i.e., that there is no interferometry required. It utilizes a pulse-shaper-based feedback loop, in which the second harmonic generated (SHG) signal from a BBO signal is fed into an optimization algorithm which sends commands to the pulse shaper's active modulator array. Since its introduction, MIIPS has demonstrated prominent accuracy and versatility, being quite fruitful in fields like selective microscopic chemical probing, multiphoton microscopy, and functional imaging.

A simplified diagram of the basic MIIPS setup is shown in Figure 24(a). The spectral phase of ultrafast pulses is controlled by a pulse shaper. The pulse shaper output is sent to a nonlinear beta barium borate (BBO) crystal. The resulting SHG spectrum is collected by a spectrometer and sent as a feedback signal to a computer algorithm designed to compress the distorted pulse.Nonlinear optical processes, such as SHG, are sensitive to the second derivative of the spectral phase of the excitation pulse. The generated nonlinear signal is proportional to the product of the amplitude of the input light with a complex phase term. MIIPS takes advantage of the dependence of SHG to this phase term, which denotes the spectral phase across the pulse, to find this unknown phase and compensate it. For transform-limited pulses (pulses with spectral phase $\varphi = constant$ across the bandwidth), the SHG signal from the BBO crystal is maximized, as the oscillatory phase term in Equation 7 is equal to 1:

$$S^{(2)}(2\omega) \propto \left| \int |E(\omega+\Omega)||E(\omega-\Omega)| e^{i(\varphi(\omega+\Omega)+\varphi(\omega-\Omega))}\, d\Omega \right|^2 \quad \textbf{Equation 7}$$

We can Taylor expand the phase modulation term for frequencies around ω:

$$\varphi(\omega+\Omega) + \varphi(\omega-\Omega) \quad \textbf{Equation 8}$$
$$= 2\varphi(\omega) + \varphi''(\omega)\Omega^2 + \cdots + \frac{2}{(2n)!}\frac{d^{2n}\varphi(\omega)}{d(\omega)^{2n}}(\omega)\Omega^{2n}$$

To first order approximation, then, the SHG spectrum has a maximum when the spectral phase is constant and the second order phase distortion is zero, $\varphi''(\omega) = 0$. MIIPS measures the unknown spectral phase acquired by the pulse, $\phi(\omega)$, by successively imposing a parametrized reference function to the pulse. This additional phase leads to a total phase across the pulse of:

$$\phi(\omega) = \varphi(\omega) + [-f(\delta,\omega)] \quad \textbf{Equation 9}$$

where $f(\omega, p)$ is the reference function. Therefore, when

$$\phi''^{(\omega_i)} = \varphi''^{(\omega_i)} + \left[-f''^{(\omega_i,p)}\right] = 0, \text{ or } \varphi''^{(\omega_i)} = -f''(\delta,\omega_i), \quad \textbf{Equation 10}$$

the SHG at a particular frequency is maximized. Typically, the reference function is sinusoidal:

$$f(\delta,\omega) = \alpha\sin(\gamma\omega - \delta) \quad \textbf{Equation 11}$$

where the variables α and γ are fixed, with $\alpha = n\pi$, n integer, γ is set to the estimated transform-limited duration of the input pulses in femtoseconds, and the phase offset δ is scanned in a range of $\delta \in [0,\ 4\pi]$ during each iteration of the MIIPS algorithm. The second derivative takes the form

$$f''^{(\delta,\omega)} = -\alpha\gamma^2\sin(\gamma\omega - \delta). \quad \textbf{Equation 12}$$

A SHG spectrum is captured at each value of δ. The spectra are plotted together in a two-dimensional intensity plot vs. frequency ω (or wavelength) and δ to obtain a MIIPS trace, as shown in Figure 25.

An experimentally obtained trace for our setup is shown in Figure 26. The MIIPS compensation is obtained with the BBO crystal and spectrometer placed right before the input to the Michelson interferometer, as shown in Figure 13. The experimentally obtained MIIPS trace differs than the theoretically ideal trace, which is likely due to the non-Gaussian shape of the input pulses in the frequency domain.

The laser pulse is not characterized at the point of the time-domain photovoltage measurement, which is at the sample surface. The location where the BBO crystal and spectrometer are placed within the experimental setup (in the beam path right before the entrance to the interferometer) is labeled in Figure 13. Though the obtained MIIPS compensation does not perfectly account for pulse dispersion that arises while the pulse travels through the Michelson interferometer, the interferometer has pre-compensation plates placed within each arm to compensate for additional dispersion, as shown in Figure 14.

In the future, we aim to achieve pulse characterization and compensation at the point of measurement. Specifically, we believe that the nonlinear response of LAO/STO nanojunctions may serve as a feedback mechanism which can replace the second harmonic generation from a macroscopic nonlinear crystal within the algorithm. If this is the case, the second harmonic signal from the LAO/STO nanojunction will be maximized when the spectral phase is constant across the bandwidth of the broadband pulse. Software and hardware upgrades which will enable the proposed experiments are currently underway.

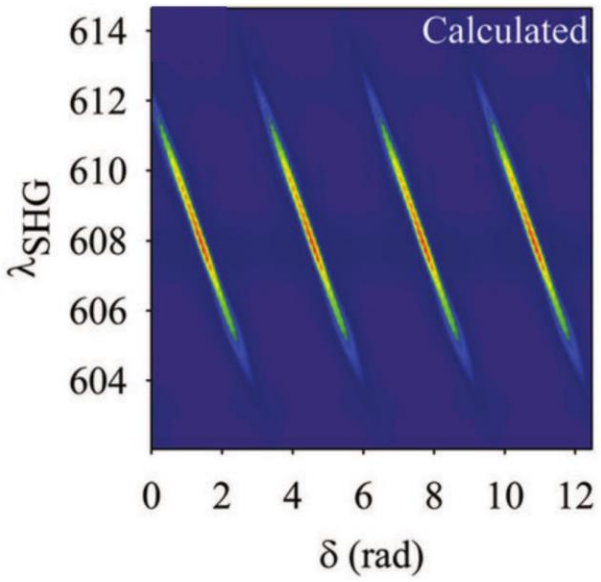

Figure 25: Theoretical MIIPS trace for transform-limited pulses. Adapted from Gamouras *et al*.[48]

As discussed above, the SHG is maximized when $\phi''(\omega) = 0$, or $\varphi''^{(\omega_i)} = -f''(\delta, \omega_i)$. Since $f''(\delta, \omega)$ is known, the unknown spectral phase $\varphi(\omega)$ can be easily retrieved by taking a double integral of $f''(\delta, \omega)$ along the maximal MIIPS trace with respect to frequency. This retrieved $\varphi(\omega)$ value is then added to the input pulses, or compensated, by the pulse shaper, and the next MIIPS iteration begins to obtain the remaining phase distortions. When the pulse is fully compensated, its remaining second-order phase distortion should vanish, leading to

$$\gamma\omega - \delta = n\pi, \qquad \textbf{Equation 13}$$

so that the ideal final MIIPS trace will follow parallel lines with a slope of $1/\gamma$ and separated by π. After several iterations, the spectral phase of the distorted pulse is accurately obtained, and the compensating phase can be applied by the pulse shaper at any time to recover a transform-limited pulse.

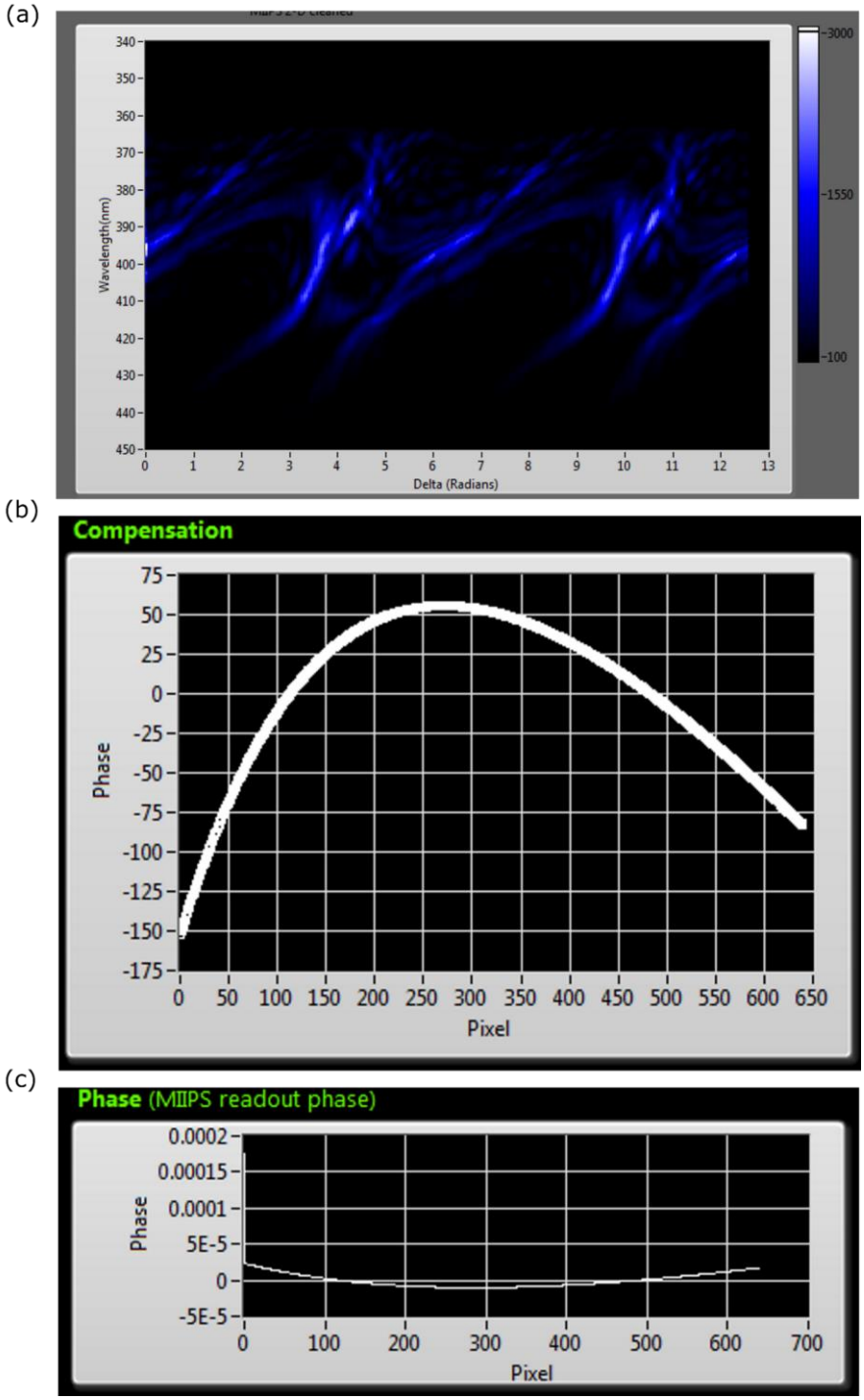

Figure 26: Experimentally obtained MIIPS compensation.(a) Experimentally obtained MIIPS trace after multiple iterations, (b) phase compensation calculated from the trace, and (c) the spectral phase across the ultrfast pulse after compensation.

2.4.4.2 **Verifying MIIPS Compensation with SHG**

To verify the accuracy of the experimentally obtained MIIPS trace, we applied a step-function phase modulation across the ultrafast pulses, as shown in Figure 27(b), both with and without the obtained MIIPS compensation phase added. The modeled SHG spectrum for the step-function phase modulation is obtained from Equation 7 and is plotted against the experimentally obtained SHG spectra for the compensated (Figure 27(c)) and uncompensated (Figure 27(d)). The compensated SHG spectrum clearly matches the theoretical model, whereas the uncompensated spectrum differs greatly. These results confirm the accuracy of the MIIPS compensation obtained for our experimental setup. As with the obtained MIIPS trace, differences between the theoretical model and the experimentally obtained spectrum can likely be attributed to the non-Gaussian shape of the input pulses in the frequency domain.

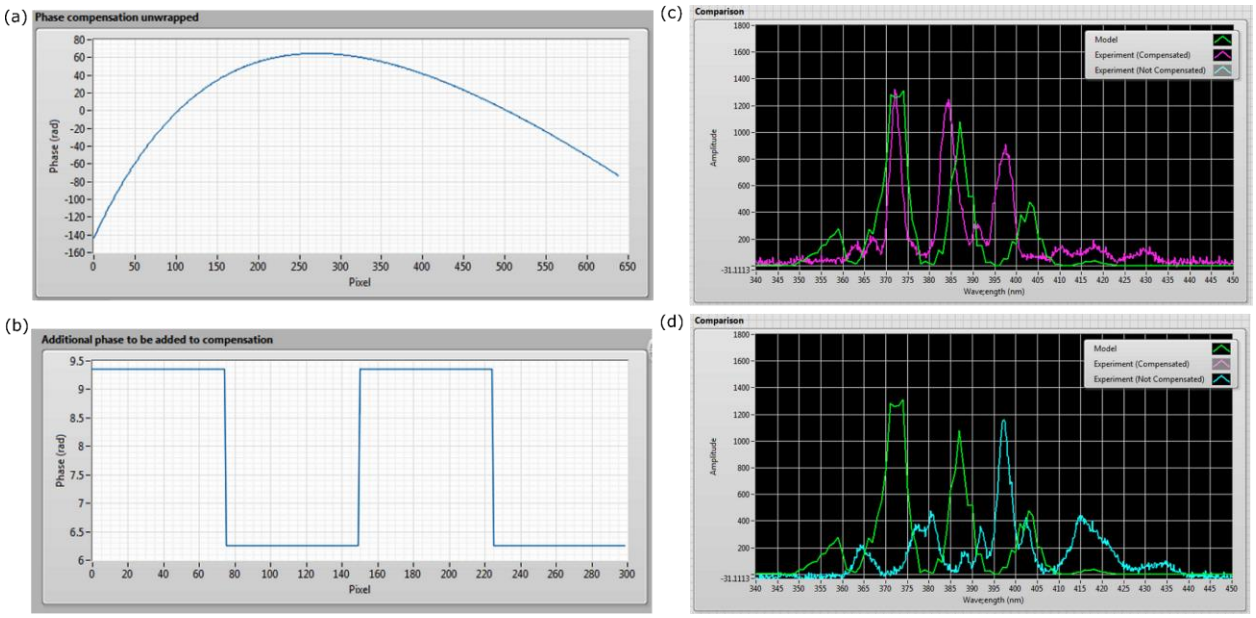

Figure 27: Testing MIIPS compensation with SHG feedback. (a) Experimentally obtained MIIPS compensation and (b) addiitonal phase modulation `to be applied across the input pulse. Theoretical and experimental output SHG spectrum both (c) with compenstion and (d) without compensation.

2.5 Optical Cryostat

2.5.1 Working Principle

Ultrafast optical responses are measured at cryogenic temperatures using a Montana Instruments optical cryostat. It is a closed-cycle operation system, with a temperature range from 4 to 350 K. The temperature stability is within 10 mK and vibration stability is within 5 nm. It is also equipped with radiation-blocked optical windows and electronic connections, providing both optical and electronic access to the sample. The system has four main components: a compressor, a control unit, the cryostat with a sample chamber, and a computer user interface. A schematic block diagram of the system is shown in Figure 28.

Cooling power is provided by a two-stage Gifford-McMahon cryo-cooler. The cryo-cooler is part of a closed-loop flow of helium which is pressurized by a separate variable-flow helium Compressor. The cryocooler has two principal stages, each equipped with thermometers and heaters to monitor and accurately control the temperature. The first of these stages is thermally coupled to a thermal radiation shield surrounding the sample and mount in the sample chamber. The second stage is thermally coupled to the platform and sample mount in the Sample Chamber. The sample chamber consists of the unit platform, the configurable sample holder, the surrounding radiation shield with its inner “cold” windows, and the outer window assembly with its “warm” windows. A vacuum pump in the control unit evacuates the air from the sample chamber to achieve a rough vacuum level. A secondary “cryo-pump” achieves a high vacuum level by trapping vapor remaining in the vacuum space. During cooldown, the sample platform temperature lags the

coldest temperature in the Cryostat so that the charcoal adsorbers achieve a hard vacuum before the sample platform is cold. This keeps the sample free from condensation.

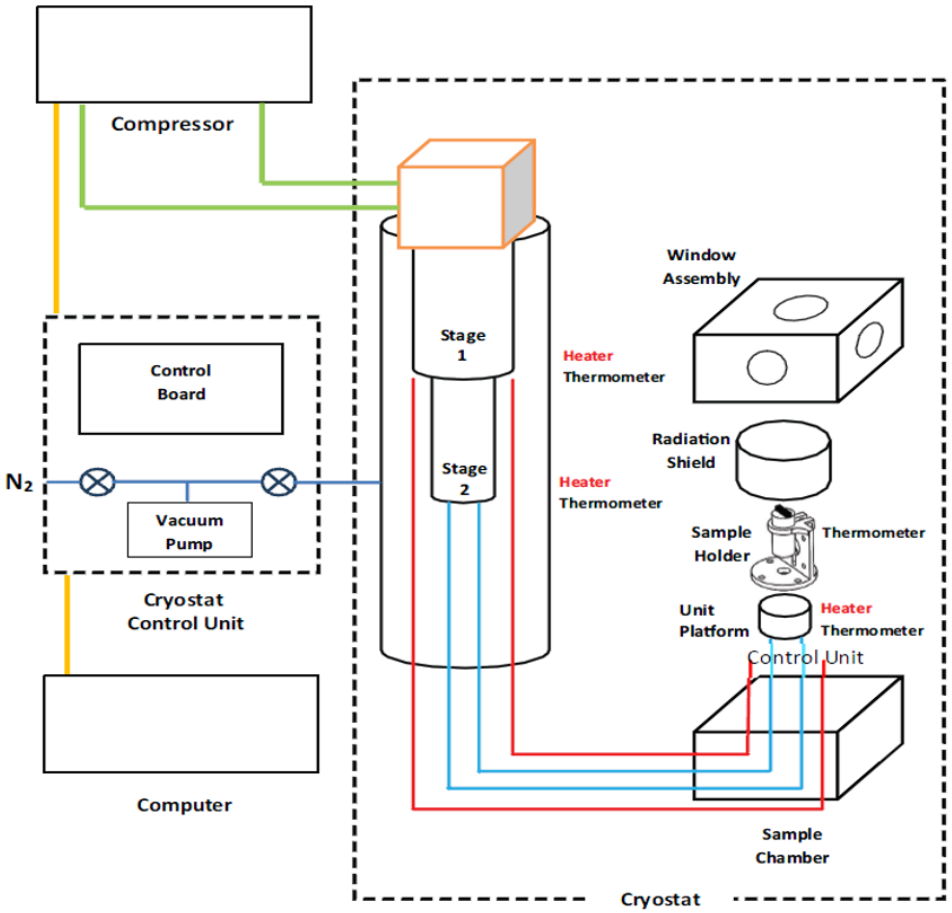

Figure 28: Cryostat Components.

Mechanical vibrations from the cryo-cooler are isolated both from the table and the sample mount. The Sample Chamber and Cryostat frame are rigidly mounted to the table. The cooling tower portion of the frame "floats" within the enclosure, to keep vibrations from passing through to the Sample Chamber. Thermal fluctuations are damped using both active and passive techniques. The sample platform also eliminates the effects of gross thermal contraction during cool down by using a thermal contraction-cancelling design. The benefit of this design is that once

room temperature alignment with optics is done, no further alignment should be required for each temperature of operation.

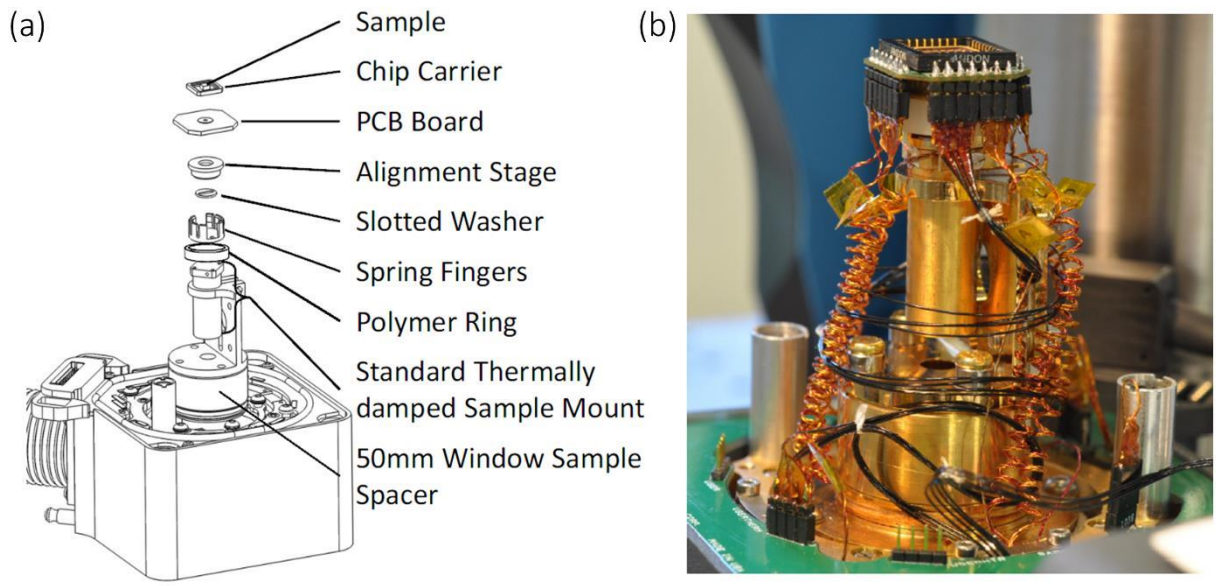

Figure 29: Cryostation Sample Chamber. (a) Chamber geometry and (b) electrical connections.

2.5.2 Sample Chamber and Connections

The sample is placed on a chip carrier that is attached to a PCB board (Figure 29 (a)). The materials used within the printed circuit board (PCB) which connects the LAO/STO sample to the cold space of the Montana Instruments cryostation are not reported by Montana Instruments. That being said, the LAO/STO sample is separated from the cold stage PCB by a chip carrier. The material comprising the chip carrier is a glass-reinforced epoxy laminate material, named FR-4. This is a composite material composed of woven fiberglass cloth with an epoxy resin, where "FR" stands for "flame-resistant." The thickness of the chip carrier is 0.24 cm, and the material is reported to have a dielectric constant of 3.9 - 4.7.

The sample mount can be positioned facing upward or sideways. Light can enter the sample chamber through any one of the windows, and the reflection or transmission after sample can be collected from the same or a different window, depending on the experimental scheme and sample mount orientation. Electronic properties of the sample are measured through 28 electrical feed-throughs, as shown Figure 29(b). In our setup the yellow spring wires are replaced by a ribbon cable and Fisher connector to enable electrical connection to external instruments.

An optional thermal radiation shield can be placed around the sample, and is thermally coupled to the first cryocooler stage. The sample is mounted to a post that is thermally coupled to the second stage. A vacuum is created in the chamber to thermally isolate the sample, radiation shield, and outer shell. A PID feedback loop controls the helium flow and the heater power to maintain a set temperature.

3.0 Optical Response of LAO/STO Nanoscale Junctions

3.1 Previous work and theoretical background

The experiments discussed in this section are the foundational experiments establishing and characterizing the ultrafast response of LAO/STO nanojunctions. The experimental setup discussed here is no longer in use. Full details of the following section can be found in Yanjun Ma's doctoral dissertation[49] , Irvin et al.[32] and Ma et al.[33].

3.1.1 Nanoscale photodetectorn

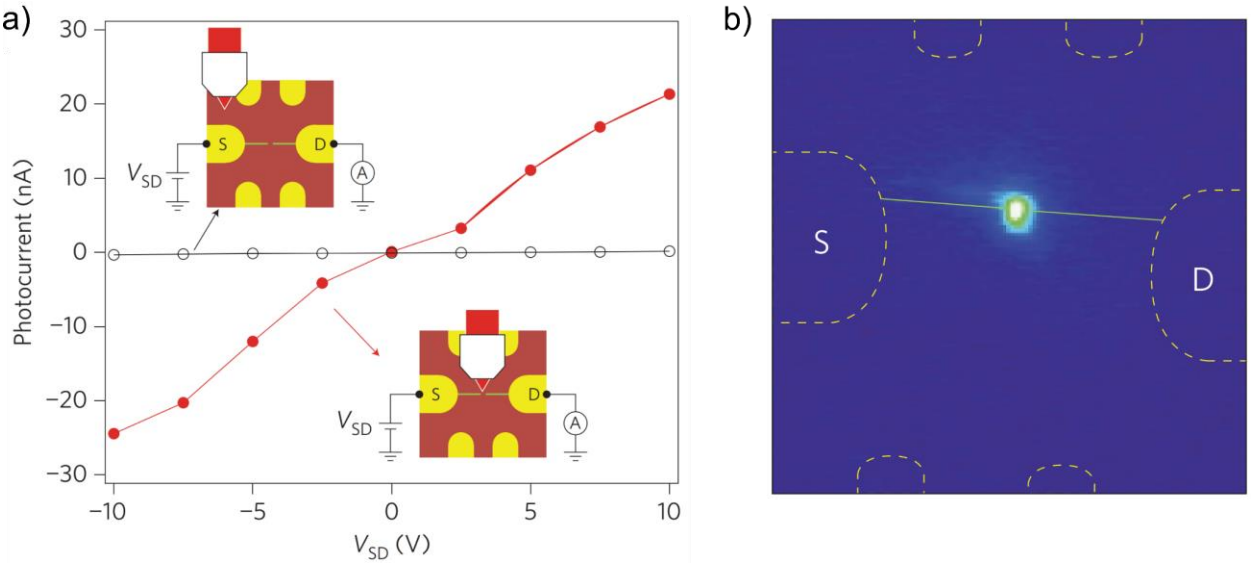

Figure 30: Nanoscale photodetector. (a) I-V curves across nanojunction when not illuminated (grey curve) and when light is focused on it (red curve.) (b) Scanning photovoltage microscopy image showing a strong, localized photovoltage response at the site of the nanojunction. Adapted from Irvin *et al.*[32]

C-AFM defined LAO/STO nanojunctions were previously shown to constitute nanoscale photodetectors, as summarized in Figure 30. I-V curves across a nanojunction show that when focused laser light overlaps with the device, there is a sharp increase in the photocurrent. The response is also highly localized in spaced; by measuring the generated photovoltage as a function of the (x,y) coordinate of the focused light spot, a scanning photovoltage microscopy image (Figure 30(b)) is generated. The scanning image reveals a strong, localized photovoltage response at the site of the nanojunction.

These nanoscale devices exhibit remarkably high gain for their size, in part because of the large electric fields produced in the gap region. The photoconductive response is electric field-tunable and spans (at least) the visible to-near-infrared regime. The physical mechanism resulting in photocurrent is likely the existence of in-gap electron states in STO. When the in-gap states are excited by vis-NIR light, they are excited to the conduction band, then swept across the junction by the source-drain bias field, as shown in Figure 32(d).

3.1.2 Ultrafast Nature of Nanojunction Response

The photoresponse of LAO/STO nanojunctions is also ultrafast in time. Figure 31(a) illustrates the (obsolete) experimental setup used in this chapter. An LAO/STO nanojunction is fabricated via c-AFM lithography, as described in Section 2.1.4. Ultrafast (30 fs) optical pulses from a home-built Ti: Sapphire laser are divided into "pump" and "probe" beams by a Mach Zehnder interferometer. Photoconductive properties of the device, located in an optical cryostat, are measured using a four-terminal geometry in which a voltage is applied between source (S) and drain (D) electrodes, as described in Section 2.3.4. All experiments are performed at 80 K except

where noted. In Figure 31(b), the diffraction-limited scanning photovoltage signal peak shows where the nanojunction is located. By allowing both beams to illuminate the nanojunction and scanning the optical delay line (ODL), dynamical information can be resolved via a time-domain photovoltage measurement. In Figure 31(c), when the chopper is off, interference fringes are observed; these are signatures of a field autocorrelation measurement. The lower envelope shows larger amplitude than the upper one; by turning the chopper on, lock-in detection can filter away the fast oscillations, leaving only the asymmetric envelope to be detected by averaging over a large number of measurements (Figure 31(d)). The time-domain response exhibits a full width at half-maximum (FWHM) of 31 fs. The spatial and temporal response of the device can be measured by repeating the time-resolved measurement at a regular two-dimensional array of locations.

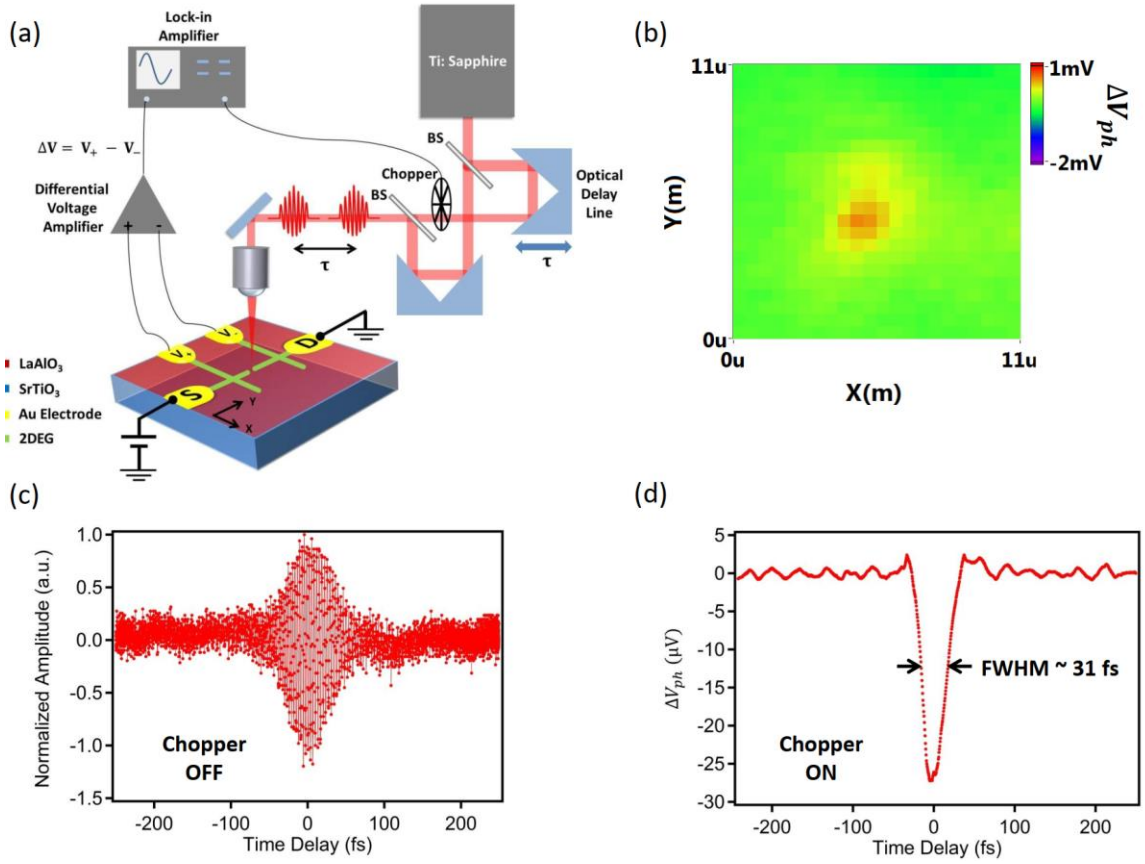

Figure 31: Broadband THz Generation Setup.(a) Experimental setup. (b) Localized photovoltage response as discussed above. (c) Time domain measurement showing signatures of a field autocorrelation. (d) Time domain measurement with chopper modulation revealing a lower envelope. Adapted from Ma *et al.*[33]

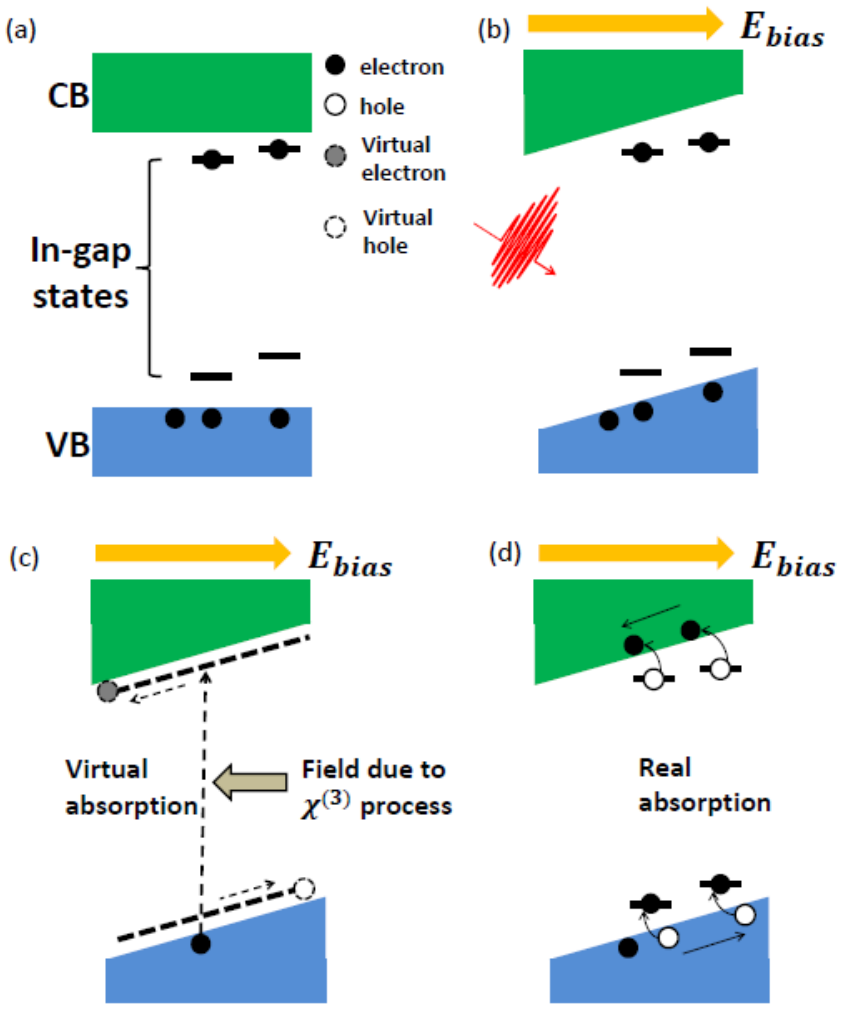

Figure 32: Physical Origin of Ultrafast Response. (a) Simplified image of LAO/STO band gap showing in-gap states. (b) The bands are bent from the applied DC bias. (c) Virtual absorption process. (d) Real absorption via in-gap electron states, which leads to photocurrent.

3.1.2.1 **Physical Origin of Ultrafast Response**

Several physical mechanisms must be considered to understand the origin of the LAO/STO nanojunction ultrafast response. To start, processes involving resonant optical absorption and carrier relaxation can be ruled out, because the reported lifetime for photo-excited carriers in $SrTiO_3$ is on the order of a nanosecond. Nonlinear $\chi^{(2)}$ or $\chi^{(3)}$ processes, on the other hand, have

a much greater inherent bandwidth. $SrTiO_3$ is a centrosymmetric crystal that should not exhibit a bulk second-order nonlinear response. Because inversion symmetry is broken at the interface of LAO/STO, $\chi^{(2)}$ processes can exist. However, the ultrafast response measured here is highly localized at the junction and can be tuned by external electric field; hence, intrinsic processes are unlikely to play an important role. The electric field is strongly confined around the nanojunction and can be on the order of 10^6 V/cm. Therefore, it is believed that the observed ultrafast response results from a $\chi^{(3)}$ process involving one quasi-static local field across the junction and two optical fields:

$$P_{NL}^{i} = \varepsilon_0 \chi_{ijkl}^{(3)}(0,0,\omega,-\omega) E_{bias}^{j} E^{k}(\omega) E^{l}(-\omega) \qquad \textbf{Equation 14}$$

where P_{NL}^{i} is the nonlinear polarization, $\chi_{ijkl}^{(3)}$ is the third-order susceptibility at the nanojunction, E_{bias}^{i} is the electric field across the nanojunction, and $E^{i}(\omega)$ is the optical field (i, j, k, l = x, y, z).

The nonlinear response of the nanojunction is analogous to that of GaAs crystals[50,51] excited by off-resonance irradiance. The incident light in the following experiments has a photon energy ~1.48 eV. STO has direct and indirect band gaps of 3.75 eV and 3.25 eV, respectively; hence, the interaction between non-resonant photons and valence electrons in STO can be described as a virtual absorption process. Physically, the picture indicates that when valence electrons interact with non-resonant photons, the electrons remain bound but are shifted from their equilibrium positions by the optical electric field. As a result, a transient dipole moment is

produced via a $\chi^{(3)}$ process that reduces the static external field (Figure 32(c)). Because this process involves no real absorption, a FWHM comparable to that of the laser pulse is expected.

3.1.3 Slow Response

In addition to the ultrafast response, illumination of LAO/STO nanojunctions also produces a time-averaged, or slow, response, which manifests as an overall offset in the bias-dependent curves shown in Figure 32(a). This offset can be attributed to the absorption of photons by electrons occupying the in-gap states in STO. Previous experiments[52-55] have shown that STO, especially when subjected to growth of $LaAlO_3$, can form deep traps from either oxygen vacancies[56-59] or unintentional doping of STO substrate[60]. These in-gap states, which are distributed from the top of the valence band to the bottom of the conduction band[61], can trap electrons, resulting in the absorption of infrared light[61,62]. Prior investigations of the wavelength dependence of the photoconductive response and the Stark shifting under electric fields[63] is in agreement with the picture that incoming near-infrared photons can be absorbed by electrons residing in states within the STO band gap. A schematic of this energy-band diagram is shown in Figure 32(d). In the presence of an external electric field, electrons and holes excited in this way are separated and result in photoconductivity. Because of this separation, charge carriers cannot recombine quickly. The net effect is a constant background offset.

3.1.4 Temperature Dependence

Motivated by the fact that STO undergoes several structural phase transitions[64], the temperature-dependence of the ultrafast response is measured from 5 K to room temperature (290 K). As the temperature is decreased from 290 K to 30 K, the amplitude of the signal generally increases. This observation is consistent with the Curie-Weiss scaling of both the dielectric constant and nonlinear susceptibility of $SrTiO_3$ with temperature[65,66]. The mechanism responsible for the abrupt drop between 25 K and 30 K has not been determined. In Ref. [66] a minimum of $\chi^{(3)}$ is found around 30 K, however, this feature is only observed when the electric field across the sample is lower than 1.5 kV/cm[66]. The electric field values within our nanojunction devices are several orders of magnitude higher, so it is possible that the abrupt change might be related to a local electric-field-induced structural phase transition within the $SrTiO_3$ from tetragonal to orthorhombic[64].

3.1.5 Polarization of Ultrafast Response

Polarization dependence provides useful information regarding the symmetry of nonlinear optical coefficients. The Y-axis is defined to be along the vertical direction of the input light polarization. and horizontal direction is along the X-axis, as shown in Figure 33. Measurements are performed with V_{SD} = -1 V and $I_{ave} \approx$ 50 kW/cm^2. When the polarization of both pump and probe are parallel, a time-resolved signal is detected. When the pump and probe polarizations are mutually perpendicular, the time-resolved signal is suppressed. The observed polarization dependence can be explained by the symmetry that STO possesses: non-vanishing $\chi^{(3)}$ parameters

constrain which light polarizations generate nonzero P_{NL}. Specifically, since STO belongs to *m3m* symmetry group, it has the following non-vanishing $\chi^{(3)}$ parameters:

$$\boldsymbol{\chi^{(3)}_{xxxx} = \chi^{(3)}_{yyyy} = \chi^{(3)}_{zzzz}}$$

$$\boldsymbol{\chi^{(3)}_{xxyy} = \chi^{(3)}_{yyxx} = \chi^{(3)}_{xxzz} = \chi^{(3)}_{zzxx} = \chi^{(3)}_{yyzz} = \chi^{(3)}_{zzyy}}$$

$$\boldsymbol{\chi^{(3)}_{xyxy} = \chi^{(3)}_{yxyx} = \chi^{(3)}_{xzxz} = \chi^{(3)}_{zxzx} = \chi^{(3)}_{yzyz} = \chi^{(3)}_{zyzy}}$$

$$\boldsymbol{\chi^{(3)}_{xyyx} = \chi^{(3)}_{yxxy} = \chi^{(3)}_{xzzx} = \chi^{(3)}_{zxxz} = \chi^{(3)}_{yzzy} = \chi^{(3)}_{zyyz}}$$

Equation 15

In our experiments, the light incident to the junction is normal to the sample, so the electric field of the light is in the transverse direction. Our samples are grown and processed in such a way that the in-plane principal axes of STO are along the X and Y direction as shown in Figure 33. The observed polarization dependence can therefore be explained as follows: The external bias field is applied in Y direction. The induced field, caused by the separation of virtual holes and virtual electrons, then must be in $-Y$ direction. This means that only the $\boldsymbol{\chi^{(3)}_{yyyy}}$ and $\boldsymbol{\chi^{(3)}_{yyxx}}$ terms are relevant. However, both terms require the optical field to be in parallel (either in X or Y direction), otherwise the $\chi^{(3)}$ coefficient will be zero and therefore no virtual absorption can occur:

$$P^{y}_{NL}(\omega_1 - \omega_2) \propto \chi^{(3)}_{yyyy} E^{y}_{bias} E^{y}_{opt}(\omega_1) E^{y}_{opt}(\omega_2)$$

$$P^{y}_{NL}(\omega_1 - \omega_2) \propto \chi^{(3)}_{yyxx} E^{y}_{bias} E^{x}_{opt}(\omega_1) E^{x}_{opt}(\omega_2).$$

Equation 16

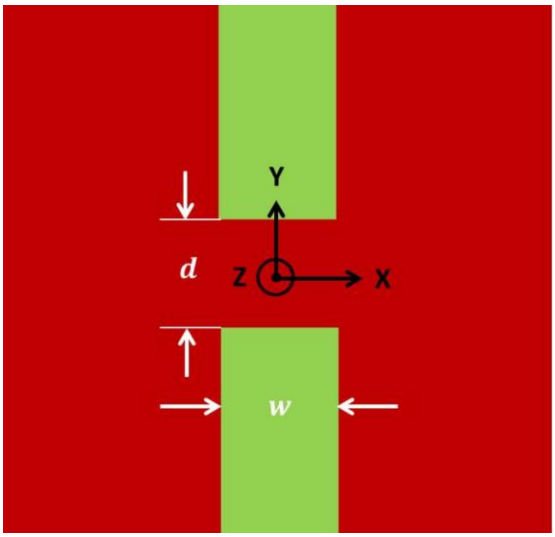

Figure 33: Geometry of LAO/STO Nanojunction.

3.2 100 THz Difference Frequency Generation

Electromagnetic waves at terahertz (THz) frequencies allow resonant interactions with matter through various intrinsic low-energy excitations, revealing information related to lattice, charge and spin degrees of freedom. In the past few decades, extensive research efforts have focused on developing narrow-band THz radiation sources in both far-infrared (<10 THz) and midinfrared (10-100 THz) regimes, due to their potential to provide insight into the fundamental physics of matter by selective excitations of different resonances. For a large number of applications, including spectroscopy, inspection, communication, and coherent control, tunability of the narrow-band THz radiation is required. On the other hand, THz techniques are also often limited by spatial resolution. Owing to the relatively long wavelength of THz radiation, diffraction usually limits the spatial resolution to the order of 10- 100 um, making it difficult to resolve features much below this scale. Several techniques have been pursued to reach a nanometer-scale

spatial resolution, such as combining THz radiation with scattering-type near-field scanning optical microscopy or scanning tunneling microscopy. However, to date, a continuously tunable, quasi-monochromatic THz source that can cover both the far- and mid-infrared regime with sub-10 nm spatial resolution is not available.

Here, we report >100 THz bandwidth selective difference frequency generation at $LaAlO_3/SrTiO_3$ (LAO/STO) nanojunctions through femtosecond optical pulse shaping. Selected frequency components of a sub-7 fs ultrafast pulse are mixed at the nanojunction through the third order nonlinear effect in STO, and their frequency difference results in narrow-band THz emission. By controlling the selected frequency components, the frequency of narrow-band THz emission can be tuned from far-infrared to mid-infrared regime. The spatial resolution of this THz source is determined by the nanojunction size, typically around 10 nm, but can be as small as 2-3 nm, thus realizing an ultra-broad bandwidth, continuously tunable, quasi-monochromatic THz source with a spatial resolution comparable to a single nanoparticle or even a single molecule.

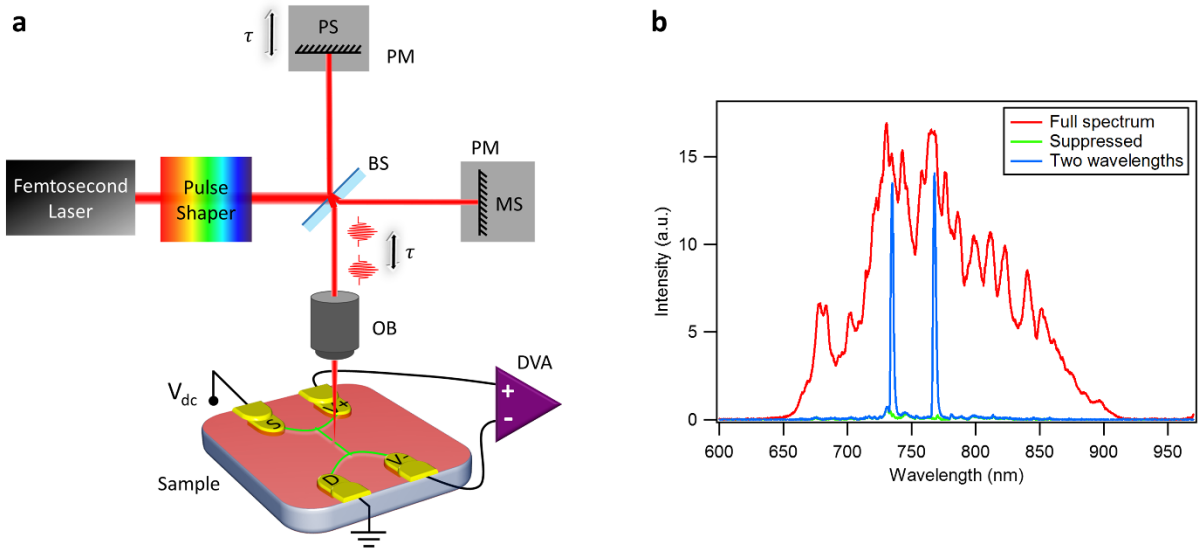

Figure 34: Broadband Pulse Shaping Experimental Setup. . (a) Michelson interferometer setup and (b) Spectrometer images showing the amplitude modulation achievable with our pulse shaper.

3.2.1 Experimental Results

As a review, Figure 34(a) shows the schematic drawing of the experimental setup. Ultrafast pulses from a sub-7 fs Ti: Sapphire oscillator (Spectra-Physics Rainbow 2 UHP) are directed into an optical pulse shaper based on a dual-mask spatial light modulator (SLM, Jenoptik SLM-S640d), where different wavelengths are spatially separated by a grating and focused onto different pixels of the SLM. Both the amplitude and the phase of the ultrafast pulse can be controlled independently. Here we focus on spectral amplitude control. After the pulse shaper, the manipulated pulses are redirected to our compact Michelson interferometer and then focused onto a nanojunction device located in an optical cryostat at $T = 80$ K. Time domain photovoltage measurements are performed with the shaped the light focused on it, while a DC bias voltage (V_{SD} = -550 mV) is applied across the junction.

Figure 34(b) shows an example of the spectral amplitude control achievable by the pulse shaper. The red curve represents the full spectrum from the Ti:Sapphire oscillator without any spectral amplitude manipulation. A broad spectrum ranging from 650 nm to 920 nm is measured by a spectrometer. By applying an appropriate voltage to each pixel of the SLM, the output at all wavelengths can be efficiently suppressed (green curve). We can then specifically select one, two or a few wavelengths to pass through the SLM, while keeping all the other wavelengths suppressed. The blue curve shows a configuration in which light at 735 nm and 768 nm is allowed to pass through the SLM, while other wavelengths are suppressed.

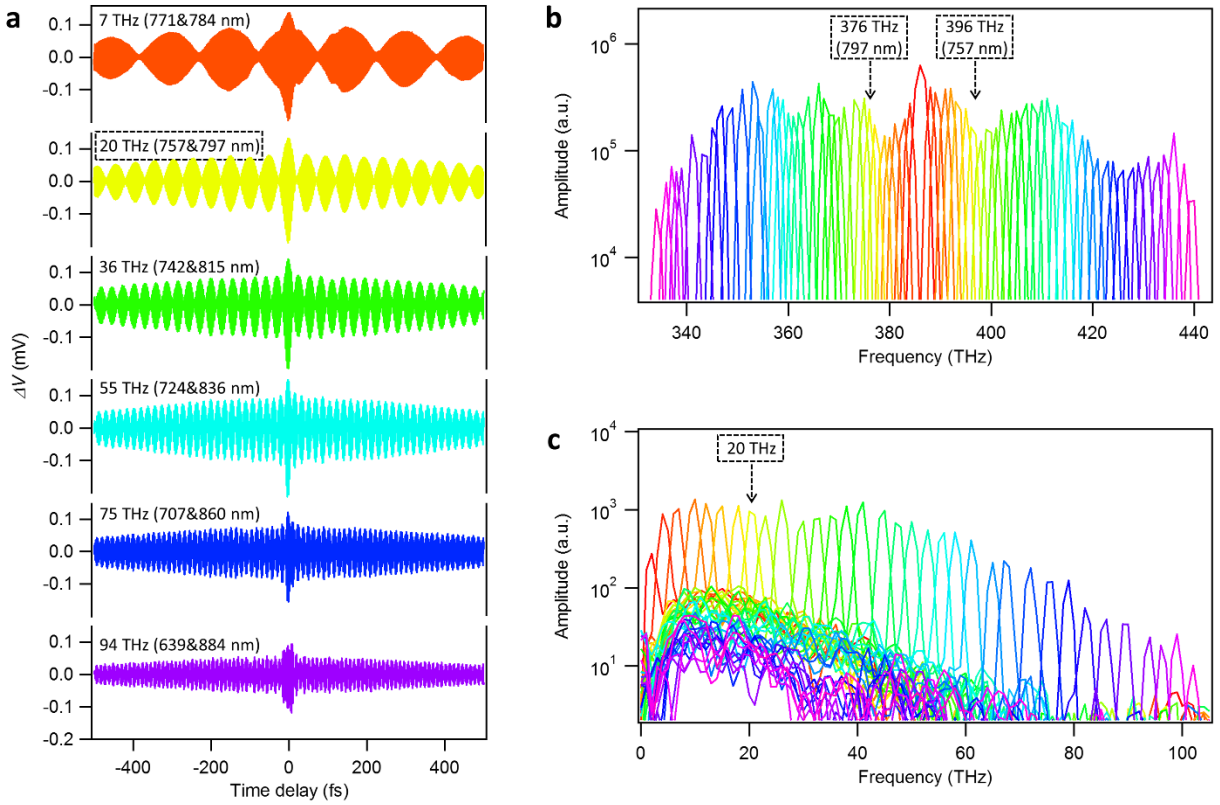

Figure 35: Tunable Broadband Difference Frequency Generation. (a) Six example time domain signals for different input frequency pairs. (b) Linear response of the nanojunction showing both input frequencies. (c) Difference frequency generation ranging from 1 to >100 THz.

To demonstrate the ultra-broad bandwidth selective difference frequency generation capability of the LAO/STO nanojunction, we perform nonlinear wavelength mixing experiments. We select 35 different fundamental wavelength pairs with the frequency difference within each pair ranging from 2 THz to 106 THz. The average input power is on the order of 10 μW. For each fundamental wavelength pair, the amplified photovoltage ΔV is recorded as the optical delay line varies from τ =-500 fs to +500 fs. Each measurement is repeated 40 times for averaging purposes. Figure 35(a) shows six representative averaged time-domain signals. A beating envelope can be clearly seen in each time-domain signal. It is important to note that the lower half of the envelope has a larger amplitude than the upper half. A constant background has been subtracted for each curve, which originates from the DC bias voltage as well as from persistent photoconductance by mid-gap states in STO.

Power spectra are calculated from the time-domain signals to reveal the frequency components. The linear (LNR) region of the power spectrum is shown in Figure 35(b) and the difference frequency generated (DFG) region is shown in panel (c). Different curves are distinguished by color, and all plots in Figure 35 share the same color code. As an example, a fundamental wavelength pair of 757 nm (396 THz) and 797 nm (376 THz) is selected from the ultrafast pulse by the pulse shaper to generate a narrowband emission at 20 THz. The corresponding time-domain signal is measured and plotted in Figure 35(a) (yellow curve), and its power spectrum clearly shows both the fundamental wavelength pair and a 20 THz difference frequency. The measured linewidth of the narrow-band THz generation (~2 THz on average) in

this configuration is limited by the spectral resolution of the pulse shaper as well as the total travel range of the optical delay line (1 ps, which corresponds to a 1 THz resolution).

3.2.1.1 **Sum-frequency mixing**

In addition to difference frequency generation, LAO/STO nanojunctions also produce sum frequencies of the two input frequencies ω_1 and ω_2. The sum frequency generation response in Figure 36 shows that frequencies are generated at $\omega_1 + \omega_2$, $\omega_1 + \omega_2 - \Delta\omega$, and $\omega_1 + \omega_2 + \Delta\omega$, where $\Delta\omega$ is the difference frequency.

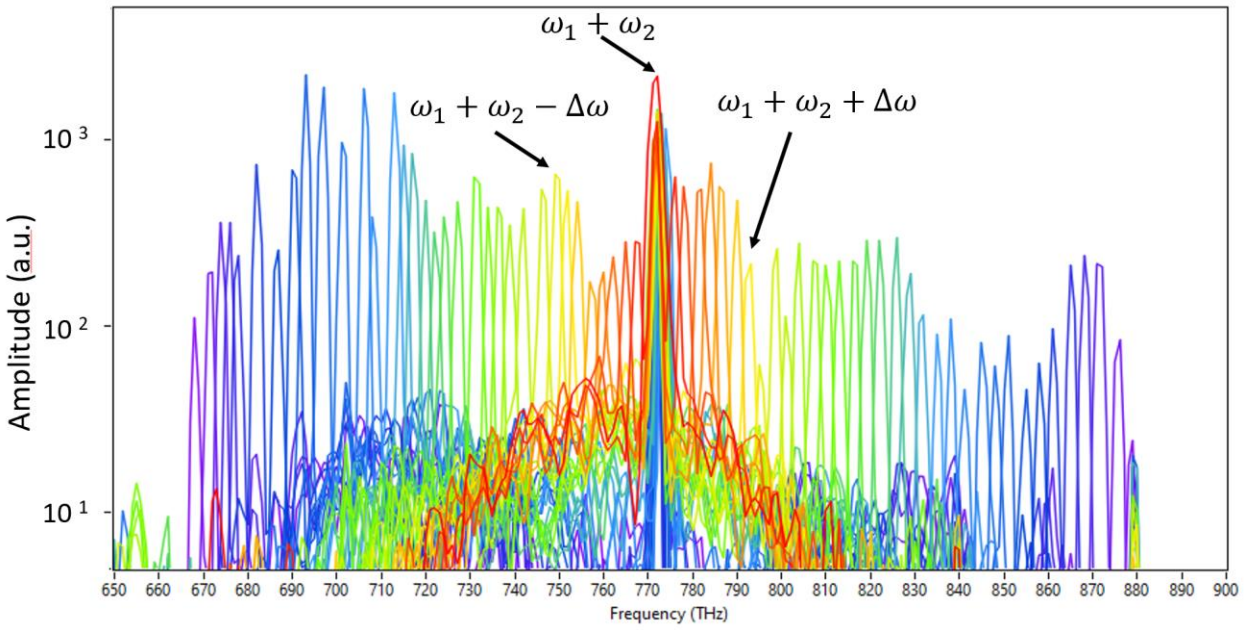

Figure 36: Sum Frequency generation in LAO/STO nanojunctions.

3.2.2 Theoretical Model

Due to the large bandgaps of both LAO and STO, the input photon energies in the experiments are not sufficient to excite valence electrons to the conduction band. Though mid-gap

states do exist in STO, the reported lifetime for STO photo-excited carriers is at least on the order of nanoseconds, which is not relevant for the time scales involved here. On the other hand, the nonlinear optical process of optical rectification is known to be able to generate a broadband THz field. The experiments reported here are performed at temperature T = 80 K. Below T =105 K, bulk STO undergoes a cubic-to-tetragonal transition; however, the STO remains centrosymmetric, with a vanishing second-order susceptibility $\chi^{(2)}$. Even though the breaking of inversion symmetry at the interface of LAO/STO can produce a $\chi^{(2)}$ response, the two-dimensional nature of the interface makes it unlikely for the second-order nonlinear effect to play a dominant role. In contrast, the third-order susceptibility $\chi^{(3)}$ is known to be exceedingly large for bulk STO. It has been experimentally demonstrated that the ultrafast photoconductive response at the LAO/STO nanojunction is DC electric field-tunable and spatially confined in the region of the nanojunction. These prior results suggest that the third-order nonlinear effect is the leading mechanism for wave mixing. The nanoscale dimension (~10 nm) of the nanojunction provides a strong confinement of the DC bias field, resulting in a strong electric field of 5.5×10^5 V/cm for V_{SD} = -550 mV. In this sense, the third-order nonlinear process can also be viewed as a DC bias field-mediated second-order nonlinear process. The electric field of the fundamental wavelength pair selected by the pulse shaper can be expressed as

$$E_{input} = E_1 \cos(\omega_1 t) + E_2 \cos(\omega_2 t) \qquad \textbf{Equation 17}$$

where E_1 and E_2 are the amplitude, and ω_1 and ω_2 are the angular frequency of the plane wave for the two fundamental wavelengths, respectively. The intensity of this input field E_{input} is then divided equally by a 50/50 ultrafast beam splitter. An additional time delay τ is added to the

reflected beam by scanning the piezoelectric stage, compared to the transmitted beam. The electric fields for the transmitted beam E_{tran} and the reflected beam E_{refl} are thus given by

$$E_{tran} = \frac{1}{\sqrt{2}}[E_1 \cos(\omega_1 t) + E_2 \cos(\omega_2 t)] \quad \textbf{Equation 18}$$

$$E_{refl} = \frac{1}{\sqrt{2}}\big[E_1 \cos\big(\omega_1(t-\tau)\big) + E_2 \cos\big(\omega_2(t-\tau)\big)\big]. \quad \textbf{Equation 19}$$

The two beams are re-combined by the same beam splitter, and focused onto the LAO/STO nanojunction, yielding an optical electric field E_{opt} in the following form:

$$E_{opt} = \frac{1}{2}(E_1 \cos(\omega_1 t) + E_2 \cos(\omega_2 t) + E_1 \cos\big(\omega_1(t-\tau)\big) + E_2 \cos\big(\omega_2(t-\tau)\big)) \quad \textbf{Equation 20}$$

A DC bias voltage is applied across the nanojunction, which can be described as a quasi-static local field E_{bias}. The optical field and the bias field interact at the nanojunction, resulting in a change in the polarization P in STO:

$$P = \varepsilon_o(\chi^{(1)}E_{opt} + \chi^{(3)}E_{bias}^2 E_{opt} + \chi^{(3)}E_{opt}^2 E_{bias} + \chi^{(3)}E_{opt}^3) \quad \textbf{Equation 21}$$

where ε_o is vacuum permittivity, $\chi^{(1)}$ and $\chi^{(3)}$ are the linear and third-order nonlinear susceptibility of STO, respectively. The second-order nonlinear response is neglected, for reasons that are described above. This time-varying polarization generates an induced electric field $E_{induced}$, which offsets the photovoltage across the nanojunction. In addition, the induced field can also mix with the bias field, optical field and itself, further modulating the polarization in STO. The resulting photo-induced voltage change $\Delta V_{selected}(\tau)$ at the nanojunction for the selected wavelength pair thus takes the form

$$\Delta V_{selected}(\tau) \sim E_{induced} + \chi^{(1)}E_{induced} + \chi^{(3)}E_{bias}^2E_{induced} + \chi^{(3)}E_{bias}E_{opt}E_{induced} + \chi^{(3)}E_{induced}^2E_{bias} + \chi^{(3)}E_{opt}^2E_{induced} + \chi^{(3)}E_{induced}^2E_{opt} + \chi^{(3)}E_{induced}^3$$

Equation 22

where higher order terms $(\chi^{(3)})^3$ are ignored. Additionally, considering the slow sample response time as compared to the optical frequencies used here, terms containing $\omega_1 t$ or $\omega_2 t$ vanish. Substituting in the forms of E_{bias} and E_{opt} gives

$$\Delta V_{selected}(\tau) \sim \frac{\chi^{(3)} E_{bias}}{64}\Big(4E_1^2\Big[4 + 6\chi^{(3)}E_1^2 + 12\chi^{(3)}E_2^2$$
$$+ 8\chi^{(3)}E_{bias}^2 + \left(\chi^{(1)}\right)^2\left(4 + 9\chi^{(3)}E_1^2 + 18\chi^{(3)}E_2^2\right)$$
$$+ 4\chi^{(1)}\left(2 + 3\chi^{(3)}E_1^2 + 6\chi^{(3)}E_2^2\right.$$
$$\left. + 2\chi^{(3)}E_{bias}^2\right)\Big]\cos(\omega_1\tau)$$
$$+ 4E_2^2\Big[4 + 6\chi^{(3)}E_2^2 + 12\chi^{(3)}E_1^2 + 8\chi^{(3)}E_{bias}^2$$
$$+ \left(\chi^{(1)}\right)^2\left(4 + 9\chi^{(3)}E_2^2 + 18\chi^{(3)}E_1^2\right)$$
$$+ 4\chi^{(1)}\left(2 + 3\chi^{(3)}E_2^2 + 6\chi^{(3)}E_1^2\right.$$
$$\left. + 2\chi^{(3)}E_{bias}^2\right)\Big]\cos(\omega_2\tau)$$
$$+ 3\left[2 + 4\chi^{(1)} + 3\left(\chi^{(1)}\right)^2\right]\chi^{(3)}[E_1^4\cos(2\omega_1\tau)$$
$$+ E_2^4\cos(2\omega_2\tau)]$$
$$+ 12E_1^2E_2^2\Big[2 + 4\chi^{(1)}$$
$$+ 3\left(\chi^{(1)}\right)^2\Big]\chi^{(3)}(\cos[(\omega_1 - \omega_2)\tau]$$
$$+ \cos[(\omega_1 + \omega_2)\tau])\Big). \qquad \textbf{Equation 23}$$

The small non-vanishing fundamental pulse background after the pulse shaper also contributes to the measured photo-induced voltage change. We approximate the input pulse shape as a Gaussian:

$$E_{input}^{Pulse}(t) = E_0 e^{-\left(t/t_p\right)^2}\cos(\omega_c t) \qquad \textbf{Equation 24}$$

where t_p is the pulse width, E_0 is the amplitude and ω_c is the central angular frequency of the pulse wave. Similarly, the focused pulse optical field at the nanojunction is given by

$$E_{opt}^{pulse} = \frac{E_0}{2}\left(e^{-\left(\frac{t}{t_p}\right)^2}\cos(\omega_c t) + e^{-\left(\frac{t-\tau}{t_p}\right)^2}\cos[\omega_c(t-\tau)]\right). \quad \textbf{Equation 25}$$

Since the material response time is much longer than the pulse duration, an integral of t from $-\infty$ to ∞ is needed to derive the pulse-induced photovoltage change $\Delta V_{pulse}(\tau)$ across the nanojunction:

$$\begin{aligned}\Delta V_{pulse}(\tau) \sim \int_{-\infty}^{\infty} \Big(& E_{induced} + \chi^{(1)} E_{induced} + \chi^{(3)} E_{bias}^2 E_{induced} \\ & + \chi^{(3)} E_{bias} E_{opt}^{pulse} E_{induced} + \chi^{(3)} E_{bias} E_{induced}^2 \\ & + \chi^{(3)} \left(E_{opt}^{pulse}\right)^2 E_{induced} + \chi^{(3)} E_{opt}^{pulse} E_{induced}^2 \\ & + \chi^{(3)} E_{induced}^3 \Big)\, dt\end{aligned} \quad \textbf{Equation 26}$$

again ignoring $\left(\chi^{(3)}\right)^3$ and higher order terms. Terms containing $e^{-(\omega_c t_p)^2}$ can also be ignored owing to their extreme small values ($-\left(\omega_c t_p\right)^2 \cong -590$). The computed $\Delta V_{pulse}(\tau)$ then reads

$$\begin{aligned}\Delta V_{pulse}(\tau) \sim \frac{\chi^{(3)} E_0^2 E_{bias}}{128} t_p \sqrt{\pi} \Bigg(\Bigg(& 12E_0^2\left[2 + \chi^{(1)}\left(4 + 3\chi^{(1)}\right)\right]\chi^{(3)} e^{-\frac{3}{4}\left(\frac{\tau}{t_p}\right)^2} \\ & + 16\sqrt{2}\left(1 + \chi^{(1)}\right)\left(1 + \chi^{(1)}\right. \\ & \left. + 2\chi^{(3)} E_{bias}^2\right) e^{-\frac{1}{2}\left(\frac{\tau}{t_p}\right)^2} \Bigg) \cos(\omega_c \tau) \\ & + 3E_0^2\left[2 + \chi^{(1)}\left(4 + 3\chi^{(1)}\right)\right]\chi^{(3)} e^{-\left(\frac{\tau}{t_p}\right)^2}\left[2 + \cos(2\omega_c \tau)\right] \Bigg).\end{aligned} \quad \textbf{Equation 27}$$

The measured photo-induced voltage $\Delta V(\tau)$ across the LAO/STO nanojunction is the sum of both $\Delta V_{selected}(\tau)$ and $\Delta V_{pulse}(\tau)$:

$$\Delta V(\tau) = \Delta V_{selected}(\tau) + \Delta V_{pulse}(\tau) \qquad \textbf{Equation 28}$$

For simplicity, we further assume $E_2 \cong E_1$, and rewrite Equation 28 as

$$\begin{aligned}\Delta V(\tau) \sim a\Bigg(& [\cos(\omega_1\tau) + \cos(\omega_2\tau)] \\ & + b[\cos(2\omega_1\tau) + \cos(2\omega_2\tau) \\ & + 4(\cos[(\omega_1 - \omega_2)\tau] + \cos[(\omega_1 + \omega_2)\tau])] + [ce^{-\frac{1}{2}\left(\frac{\tau}{t_p}\right)^2} \\ & + 4\,d\,e^{-\frac{3}{4}\left(\frac{\tau}{t_p}\right)^2}]\cos(\omega_c\tau) + de^{-\left(\frac{\tau}{t_p}\right)^2}[2 + \cos(2\omega_c\tau)]\Bigg)\end{aligned} \qquad \textbf{Equation 29}$$

using the following abbreviations:

$$\begin{aligned} a &= \frac{1}{16}[4 + 18\chi^{(3)}E_1^2 + 8\chi^{(3)}E_{bias}^2 + \left(\chi^{(1)}\right)^2\left(4 + 27\chi^{(3)}E_1^2\right) + 4\chi^{(1)}(2 \\ &\quad + 9\chi^{(3)}E_1^2 + 2\chi^{(3)}E_{bias}^2)]\chi^{(3)}E_1^2E_{bias} \\ b &= \frac{3}{64a}\left[2 + \chi^{(1)}\left(4 + 3\chi^{(1)}\right)\right]\left(\chi^{(3)}\right)^2E_1^4E_{bias} \\ c &= \frac{1}{8a}t_p\sqrt{2\pi}\left(1 + \chi^{(1)}\right)\left(1 + \chi^{(1)} + 2\chi^{(3)}E_{bias}^2\right)\chi^{(3)}E_0^2E_{bias} \\ d &= \frac{3}{128a}t_p\sqrt{\pi}\left[2 + \chi^{(1)}\left(4 + 3\chi^{(1)}\right)\right]\left(\chi^{(3)}\right)^2E_0^4E_{bias.}\end{aligned} \qquad \textbf{Equation 30}$$

A nonlinear least-squares fit is performed to obtain the initial fitting parameters. The initial values for *a-d* and their corresponding standard errors are listed in the table below. A slight fine-tuning of *a-d* is then performed manually around the initial values to better reproduce the experimental data, and final values used for the simulation in the next section are:

Table 1: Fitting Parameters

	Estimate	Standard Error
a	-0.0000425596	3.46618×10^{-8}
b	0.0128076	0.000221672
c	0.887046	0.0123936
d	0.147767	0.00276426

Table 2: Final Fitting Values Used

	A	*b*	*c*	*d*
Coefficient	4.33×10^{-5}	0.018	1.1	0.154

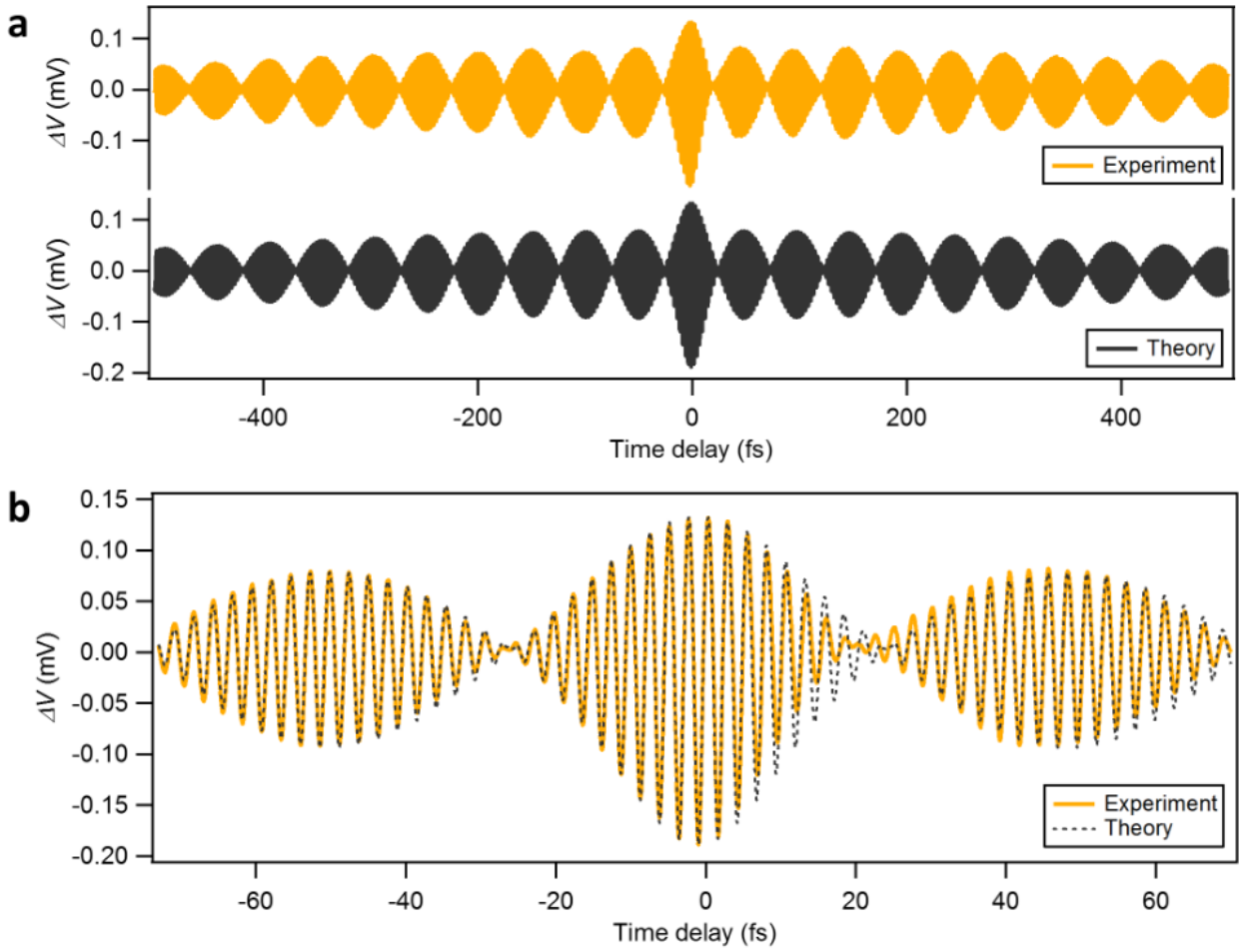

Figure 37: Comparison of Simulation and Experimental Results. (a) Comparison of experimental snd simulated time domain signals for a 20 THz frequency and (b) a zoomed in overlapped plot, showing close agreement.

3.2.3 Simulation and Experimental Results

The time-varying optical field E_{opt} from ultrafast pulses and the quasi-static bias field E_{SD} from the DC bias voltage interact at the LAO/STO nanojunction, resulting in a change in the polarization in STO. Frequency components ω_1 and ω_2 in the optical fields mix, and the resulting time-varying polarization produces an induced field, which offsets the applied DC electric field,

as well as further mix with the bias field, the optical field and even with itself to produce a photo-induced voltage change at the difference frequency $\omega_1 - \omega_2$ at the LAO/STO nanojunction. To better understand the different contributing components for the THz generation, a numerical simulation of the measured time-domain signal has been performed using Equation 29 and the result is shown in Figure 37.

The first term represents the linear response of the two selected frequencies at the LAO/STO nanojunction. The second term corresponds to the frequency mixing through the third order nonlinear effect. The third and fourth terms are the induced linear and third-order nonlinear photoconductive response by the pulse at the nanojunction, respectively. These two terms exist because of the small non-vanishing fundamental pulse background (baseline of the blue curve in Figure 34(b). In Figure 37, we compare the measured time-domain signal at a difference frequency of 20 THz with the numerical simulation. Both the beating envelope and the asymmetry in the upper and lower amplitude of the envelope are reproduced. The overall decay of the signal amplitude is due to the finite width of the two selected fundamental wavelengths. Figure 37(b) shows a close-up of the measured signal and simulated response near $\tau = 0$, showing good agreement between the two. The unequal amplitudes of the lower and upper envelope are a result of the nonlinear process that produces the THz response. The fast oscillation with beating envelope mostly comes from the superposition of the two fundamental frequencies. Discrepancies between the measured signal and the simulation are most visible at the node (near $\tau = 20$ fs), and are attributed to imperfect alignment of the two beams during the movement of the optical time delay line. In addition to the main non-resonant three wave mixing process, other responses could also take place. For example, the mid-gap states, which are known to form in STO, could introduce near-resonant structure to the response. Nonetheless, the good agreement between the simulation

and the experimental data indicates that these responses are unlikely to play a dominant role. The linear dependence of signal amplitude on the bias voltage (as indicated by the theoretical model) has also been confirmed experimentally.

3.2.4 Discussion

Compared to other existing ultra-broad bandwidth THz sources, such as free-electron lasers, or nonlinear crystals such as GaSe crystals, the LAO/STO nanojunctions are easy to fabricate and reconfigurable, and do not rely on phase matching due to the extremely small dimension of the device. Here, the bandwidth of the THz emission is not restricted by the material, but rather limited only by the spectral bandwidth of the ultrafast pulses. Moreover, a high spatial resolution comes naturally with the LAO/STO nanojunctions. By simply drop-casting the target nanoscale objects onto LAO/STO surface, and creating a nanojunction in the vicinity of a single particle or molecule, individual nanoscale objects can be addressed independently, offering insights that would otherwise be inaccessible from averaging over the ensemble. Spatial mapping of arbitrary substrates is also possible by scanning an LAO/STO nanojunction device in close proximity to the sample (or the other way around). Variations on the sample surface lead to modifications in the interaction among different fields at the nanojunction, which can be reflected by the measured photo-induced voltage change, with a spatial resolution determined by the nanojunction size. In this work, we only control the amplitude of the input ultrafast pulse. Full use of the dual-mask SLM, which can achieve both amplitude and phase modulation, can enable arbitrary shape of the THz waveform for future applications.

In this chapter, we have demonstrated over 100 THz bandwidth selective difference frequency generation at LAO/STO nanojunctions that spans the entire far-infrared to mid-infrared regime by femtosecond optical pulse shaping. The broadband nonlinearity also gives rise to a similar sum-frequency generated response. The ultra-broad tunability, combined with an exceptional spatial precision of 10 nm, shows great promise for exploring fundamental physics in single nanoscale objects such as quantum dots, nanoparticles or individual molecules. The low optical excitation power imposes minimal heating or other adverse effect on the analyte. The LAO/STO nanojunction serves both as generator and detector of THz emission; by writing two similar nanojunctions adjacent to each other, one can generate and detect tunable, ultra-broad bandwidth THz fields at the micron scale. On the other hand, numerous nanoelectronic devices have already been realized at the LAO/STO interface, such as photodetectors and field-effect transistors. Combining the versatility of the LAO/STO nanodevices with tunable THz functionality further enables a new pathway towards integrated on-chip optoelectronic devices.

4.0 VIS-NIR Extinction and Enhanced Optical Nonlinearities in Graphene/LAO/STO Nanostructures

The content in this section is the subject of a publication in Nano Letters[67].

4.1 Introduction

Graphene exhibits many unique properties that are desirable for quantum and optical device applications[68-70]. The optical attenuation from a single undoped graphene monolayer is $\pi\alpha \approx 2.3\%$, where α is the fine structure constant, and is essentially constant throughout the visible to near-infrared (VIS-NIR) spectral range[71]. The graphene chemical potential μ, which can be tuned via electrostatic gating or chemical doping, has only a modest effect on optical absorption[72,73]. While these optical properties of graphene may be beneficial for some applications (e.g, transparent ultrathin conductors[74]), they preclude others that require much stronger coupling, such as photodetectors[75] or optical modulators. For light in the mid-infrared to far-infrared region, graphene hosts a strong response attributed to plasmonic excitations[76-79]. However, it has proven difficult to extend this response to VIS-NIR frequencies[80]. The graphene/VIS-NIR interaction has been enhanced through a variety of strategies: by creating graphene-based metamaterials or surfaces in which the charge-neutrality point (CNP) is modulated at the nanoscale[81,82], by creating arrays of graphene nanodisks or nanoribbons[77-79,83], or by placing graphene near metallic plasmonic metasurfaces or nanoscale metal gratings[84-87].

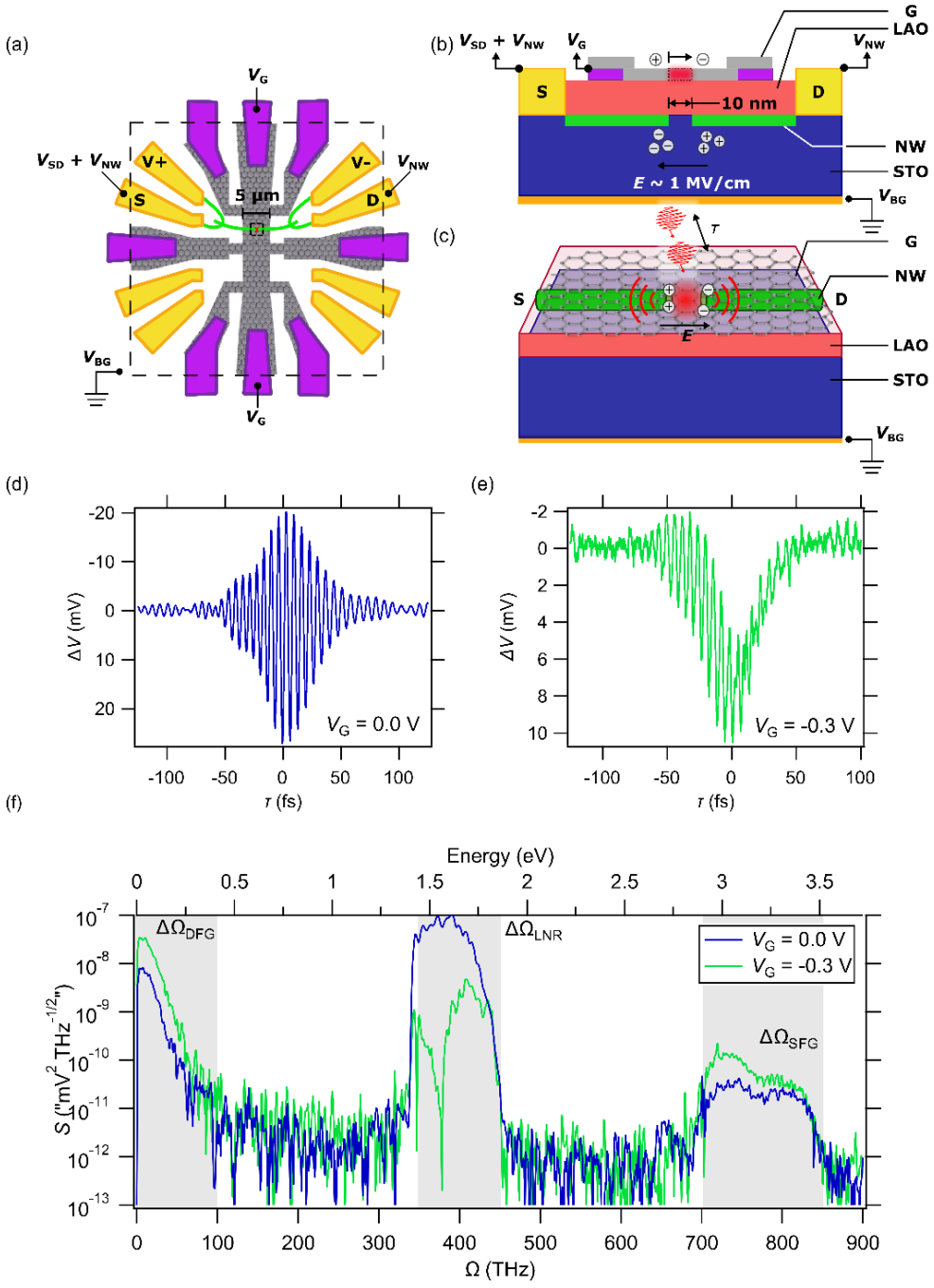

Figure 38: VIS-NIR Extinction in Graphene. . (a) Top-view of G/LAO/STO heterostructure. Purple electrodes indicate connections to the graphene. Pink electrodes contact the LAO/STO interface. A nanojunction device is sketched across the top half of the 5-µm-wide Hall bar. (b) Zoomed-in side view and (c) perspective of the biased LAO/STO nanojunction underneath the graphene. Images not to scale. The green wire represents the

conducting nanostructure at the LAO/STO interface. The black dashed rectangle symbolizes the graphene nanoribbon-like structure. A dipole is pictured above the graphene to illustrate the dipole field established in the nanodisk-like structure. (d,e) Representative time domain photovoltage measurements on Device A, where $\Delta V = V_+ - V_-$, at $V_G = 0.0$ V (d) and $V_G = -0.3$ V (e). $V_{NW} = 0.0$ V and $V_{SD} = -1.0$ V for both measurements. (f) Power spectra of the time domain signals in (d,e).

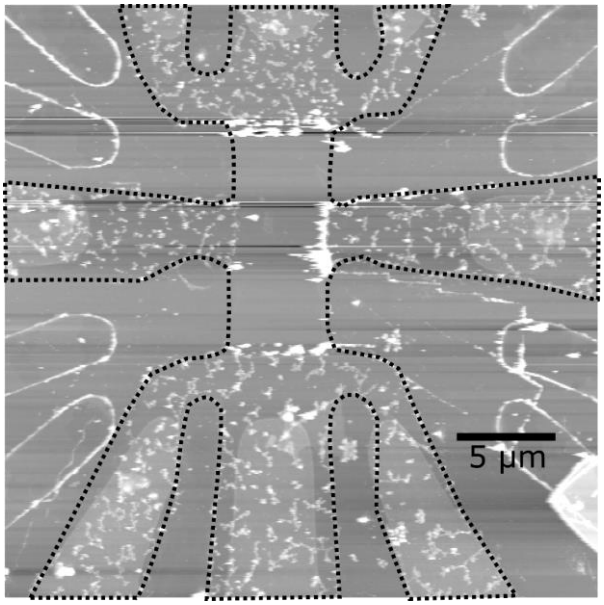

Figure 39: AFM Image of graphene/LAO/STO canvas. . The graphene Hall bar is outlined in black.

Recently, as discussed in Section 2.1.5.1, graphene has been integrated with $LaAlO_3/SrTiO_3$ (LAO/STO) nanostructures[21,88-90], which themselves have a variety of interesting optical and electronic properties[1]. To review, when the LAO thickness is close to the critical thickness for a metal-insulator transition, ~3-4 unit cells[25], the conductivity of the LAO/STO interface can be reversibly switched at nanoscale dimensions using conductive atomic force microscope (c-AFM) lithography[28,29,81]. A wide range of LAO/STO-based optoelectronic devices have been "sketched" in this fashion, including 10 nm-scale photodetectors[91] and nanoscale terahertz (THz) sources and detectors[33,92] with >100 THz bandwidth.

We describe the ultrafast optical response of graphene subjected to large local electric fields from a nearby nanowire junction created in the LAO/STO layer (Figure 38 (a-c)). The nanojunction consists of a conducting LAO/STO nanowire with a nanoscale (~10 nm) insulating gap. The optical response of the graphene is measured by the same junction, which behaves as a broadband near-field photodetector[33,92,93]. Details of c-AFM lithography, sample growth, and graphene patterning can be found in Chapter 2.0.

The optical response of G/LAO/STO nanostructures is measured as a function of local electrostatic LAO/STO nanowire-gates ($V_{\mathrm{NW}}, V_{\mathrm{SD}}$) and a global gate ($V_{\mathrm{G}}$) defined by the graphene, as illustrated in Figure 38(a). The nanostructure is illuminated by ultrafast pulses and the induced photovoltage across the LAO/STO nanojunction $\Delta V(\tau) = V_{+}(\tau) - V_{-}(\tau)$ is measured as a function of the time delay τ between two pulses[33,92] (Figure 38 (d,e)). The power spectrum $S(\Omega)$ versus frequency Ω (Figure 38 (f)) is calculated by taking a Fourier transform of the photoresponse $\Delta V(\tau)$ with respect to τ. A detailed description of the experiment setup, is provided in Section 2.3.

4.2 Experimental Results

LAO/STO nanojunctions without graphene have been shown to locally generate and detect THz emission, with greater than 100 THz bandwidth, via the third-order nonlinear optical process in STO[13]. V_{SD} creates a quasi-static electric field $\vec{E}_{\mathrm{SD}}$ across the junction that is highly confined in space to ~10 nm, while input optical fields $\vec{E}_{opt}(\omega_1), \vec{E}_{opt}(\omega_2)$ are sharply peaked in the time domain. The three electric fields mix to generate the nonlinear response of the nanojunction at the difference $(\omega_1 - \omega_2)$ and sum $(\omega_1 + \omega_2)$ frequencies. Equivalently, the third-order nonlinear

susceptibility of the STO is converted, via E_{SD}, into a local second order nonlinear susceptibility at the site of the nanojunction[92]. The corresponding power spectrum has several distinct ranges:

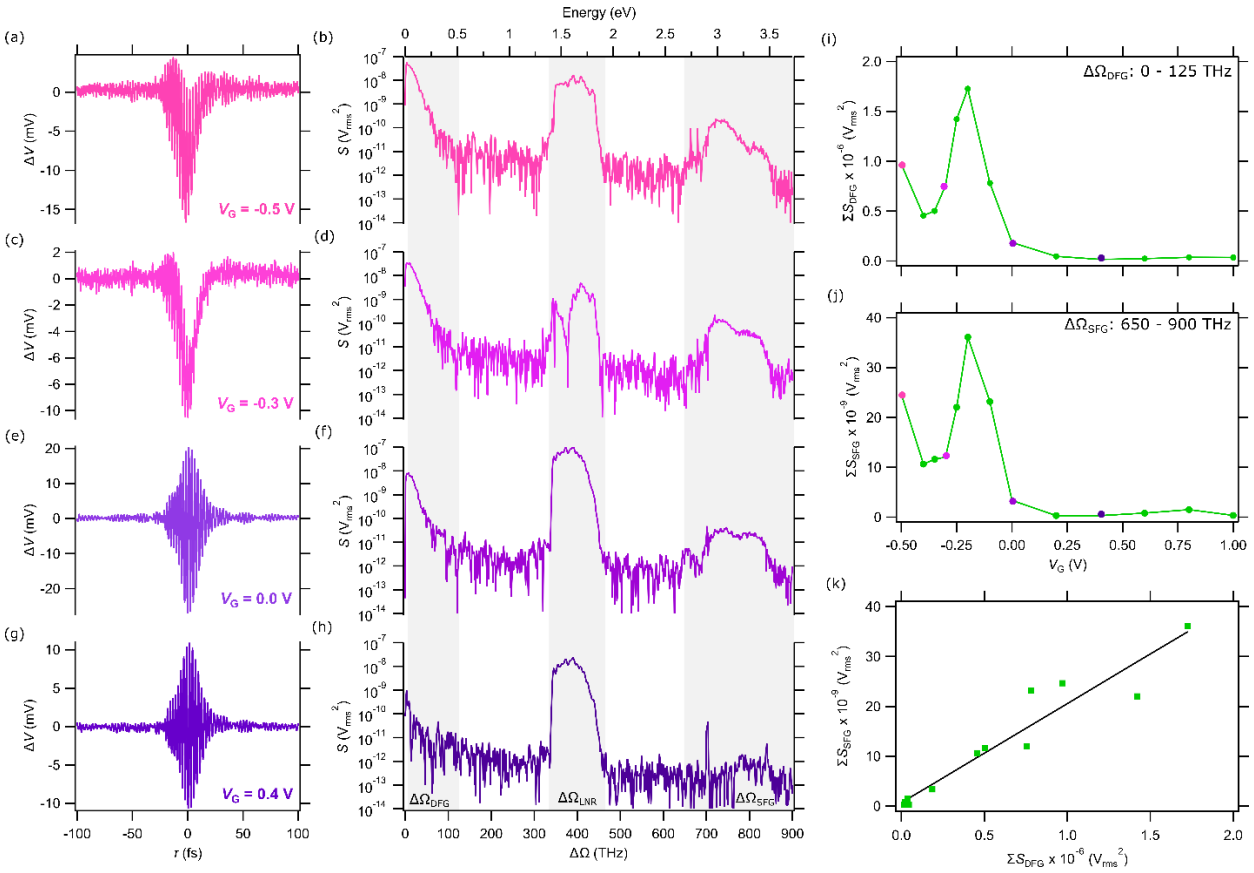

Figure 40: Gate-Dependence of Graphene/LAO/STO Optical Response. (a,c,e,g) V_G dependence of the G/LAO/STO time domain signal. A gate-dependent splitting of the time domain signal appears at $V_G = -0.3$ V. ($T = 10$ K, $V_{SD} = -1$ V, $V_{NW} = 0$ V.) (b,d,f,h) Power spectra of the time domain signals. All plots share the same color correspondences. (i,j) Integrals of the DFG and SFG components of the power spectra vs. V_G, respectively. (k) Plot of the integrated DFG and SFG integral values (squares) with a linear fit.

the difference-frequency generated response ("DFG") $\Delta\Omega_{DFG}$: 0 to 125 THz, the sum-frequency generated response ("SFG") $\Delta\Omega_{SFG}$: 650 to 900 THz, and the response at the fundamental excitation, which exists primarily in the near-infrared but extends into the visible range 325 to 450

THz (1.4-1.9 eV). This constitutes the linear response ("LNR") of the junction to the input laser excitation ($\Delta\Omega_{\mathrm{LNR}}$).

The strong electric field across the nanojunction induces a local dipole moment in the graphene, locally breaking symmetry and causing a second-order nonlinear optical response, as depicted in Figure 38 (b,c). This symmetry breaking greatly enhances the difference and sum frequency responses of the Graphene/LAO/STO nanostructure as compared to a bare LAO/STO nanojunction, and will be discussed in more detail later on.

4.2.1.1 **Gate-dependence of optical response**

Time-domain photovoltage measurements of Graphene/LAO/STO nanojunctions are taken under a variety of experimental conditions at temperatures ranging from $T = 5 - 50$ K. There are three electrical gates that are tuned: V_{G}, the "global" bias with respect to the STO back gate, the nanowire gate V_{NW}, the common mode bias applied to the nanowire, and V_{SD}, the differential bias across the junction. For all experiments, the back gate V_{BG} is grounded. Other degrees of freedom explored include the average optical power and linear polarization. Here we focus mainly on the gate-dependent measurements, and show some examples of the dependence of the Graphene/LAO/STO nanostructure response on optical parameters. The photovoltage $\Delta V(\tau)$ is measured at different gate values, while the four-terminal resistance of the graphene $R_{\mathrm{G,4T}}$ is measured at the same conditions. Extinction features have been observed in 12 devices on three different samples. We focus here on results from four devices, **Devices A**, **B, C, D**.

The graphene chemical potential is first tuned by applying a DC offset to the global graphene gate V_{G} with respect to ground. The results of a V_{G}-dependent experiment on **Device A** are summarized in

Figure 40. Figure 38(d) shows the time domain measurement at $V_{\mathrm{G}} = 0.0\ \mathrm{V}$, which resembles the response from a LAO/STO nanojunction without graphene. When $V_{\mathrm{G}} = -0.3\ \mathrm{V}$, shown in Figure 43(e), the time-domain signal changes significantly. In the corresponding power spectrum (Figure 43(f)), a sharp, ~99.96% extinction feature is revealed within the LNR spectral region at Ω =378 THz (1.56 eV), compared to the response at to the $V_{\mathrm{G}} = 0.0\ \mathrm{V}$. Experiments performed on control nanojunctions in the absence of graphene do not exhibit these extinction features (see below.)

When the graphene chemical potential is tuned via V_{G}, the response of the G/LAO/STO nanojunction changes considerably (Figure 40). This method of changing the chemical potential does not reveal a clear resistance maximum that can be ascribed to the graphene CNP. By contrast, gating with V_{NW} reveals a well-defined CNP, as will be described below. V_{NW} can tune the graphene chemical potential more effectively than V_{G}, perhaps because V_{G} is comprised of a DC offset applied to metal top-electrodes at either end of the graphene main channel, whereas the local nanowire gate V_{NW} is comprised of a DC offset applied directly to the conducting nanowire within the LAO/STO interface. To summarize, we have access to multiple controls to tune the carrier density in the graphene: the strong zero-dimensional variations at the site of the junction, the one-dimensional variations of V_{NW}, and the two-dimensional variations of V_{G}.

Four representative time-domain photovoltage traces from **Device A** for different V_{G} values, and their corresponding power spectra, are shown in Figure 40. Here $V_{\mathrm{NW}} = V_{\mathrm{BG}} = 0$ and $V_{\mathrm{SD}} = -1\ \mathrm{V}$ at $T = 10\ \mathrm{K}$. A sharp extinction feature occurs over a narrow gate range, $V_{\mathrm{G}} = -0.5\ \mathrm{V}$ to $-0.2\ \mathrm{V}$, and can be observed in the time-domain signals in Figure 40(a,c). Additionally, the nonlinear (DFG, SFG) regions of the power spectra for these time domain signals is quite large.

In comparison, the nonlinear regions of the power spectra in Figure 40(f,h), where no extinction is observed, have lower amplitudes.

To further examine the enhancement of the nonlinear response, the integrated power spectrum vs. V_{G} is plotted for the DFG and SFG regions in Figure 40 (i,k), and compared in Figure 40(l). The nonlinear response of the G/LAO/STO nanostructure is maximal at $V_{\mathrm{G}} = -0.2$ V, close to $V_{\mathrm{G}} = -0.3$ V, where the sharp extinction line in the LNR range appears. It is important to note that the values of both the DFG and SFG integrals are an order of magnitude larger in the vicinity of the extinction feature than elsewhere. The corresponding LNR power spectra integral vs. V_{G} is anticorrelated with these features (Figure 41 (c)).

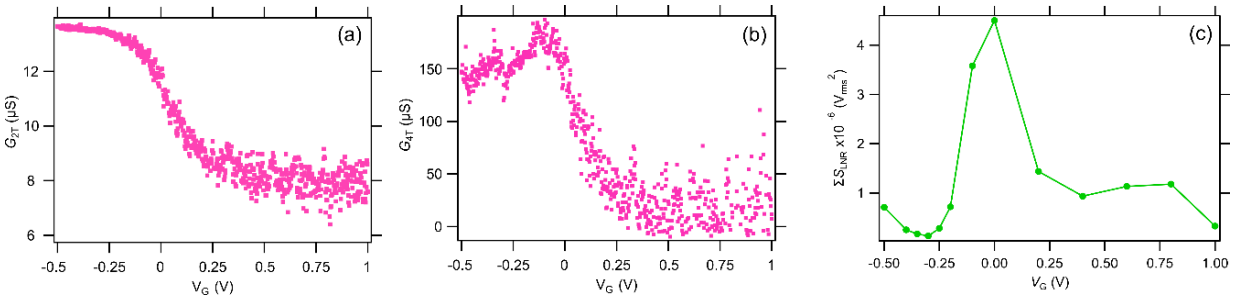

Figure 41: Graphene conductance and LNR integral vs. V_G.

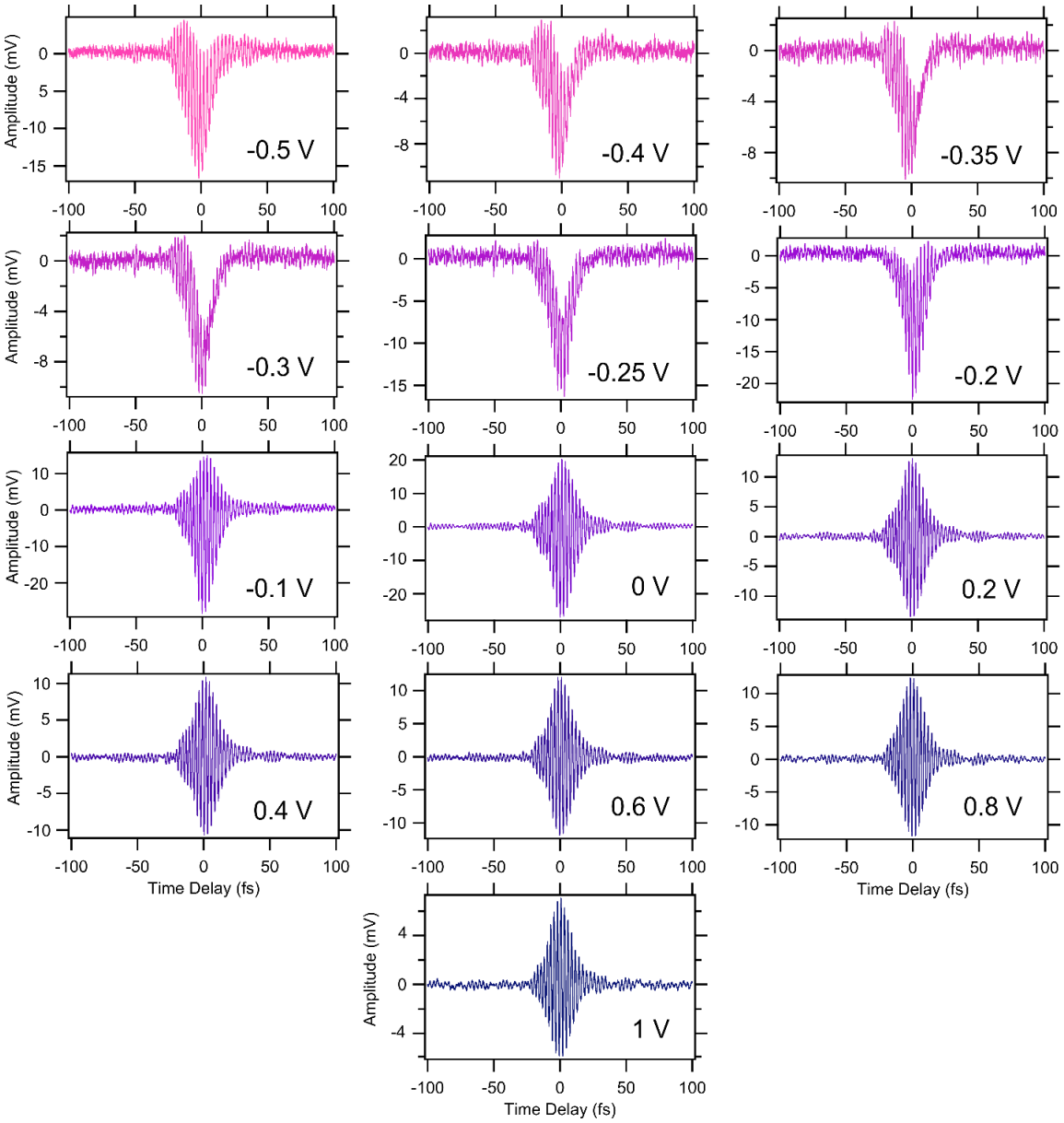

Figure 42: Complete data set from Figure 40.

4.2.1.2 **Dependence on nanowire gate**

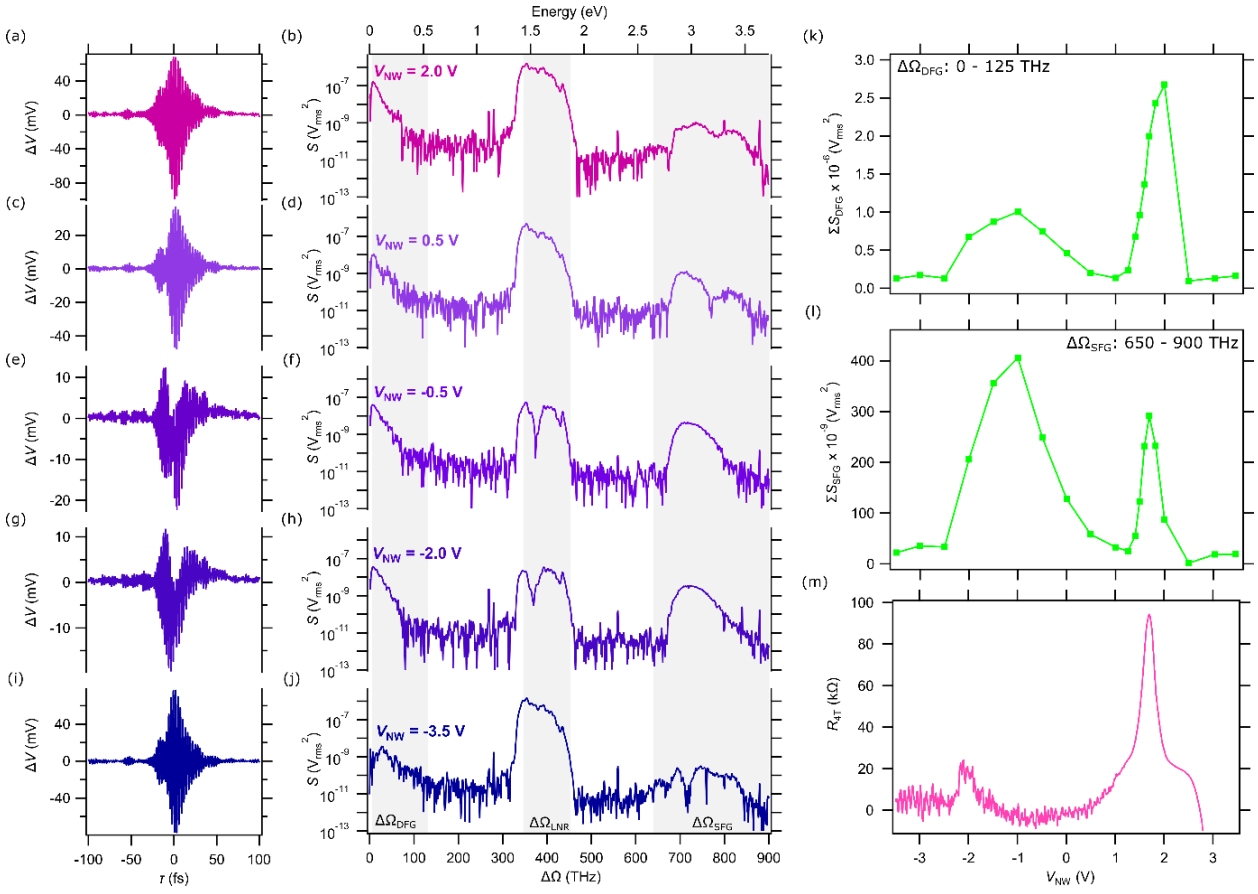

Figure 43: Nanowire Gate Dependence of Optical Response. (a,c,e,g,i) Time domain signals at different V_{NW} values. (b,d,f,h,j) Power spectra of the time domain signals. (k,l) Integrals of the DFG and SFG responses as a function of V_{NW}, respectively. (m) Four-terminal graphene resistance $R_{G,4T}$ measured as a function of V_{NW}.

The nonlinear response and extinction features depend sensitively on the common-mode nanowire gate bias V_{NW}. Five representative time domain signals and power spectra for different V_{NW} values from **Device B** are shown in Figure 43, with $V_{SD} = -2$ V and $V_G = V_{BG} = 0$ V at $T =$ 45 K. A sharp extinction line appears in the LNR region at Ω = 375 THz when V_{NW} = -1.5 V. Remarkably, an extinction line also appears in the SFG response at Ω = 760 THz when V_{NW} = 1 V. The graphene four-terminal resistance $R_{G,4T}$ is plotted as a function of V_{NW} in Figure 43 (n), where the CNP is clearly visible at V_{NW} = 1.7 V with a second local maximum in $R_{G,4T}$ at V_{NW} =

-2 V. The second local maximum may be a signature of inhomogeneous doping in the graphene by the nanojunction, as discussed in more detail below. It is instructive to compare the integrated power spectra over the DFG, LNR and SFG ranges with the measured four-terminal graphene resistance $R_{G,4T}$. Extinction features that appear in the LNR response are correlated with local maxima in the DFG and SFG integrals which peak near V_{NW} = -1.5 V. Additionally, both nonlinear signals have local maxima near the CNP of graphene (V_{NW} = 1.7 V).

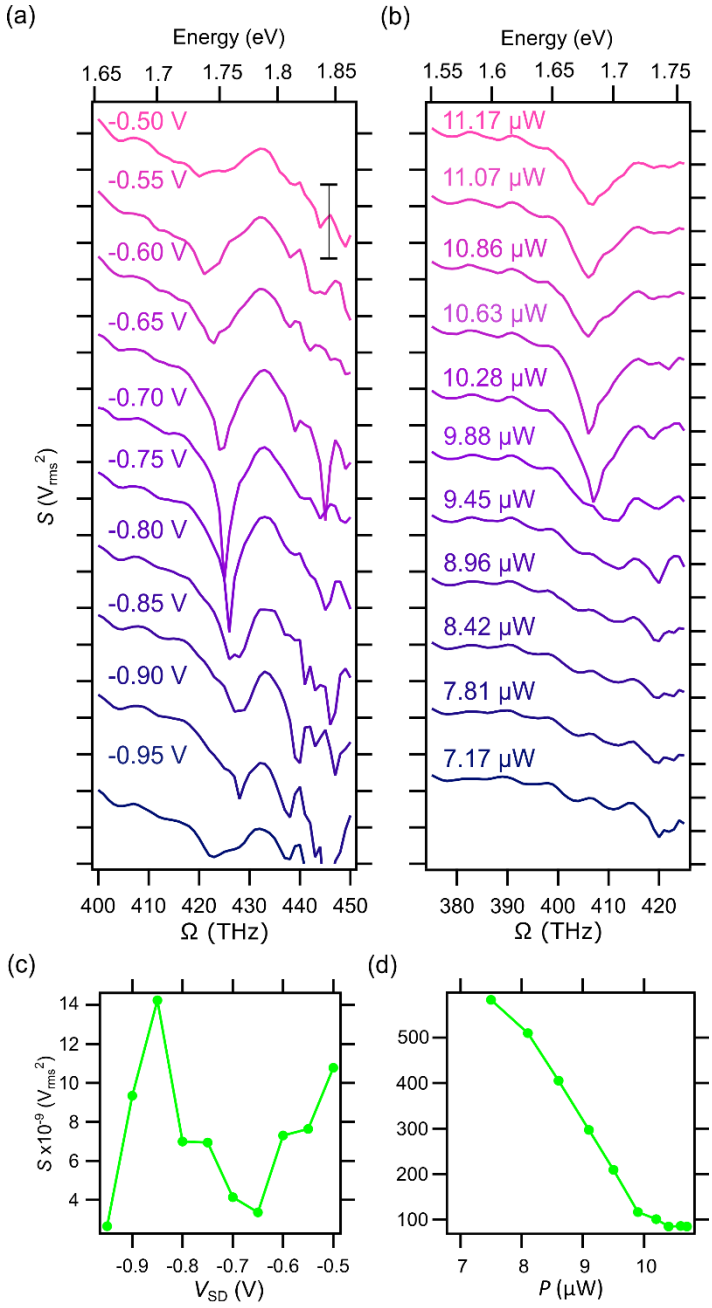

Figure 44: Source-Drain Bias and Power Dependence. Waterfall plots of the Vis–NIR region of (a) bias-dependent and (b) power dependent power spectra, zoomed in to the vicinity of an extinction feature. Each tick mark denotes two orders of magnitude, and plots are vertically offset for clarity. (c,d) Integrals of Vis-NIR power spectra region reveal trends in the extinction feature evolution.

4.2.1.3 **Source-drain bias and power dependence**

The extinction features also show a sensitive dependence on the magnitude of the gate bias across the junction V_{SD} (Figure 44(a**)**). As V_{SD} increases in magnitude from -0.5 V to -0.95 V, with $V_{\mathrm{G}} = 25$ mV and $V_{\mathrm{NW}} = V_{BG} = 0$ V at $T = 10$ K, a spectrally sharp extinction feature in the LNR response emerges, shifts in frequency, and disappears. Therefore, unlike V_{G} or V_{NW}, V_{SD} can more easily be used as a fine-tuning parameter to precisely control the amplitude and frequency of extinction features. A power dependence experiment (with $V_{\mathrm{SD}} = -1.25$ V, $V_{\mathrm{G}} = 625$ mV and $V_{\mathrm{NW}} = V_{BG} = 0$ V at $T = 10$ K) reveals a tuning of spectral extinction that qualitatively resembles the dependence on V_{SD} (Figure 44(b)).

The interplay between the V_{SD} and optical power dependence of the extinction feature is investigated by constructing a "matrix" of data by repeating the same optical power sweep at different V_{SD} values for **Device E,** with $V_{\mathrm{NW}} = V_{BG} = 0$ V. The input optical power to the G/LAO/STO nanostructure is decreased from $9.42 \rightarrow 7.88$ μW at $V_{\mathrm{SD}} = -0.2$ V, then V_{SD} is increased and the power sweep is repeated.

As the V_{SD} value increases, the observed extinction features shift downwards, or to a lower power. Black arrows in Figure 45 mark the first power spectrum for which two extinction features are visible in the LNR response. The downward shift in the black arrows shows how the power dependence shifts with increasing V_{SD}. Although the V_{SD} and optical power dependences of the extinction feature appear to be similar and interrelated, the complex interplay of various optical and electronic effects on the G/LAO/STO nanostructure prohibit the formulation of a specific scaling law. Though the interplay between optical power and V_{SD} is complex, and we cannot obtain an exact scaling law depicting their relationships, the two parameters appear to act together as

powerful fine-tuning parameters for extinction feature frequencies and extinction ratios, as well as the nonlinear response of the G/LAO/STO nanostructure.

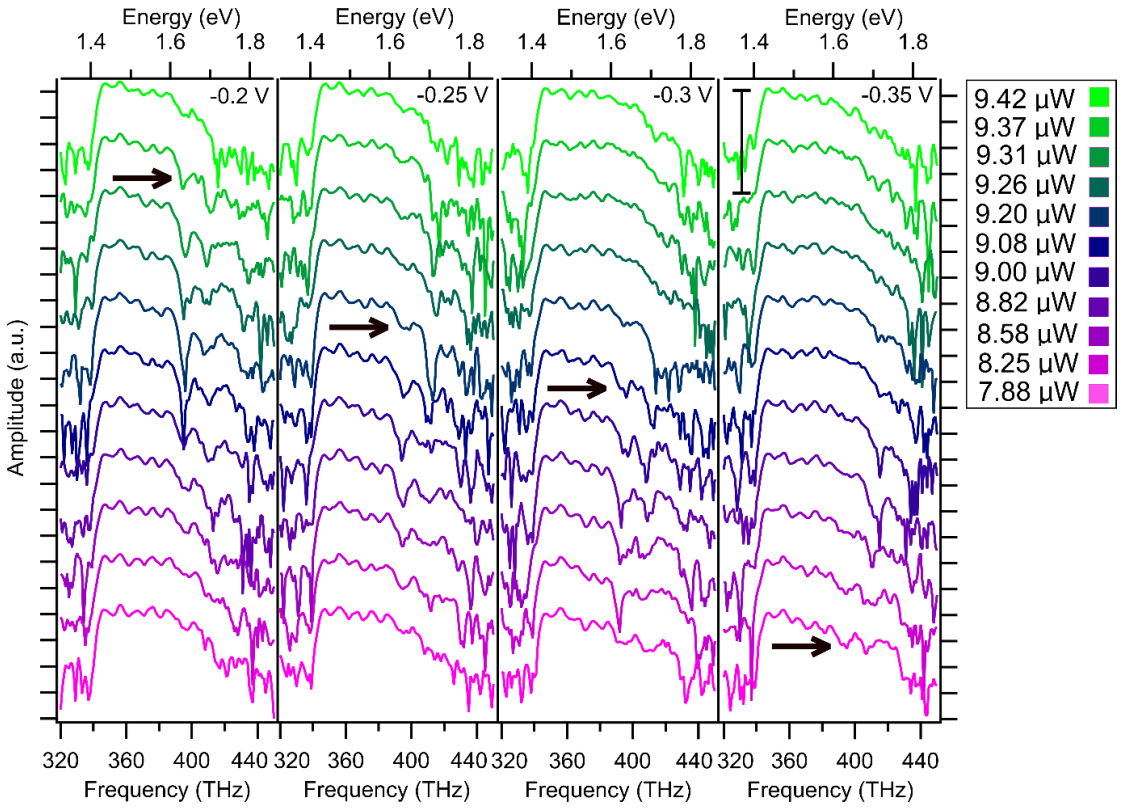

Figure 45: Interplay of power and source-drain bias.

4.2.1.4 **Linear polarization dependence**

To study the polarization dependence of the VIS-NIR sharp absorption line, we place a thermally-stabilized liquid crystal variable retarder optic (LCVR) in the beam path directly before the Michelson interferometer. The LCVR can act as a broadband half waveplate. This allows us to switch the linear polarization of the input pulses from 0 degrees (parallel to the device) to 90 degrees (perpendicular to the device) by changing the voltage applied to the liquid crystal. We can therefore instantaneously switch between two linear polarizations without disturbing the beam path, as we would if we manually rotated a half wave plate.

For each experiment, a measurement is taken at 0 degrees polarization, or parallel to the nanojunction device. The LCVR is then switched to 90 degrees polarization and another measurement is taken. In the two experiments shown on **Device D** in Figure 46, the linear polarization is switched from 0 degrees to 90 degrees, then immediately back to 0 degrees, then 90 degrees again. For both of the experiments shown, the nanostructure appears to have two different resonances; one when the light is polarized along the nanowire, and another when the light is polarized perpendicular to it. For Figure 46 (a), the extinction appears at about 400 THz for parallel polarization and at 428 THz for perpendicular polarization. For Figure 46(b), the extinction appears at 359 THz for parallel polarization and at 368 THz for perpendicular polarization.

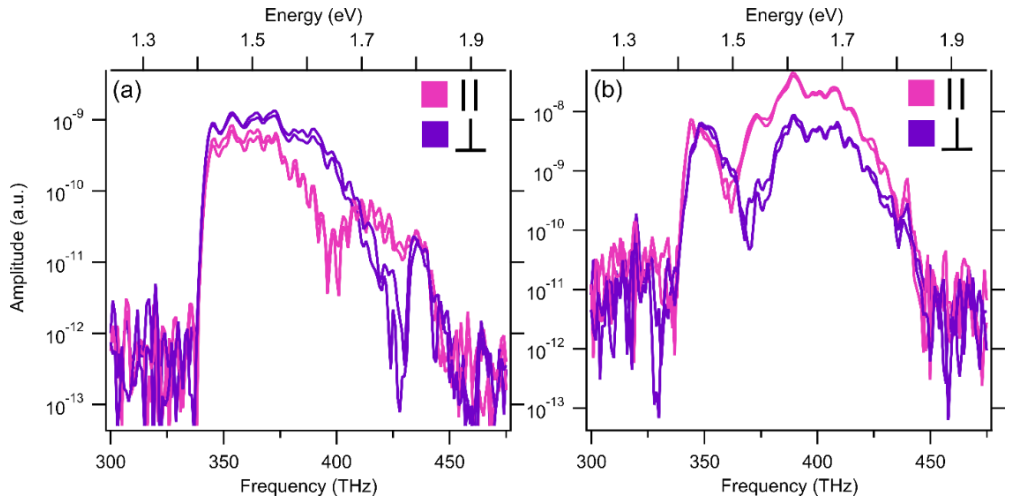

Figure 46: Linear polarization dependence of extinction feature. Pink: light polarized parallel to nanojunction device (parallel to nanowire containing the nanojunction.) Purple: light polarized perpendicular to device. Power spectrum at each polarization for (a) $T = 5\ \mathrm{K}, V_{SD} = -1\ \mathrm{V}, V_G = 1\ \mathrm{V}$ and (b) $T = 10\ \mathrm{K}, V_{SD} = -2.3\ \mathrm{V}, V_G = 2.5\ \mathrm{V}$.

4.2.2 Control Nanojunction data

To verify that the observed sharp extinction features originate from the graphene in the G/LAO/STO nanostructure and not from the LAO/STO, a nanojunction device (**Device N**) was written on a LAO/STO sample without graphene. A nanowire gating experiment is performed. Time domain measurements (Figure 47) are taken at a constant $V_{\mathrm{SD}} = -1$ V while changing V_{NW}. The corresponding power spectra are shown in Figure 48. The device shows no observable nanowire gate dependence. No sharp extinction feature is observed, and there is no noticeable change in the nonlinear DFG or SFG response with V_{NW}.

LAO/STO without graphene clearly has a characteristic nonlinear response that is not gate-dependent. On the other hand, nanowire gating of the G/LAO/STO nanostructure reveals dramatic changes in both the DFG and SFG responses. We therefore assume that the observed nonlinearities in the G/LAO/STO nanostructures are comprised of a combination of both the graphene and LAO/STO nonlinear responses, and the gate dependence originates in the graphene response. Figure 49 shows the integrals of the relevant regions of the power spectra. Note that, unlike the G/LAO/STO nanostructure, the linear and nonlinear responses of LAO/STO nanojunction without graphene do not show any dependence on the nanowire gate value.

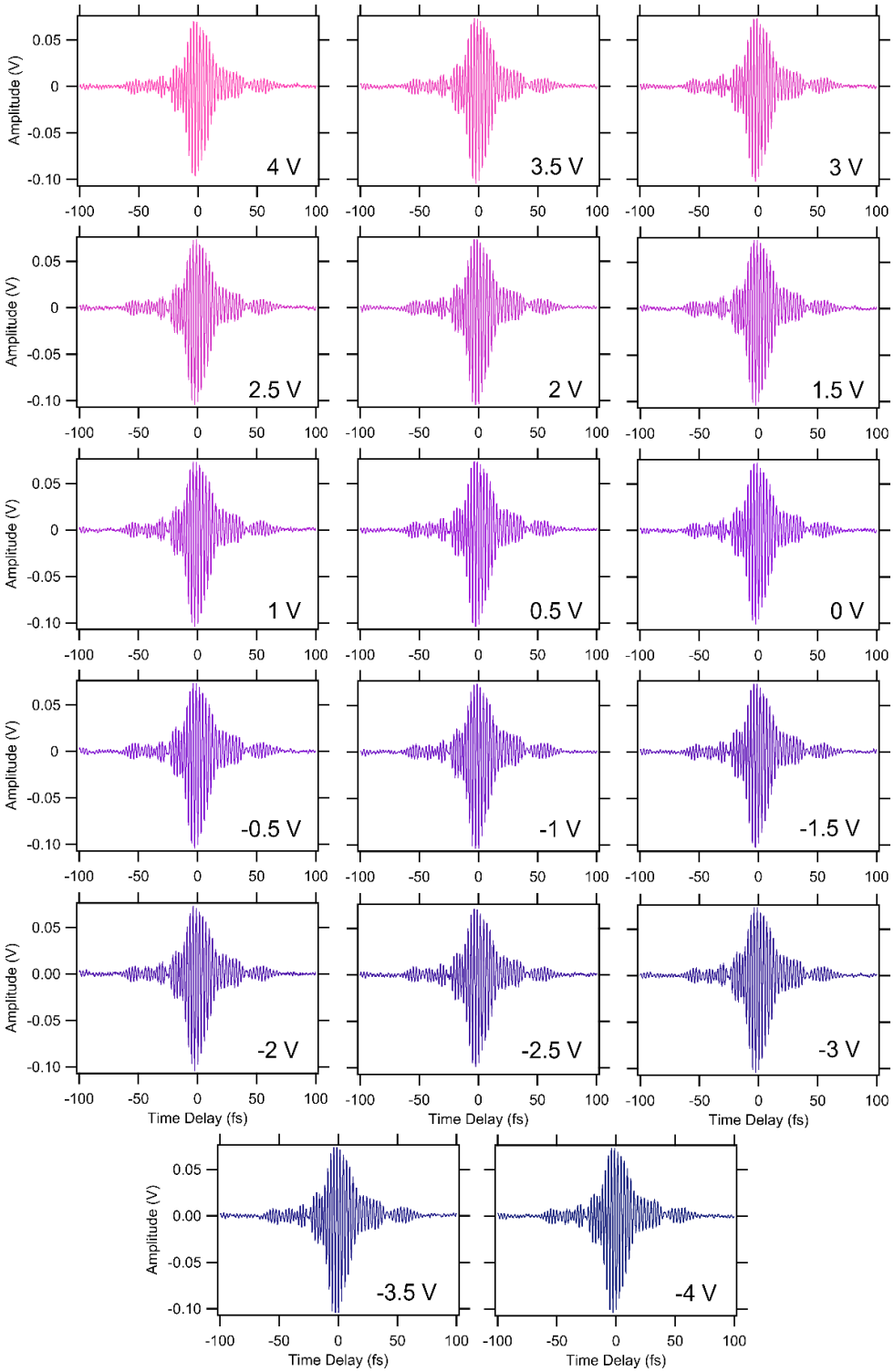

Figure 47: Control nanojunction time-domain signals. The signal at each gate value is nearly identical to the rest; no splitting features appear, and there are no noticeable changes in amplitude.

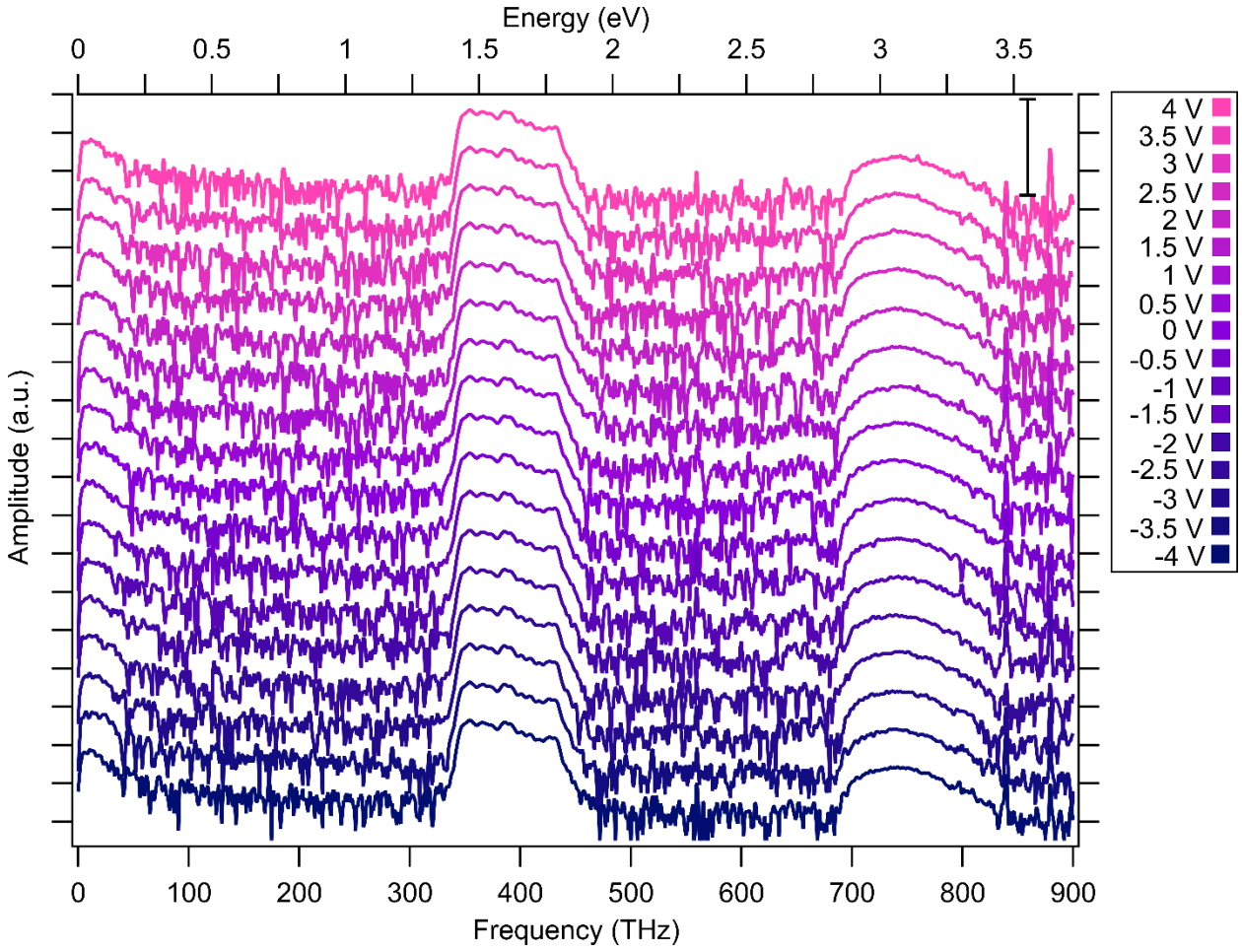

Figure 48: Control nanojunction power spectra. Different power spectra are offset vertically for clarity. Scale bar denotes five orders of magnitude. No nanowire gate dependence or extinction features are observed.

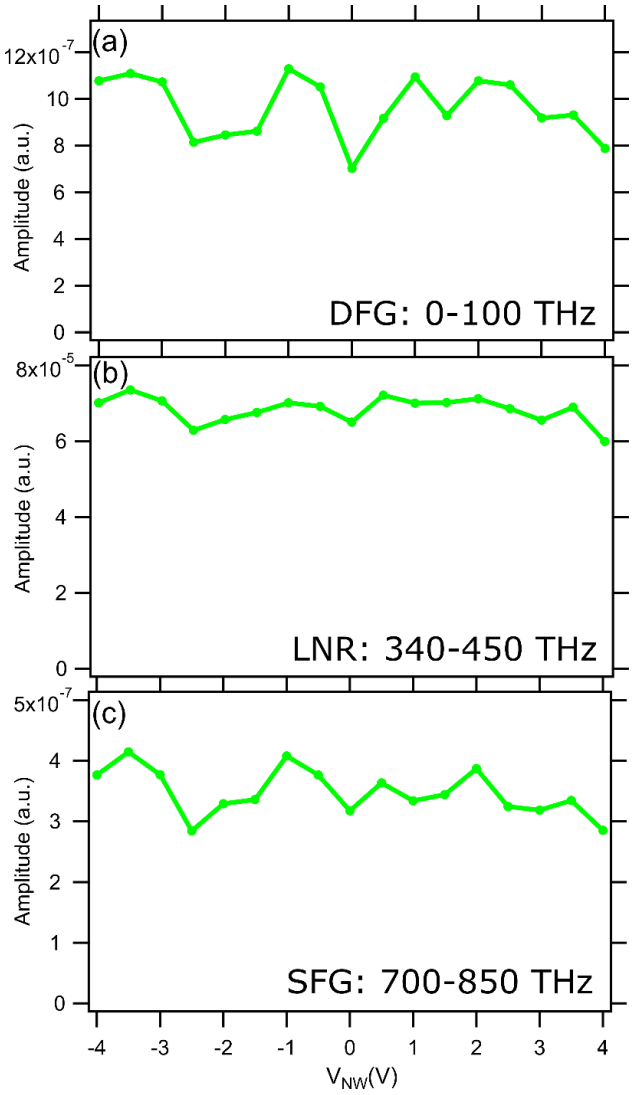

Figure 49: Control nanojunction power spectrum integrals. Integrals versus nanowire gate for (a) DFG (b) LNR, and (c) SFG regions. Notice that the linear and nonlinear responses of the LAO/STO nanojunction without graphene do not show any observable gate dependence.

4.2.2.1 **Graphene Dirac feature splitting**

To learn more about the inhomogeneous gating of the graphene by V_{NW} and V_{SD}, we measured $R_{\mathrm{G,4T}}$ as a function of V_{NW} at different V_{SD} values. If the biased LAO/STO nanojunction is a source of inhomogeneous doping in the graphene sheet, we should expect to see a separation of two Dirac point features as the LAO/STO nanojunction source-drain bias V_{SD} increases in magnitude. As V_{NW} is tuned, different regions of the graphene sheet will be gated to the CNP at different gate values, and the difference in these two gate values should increase as the inhomogeneity of the gating increases.

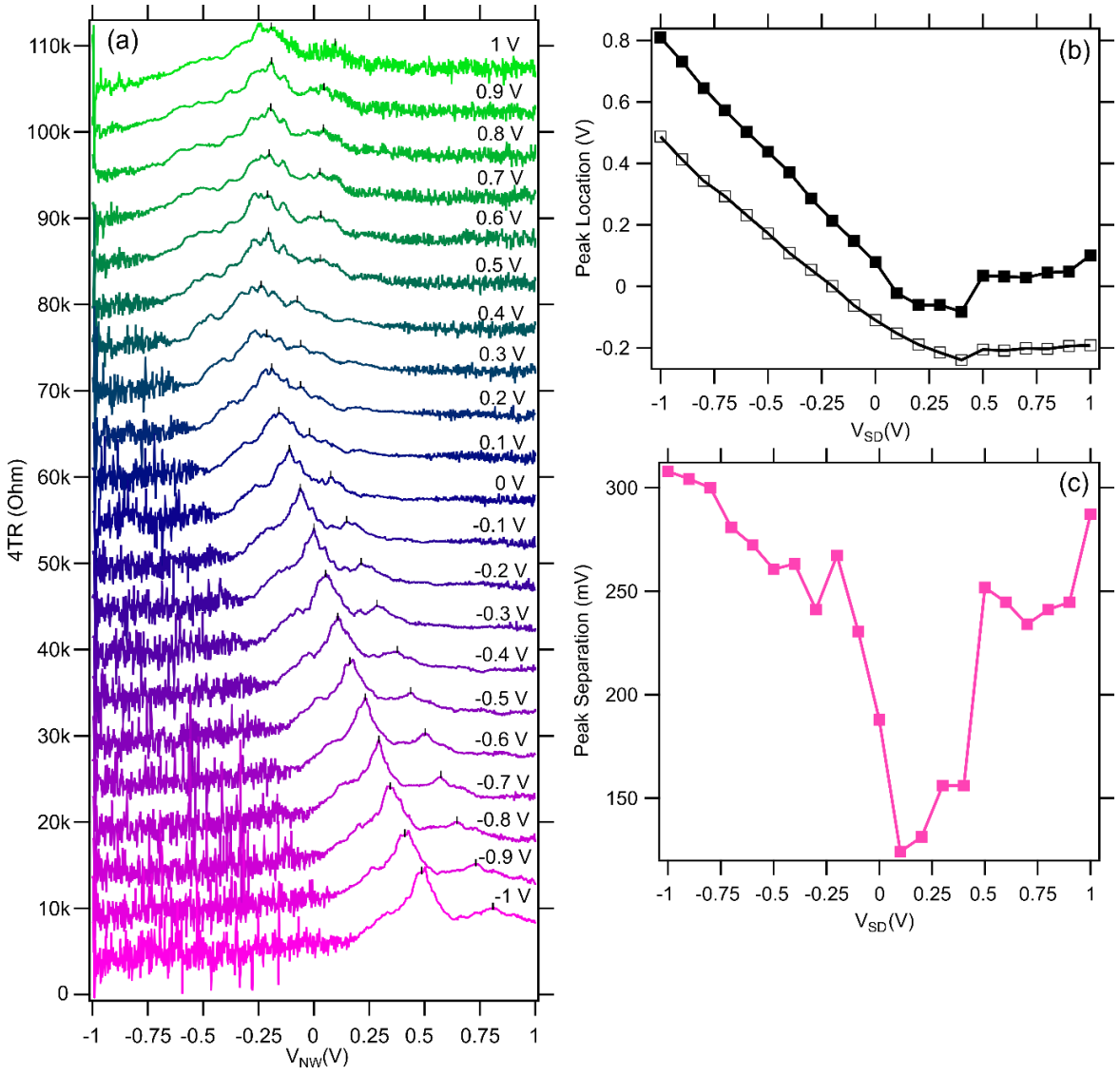

Figure 50: Dirac feature separation. (a) Graphene four-terminal resistance as a function of the nanowire gate for different V_{SD} values. Resistance curves are offset by 5 kOhm for clarity and labeled with their corresponding V_{SD} value. (b) Location of the two observed resistance peaks for each V_{SD} value. (c) Peak separation of two Dirac point maxima vs. V_{SD}.

As shown in Figure 50, preliminary experiments on **Device F** match our predictions. A plot of the Dirac point separation vs. V_{SD} shows a clear increase in peak separation as the magnitude of V_{SD} increases. However, the CNP appears quite broad, which obscures the clarity of the results to

some extent. Follow-up experiments are required to further clarify the nature of inhomogeneous doping of the graphene by the nanojunction.

4.3 Discussion

The strong, spectrally sharp, gate-tunable extinction features observed in the VIS-NIR range in G/LAO/STO are highly unusual given graphene's typical optical behavior. When the energy of the input radiation $\hbar\omega$ is greater than or equal to the Fermi energy 2μ of the graphene, $\hbar\omega \gtrsim 2\mu$, the conductivity of bulk Dirac fermions is predicted to be independent of frequency, and therefore the optical absorption of graphene should exhibit no resonant features[84]. Resonant absorption of light in graphene-based structures has been reported in the near-infrared or visible range[78,84,85,87,94,95] and has been ascribed to a variety of mechanisms, including magnetic polaritons, surface plasmon polaritons, and plasmonic resonances of nanostructures or underlying metallic or dielectric cavities. These plasmon resonances exist independently of the graphene, and the graphene merely intensifies or tunes an absorption resonance that is already there. In contrast to these methods, we believe that we have achieved near-total extinction of VIS-NIR light in graphene by utilizing its own plasmonic response.

To help identify the source of the resonant and nonlinear optical response, we focus on the inhomogeneous doping of graphene that exists within the ~10 nm gap of the LAO/STO nanowire junction. Additional evidence of inhomogeneous doping is shown in Figure 43(m), where there are two peaks in the four-terminal graphene resistance. The larger peak at $V_{NW} = 1.75$ V looks like a clear CNP, while the other at $V_{NW} = -2$ V is less clear. Since the graphene is being

subjected to quite large (~V/10 nm) electric fields from the nanojunction, one can expect there to be different CNPs at different spatial locations. The existence of two graphene CNP features supports this idea.

The gap dimensions are comparable to graphene nanoribbons, nanodisks and other quantum-confined structures[83,96,97], which may have quantized energy levels or other resonant modes. Quantum confinement is difficult to achieve in graphene due to its unique electronic structure, though it has been observed in the presence of combined electric and magnetic fields[97]. However, in such cases the energy level spacings are much smaller than the ~eV transitions reported here. It is difficult to imagine how a single quantum dot can by itself absorb or scatter light with >99.9% efficiency. If the incident energy were being re-radiated or scattered as electromagnetic waves by a quantum dot, it would have been detected by the LAO/STO nano-junction, and no such signal is observed here.

An alternate explanation is that VIS-NIR light is being absorbed by the graphene nanostructure and then efficiently converted into plasmons that propagate through the graphene medium. The generation of confined and guided graphene plasmons at VIS-NIR energies is already known to lead to absorption of light at the plasmon energy[83,96,98,99]. Indeed, a theoretical calculation of the plasmon energy for a 5 nm-wide doped graphene nanoribbon predicts dipole-mode plasmon energies ranging from 0.6 to 1.8 eV for Fermi energies of 0.5-2.5 eV with corresponding plasmon absorption at these energies[83]. We expect that a graphene nanoribbon-like nanostructure with a width of approximately 10 nm, under a strong electric field, can similarly host plasmons within the 1.4-1.9 eV energy range observed here. This behavior has been predicted elsewhere for graphene nano-islands[100]. Additionally, it has been shown that graphene nanoribbons host especially sharp and narrow plasmon resonances in the frequency domain[101], which could

account for the observed extinction features. Accompanying the striking VIS-NIR extinction features are the enhanced DFG and SFG responses. Graphene exhibits large, broadband and gate-tunable third-order optical nonlinearities[102-106]. We could therefore potentially attribute the observed strong nonlinear optical response in G/LAO/STO nanostructures to strong four-wave-mixing (FWM) processes in the planar graphene sheet. The observed DFG and SFG enhancement arises from a second-order optical nonlinearity in the graphene, however, and not a third-order nonlinearity, as with FWM. The second-order nonlinearity can plausibly be explained by the large symmetry-breaking electric dipole induced by the LAO/STO nanojunction. Breaking of inversion symmetry in graphene via applied current or voltage has previously been reported[107,108] and analyzed as a third-order nonlinear response where one of the frequencies is zero[33,109]. Additionally, nanostructured graphene is known to exhibit strong, plasmon-enhanced nonlinear optical behavior[100,110-112], which can help account for the correlation between the enhanced DFG and SFG response and extinction features.

We are unable to account for our observations by considering quantum confinement, four wave mixing processes, and intrinsic absorption in the graphene. Plasmon absorption/re-emission by nanostructured graphene remains a candidate mechanism to be explored in future experiments. A detailed explanation for the observed optical response of these G/LAO/STO nanostructures will certainly need to incorporate many other experimental details. For example, the G/LAO/STO nanostructure is excited with nearly transform-limited ultrafast femtosecond pulses, which are known to create non-equilibrium hot electrons and transient plasmons in graphene[113-116]. Patterned graphene under ultrafast optical excitation has also been shown to have an intense photocurrent response when at the CNP[117]. For a given frequency, the graphene plasmon momentum is greater than the momentum of the free-space light. In order to overcome the momentum mismatch

between the graphene plasmon and incident free-space light, the mismatch can be overcome by a sufficiently sharp object, such as a scanning probe microscope (SPM) tip[118,119], a lattice defect, or a periodic surface pattern[80]. These sharp objects serve to enhance the electric fields, so that the low-efficiency coupling rate is compensated. In our experiments, the biased LAO/STO nanojunction may play the role of a sharp object, enhancing the local electromagnetic fields. As discussed within the dissertation, the nanojunction confines a DC source-drain bias to 10 nanometer-scale regions, producing strong localized electric fields on the order of 1 MV/cm. This would obviate the need for an additional mechanism to overcome the momentum mismatch, such as an SPM tip, and allow for efficient coupling between the incident light and graphene plasmon.

In summary, in this chapter, we have created G/LAO/STO nanostructures that exhibit narrow-band, near-total extinction of light across a broad range of VIS-NIR frequencies, as well as strong second-order optical nonlinearities resulting in strong difference- and sum-frequency generation. The behavior is highly unusual, considering the low intrinsic absorption of graphene. In addition to their fundamental interest, these properties may potentially be utilized in a variety of nanophotonics and quantum optics applications. These nanostructures are useful in generating localized sources of THz emission which could be used for chemical identification with molecular sensitivity. The near-total, electrically tunable absorption could be replicated in a 2D array and used to create programmable amplitude or phase masks. The feasibility of these applications will depend, however, on a detailed understanding of the observed phenomena.

5.0 Nonlinear Optical Spectroscopy Graphene Nanoribbon/LAO/STO Nanojunctions

The work discussed in this section is the subject of a publication in APL Materials[120].

5.1 Introduction

Graphene nanoribbons (GNRs), quasi-one-dimensional honeycomb arrangements of carbon with precisely defined chemical makeup defined by synthetic chemistry, have emerged as a system of interest in low-dimensional condensed matter physics. On account of their high electronic mobility[121], high thermal conductivity[122], and low noise[123], they are also candidates for use in next-generation integrated circuits and other systems[124-126]. This is in part due to their unique electronic structure. Unlike pristine two-dimensional graphene sheets, GNRs often have energy band gaps[127,128]; furthermore, their electronic structure depends sensitively on their width, edge geometry, and dopants[129-132]. This allows for atomic-scale engineering of diverse physical properties[133,134].

GNRs are known to exhibit unusual optical properties, such as edge-dependent optical selection rules[135], and have been integrated into optoelectronic devices[123,136]. GNRs also host gate-tunable surface plasmon polaritons (or plasmons)[101,137,138], which can give rise to a plasmon-enhanced nonlinear optical response[139-142]. The integration of GNRs with other nanostructures opens up the possibility for many new device concepts, such as programmable nanoplasmonic arrays for use in integrated photonic circuits and GNR electron waveguides. These and other

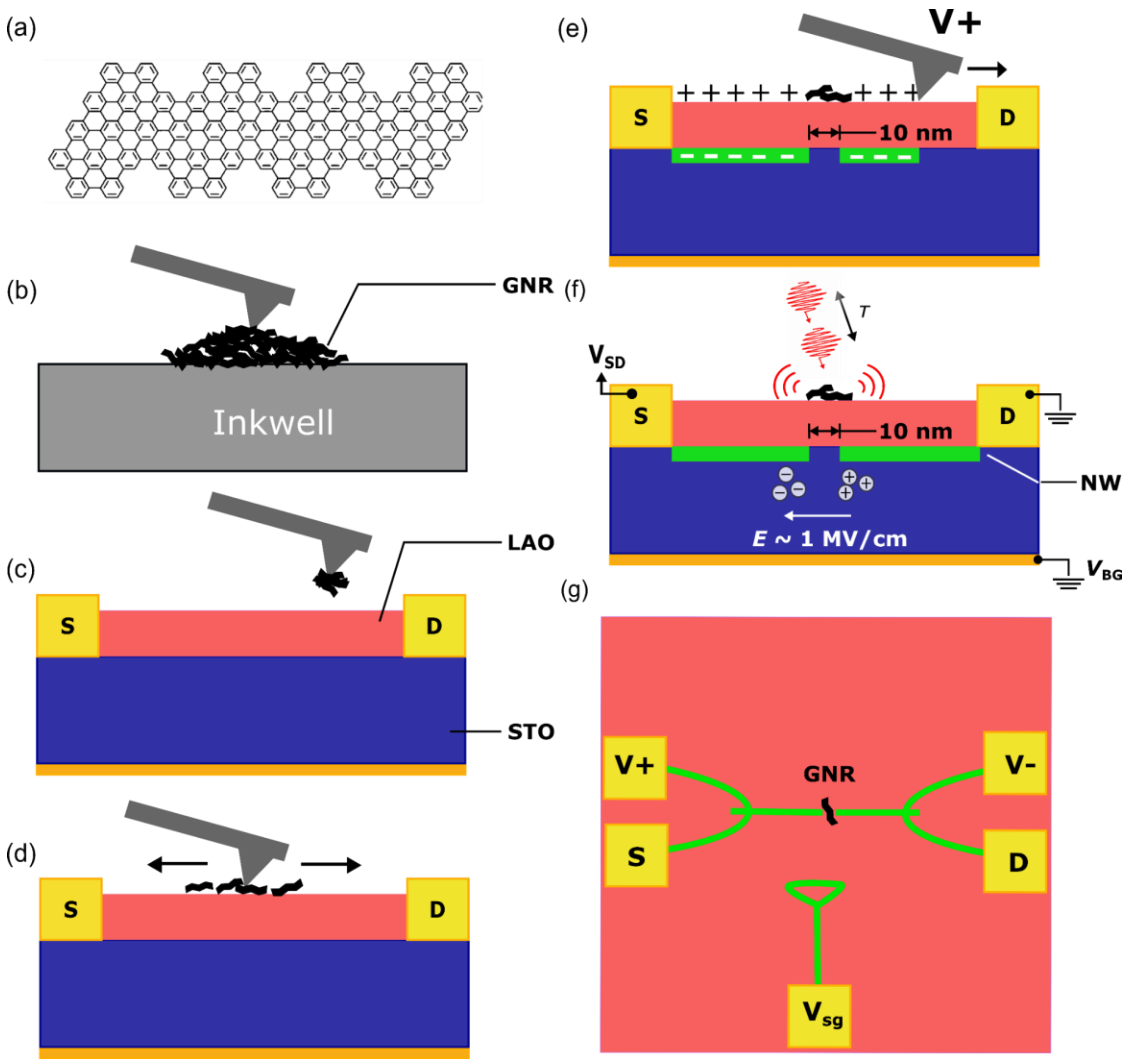

Figure 51: Graphene Nanoribbon Deposition. (a) Diagram of the chevron a-GNRs used in this work. (b) GNR "inkwell" consisting of a GNR powder on an LAO/STO substrate. An AFM tip is brought into contact with the inkwell and comes away with a small number of GNRs. (c) The tip with a small number of GNRs is brought to a clean LAO/STO sample. (d) The tip is scanned along the LAO surface in contact mode and sheds GNR nanoclusters. (e) A clean AFM tip is used to create a GNR/LAO/STO nanojunction via c-AFM lithography. (f) Time-domain optical measurements are performed on the gated GNR nanojunction device. +, - charges represent the dipole field established across the junction. (g) Top-view diagram of four-terminal nanojunction and nearby side gate nanowire.

devices further advance GNRs as a candidate material in nanophotonic and quantum information applications. Characterizing and integrating a small number of GNRs is necessary, as aggregation effects obscure their intrinsic properties[143], and precise control is required for quantum applications[144].

Integration of single or few GNRs into devices remains a challenge, however, as does characterization of GNRs optical response beyond ensemble measurements[145]. $LaAlO_3/SrTiO_3$ (LAO/STO) nanostructures are able to characterize the nonlinear optical response of materials like graphene[67], and have a variety of interesting optical and electronic properties themselves[1]. A wide range of LAO/STO-based optoelectronic devices have been created using conductive atomic force microscope lithography[28], including 10 nm-scale photodetectors[32] and nanoscale terahertz (THz) sources and detectors with >100 THz bandwidth[33,92]. Previously, the THz response of LAO/STO nanojunctions has been coupled to the plasmonic degrees of freedom in single gold plasmonic nanorods[93]. Graphene has recently been integrated with LAO/STO nanostructures as well[88,89,146], and graphene/LAO/STO nanojunctions exhibit gate-tunable, >99.9% extinction of visible-to-near-infrared (VIS-NIR) light and an enhanced nonlinear optical response[67].

In this work, we perform nonlinear optical spectroscopy of GNR nanoclusters using nanoscale junctions defined at the LAO/STO interface. First, we briefly detail a GNR deposition method with which one can controllably deposit a very small number of GNRs on a desired substrate with nanoscale resolution. We then discuss results obtained by using this method to integrate GNR nanoclusters into LAO/STO nanojunction devices. Specifically, time-domain photovoltage measurements reveal strong, spectrally sharp, gate-tunable extinction features at VIS-NIR frequencies in addition to an enhanced second harmonic generation (SHG) and third harmonic generation (THG) response. In the discussion section we will compare the observed

features in the GNR/LAO/STO nanojunctions to those in graphene/LAO/STO nanojunctions and offer an interpretation of our experimental results.

5.2 Inkwell Graphene Nanoribbon Deposition

The GNRs studied in this work are solution-synthesized semiconducting chevron-type GNRs. These have a bandgap of about 2 eV, which is notably smaller than other chevron GNRs. A powder of synthesized GNRs is created by annealing the synthesized solution in ultra-high vacuum. See Liu *et al.* (2020)[147] for growth and characterization details.

Small clusters of GNRs are placed on the surface of a 3.4 unit cell LAO/STO heterostructure using a process that is summarized in Figure 51 (b-e) and described in detail below[148-153]. First, some GNR powder is directly placed onto an LAO/STO substrate. A clean AFM tip is lowered into the GNR powder and raster scanned to pick up a small number of GNRs. The GNR-covered AFM tip is subsequently brought into contact with the LAO surface in the desired "canvas" region. To deposit few-GNR clusters, the tip is raster scanned in contact mode, shedding GNRs as it moves back and forth. Contact-mode AFM scanning can also be used to clean away unwanted GNR clusters. The GNR-coated AFM tip is then removed and replaced with a clean AFM tip, which is used to image the LAO surface in AC mode. In order to identify GNRs, the AFM image is compared with a reference image taken before depositing the GNRs. An AFM image of deposited GNR clusters is shown in Figure 53(a). Analysis of the AFM image, detailed in Figure 52, reveals a distribution of GNR clusters as small as 1-2 GNRs. The GNR cluster used for this investigation is estimated to contain roughly 10 GNRs.

A LAO/STO nanojunction device is created by first locating a GNR cluster using an AFM. A nanojunction device that surrounds the single GNR nanocluster is then written using c-AFM lithography[93]. The nanojunction consists of a conducting LAO/STO nanowire with a nanoscale

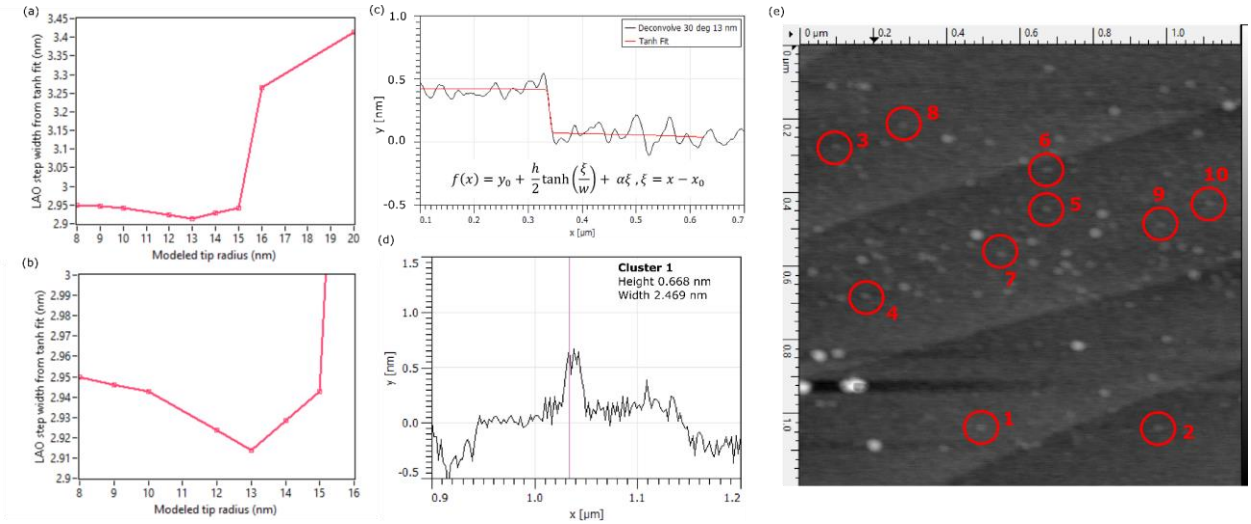

Figure 52: AFM Analysis of GNR Nanoclusters. (a,b) Measured LAO step width versus modeled tip radius. (c) Example line profile of LAO step with tanh fit. (d) Line profile of GNR cluster 1 after the 13 nm radius tip is deconvolved from the AFM image. (e) Reconstructed AFM image of GNR clusters deposited on LAO.

(~10 nm) insulating gap enables tunable electric fields on the order of 1 MV/cm to be applied directly to the GNRs. The GNR nanocluster is located on the LAO surface directly above the nanojunction gap, as shown in Figure 51 (f,g) and Figure 53 (b). A nearby looped nanowire serves as a "side gate" to adjust the chemical potential in the device[31,38]. Additional details of c-AFM lithography and LAO/STO sample growth can be found in Section 2.1.

After the device is written, the sample is transferred to an optical cryostat, where it is pumped to high vacuum and cooled to a temperature between 5-50 K. The optical response of the GNRs is measured by the same LAO/STO nanowire junction, which behaves as a broadband near-field photodetector[32]. As shown in Figure 53 (c), a source-drain bias (V_{SD}) is applied across the nanostructure, which is illuminated by ultrafast pulses. The induced photovoltage across the

LAO/STO nanojunction, $\Delta V(\tau) = V_+(\tau) - V_-(\tau)$, is measured as a function of the time delay τ between two pulses.

5.2.1 AFM Image Analysis

GNR clusters are deposited via the Inkwell deposition method using an Aspire-CMFR AFM probe. These probes have conical tips with a 30 degree tip cone angle and an estimated 10 nm tip radius. To obtain a highly accurate AFM measurement of GNR cluster sizes, it is necessary to account for the tip's influence on the AFM image. To this end, we model and deconvolve the tip from the AFM image as described below.

First, we perform a step height calibration to obtain an accurate value for the tip radius at the time of measurement. Using Gwyddion SPM analysis software[154], we model AFM probes matching the Aspire-CMFR AFM probe specifications, with modeled tip radii ranging from 8 nm to 20 nm. The LAO surface has a smooth terrace structure with 4 angstrom steps. A deconvolution is performed on an AFM image of GNR clusters deposited on LAO/STO for each modeled tip, and a step height measurement is taken of the deconvolved LAO surface.

A vertical line profile is taken of an LAO step at the same location of the same AFM image for each modeled tip deconvolution, then is fit with a "Boltzmann bent step" function:

$$f(x) = y_0 + \frac{h}{2}\tanh\left(\frac{\xi}{w}\right) + \alpha\xi\,, \xi = x - x_0 \qquad \textbf{Equation 31}$$

where w is the step width, and it is understood that the most accurate tip deconvolution will provide the smallest step width. A plot of the step width versus modeled tip radius is shown in Figure 52.

A local minimum is located at the rip radius value of 13 nm, which we take to be the actual radius of the tip.

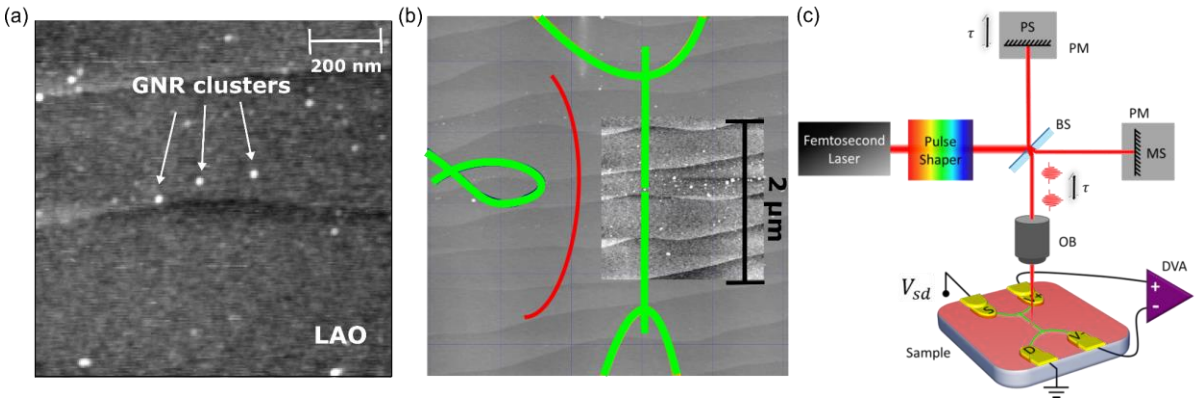

Figure 53: GNR/LAO/STO Nanojunction. (a) AFM image of GNR clusters deposited on LAO surface. The rightmost labeled cluster is used for the device in panel (b). (b) AFM image of GNR/LAO/STO nanojunction. A GNR nanocluster is located in the center of the nanojunction gap on the LAO surface. The red line represents a negative-voltage wire which ensures that there is no leakage between side gate and nanojunction. (c) Diagram of optical measurement setup. BS: beam splitter, PM: plane mirror, MS: mechanical stage, PS: piezoelectric stage, OB: objective, and DVA: differential voltage amplifier. The dimensions are not to scale.

Next a surface reconstruction is performed to remove the influence of the modeled 13 nm radius tip, as shown in Figure 52(e). After that, the size of the deposited GNR clusters is measured by taking line profiles in the vertical (slow scanning) direction. Ten of the smallest visible GNR clusters are measured in this manner, and the width and height of each cluster is obtained using Gwyddion's built-in peak finder function and summarized in Table 3 below. A volume estimate is calculated by calculating $height \times (width)^2$. The obtained volume estimate is also converted to a "standard volume" unit. This unit is defined using dimensions provided in Liu *et al.*[147] for the GNRs used in this study. Specifically, a single GNR is taken to have dimensions $1.7\ \text{nm} \times 5.08\ \text{nm} \times 0.3\ \text{nm} = 2.591\ \text{nm}^3$. Using this method, the GNR cluster used in the

device pictured in Figure 53**(b)** is found to have a volume of 12.733 standard volumes, as summarized in Table 4.

Table 3: GNR Nanocluster Measurements.

Cluster #	Height (nm)	Width (nm)	Volume Estimate $H*W^2$ (nm^3)	Standard volumes
1	0.668	2.469	4.072	1.571
2	0.369	2.978	3.272	1.263
3	0.306	2.564	2.013	0.777
4	0.417	3.960	6.539	2.523
5	0.400	2.270	2.061	0.795
6	0.374	2.968	3.294	1.271
7	0.487	3.081	4.622	1.783
8	0.358	1.252	0.561	0.216
9	0.351	2.720	2.596	1.001
10	0.460	3.992	7.330	2.829
Average	**0.419**	**2.825**	**3.636**	**1.402**

Table 4: Measurement of the GNR cluster studied in this work.

Cluster #	Height (nm)	Width (nm)	Volume Estimate $H*W^2$	Standard volumes
Device	0.475	8.334	32.991	12.733

5.3 Experimental Results

After the device is written, the sample is transferred to an optical cryostat, where it is pumped to high vacuum and cooled to a temperature between 5-50 K. The optical response of the

GNRs is measured by the same LAO/STO nanowire junction, which behaves as a broadband near-field photodetector[32]. As shown in Figure 53(c), a source-drain bias (V_{SD}) is applied across the nanostructure, which is illuminated by ultrafast pulses. The induced photovoltage across the LAO/STO nanojunction, $\Delta V(\tau) = V_{+}(\tau) - V_{-}(\tau)$, is measured as a function of the time delay τ between two pulses.

As discussed in Section 3.0, LAO/STO nanojunctions have been shown to locally generate and detect THz emission[13], with greater than 100 THz bandwidth, via the third-order nonlinear optical process in STO. V_{SD} creates a quasi-static electric field $\vec{E}_{\mathrm{SD}}$ across the junction that is highly confined in space to ~10 nm, while input optical fields $\vec{E}_{opt}(\omega_1), \vec{E}_{opt}(\omega_2)$ are sharply peaked in the time domain. The three electric fields mix to generate the nonlinear response of the nanojunction[92]. The power spectrum $S(\Omega)$ versus frequency Ω is calculated by taking a Fourier transform of the photoresponse $\Delta V(\tau)$ with respect to τ.

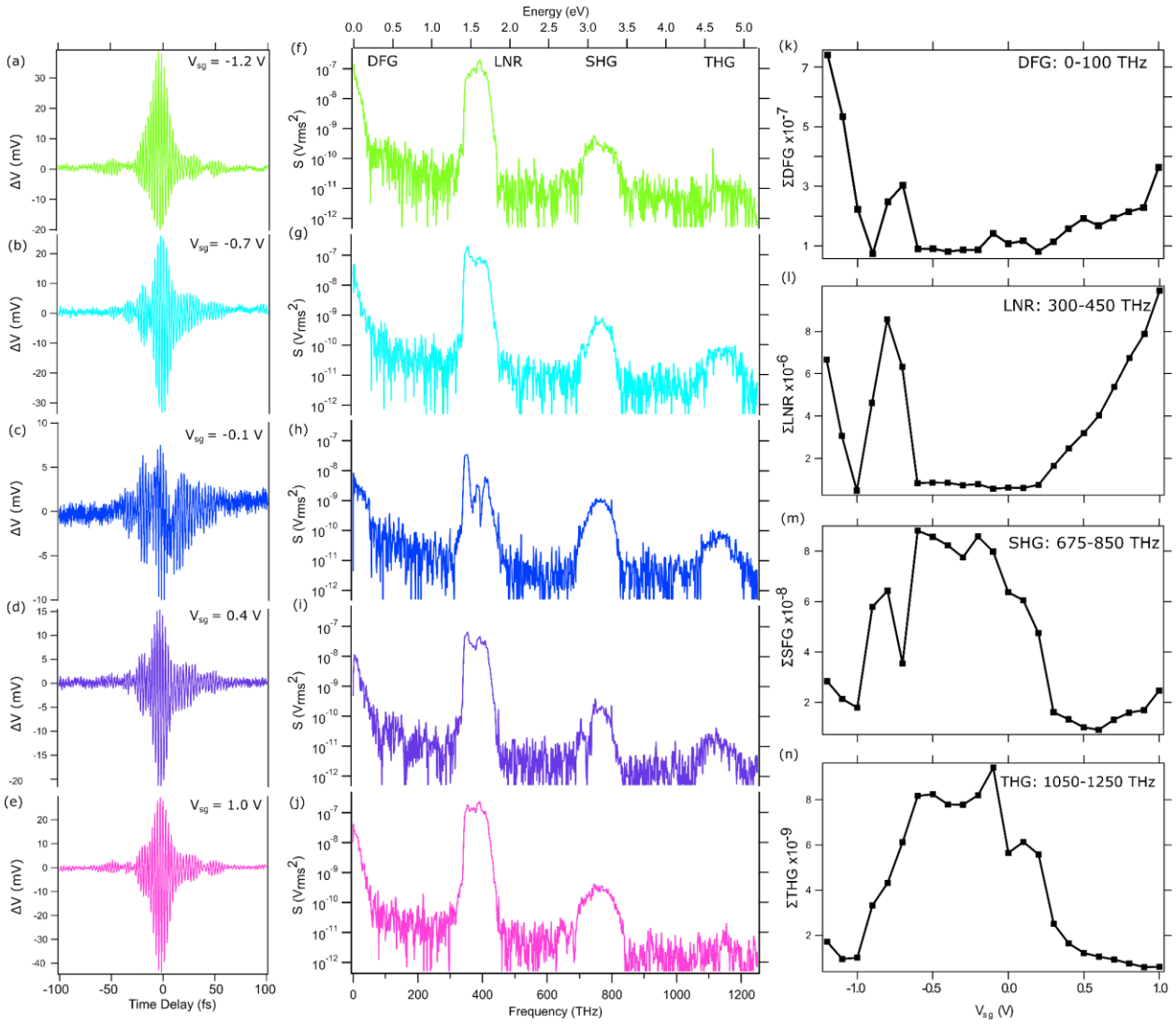

Figure 54: Side-gate Dependence of Optical Response. (a-e) Time-domain signals and (f-j) corresponding power spectra at 5 different side gate values. Power spectra regions are labeled in panel (f). Integrals of the (k) DFG, (l) LNR, (m) SHG and (n) THG responses reveal correspondence between the DFG and LNR response, and between the SHG and THG response. $T = 5$ K, $V_{SD} = -0.75$ V, input power 8 μW.

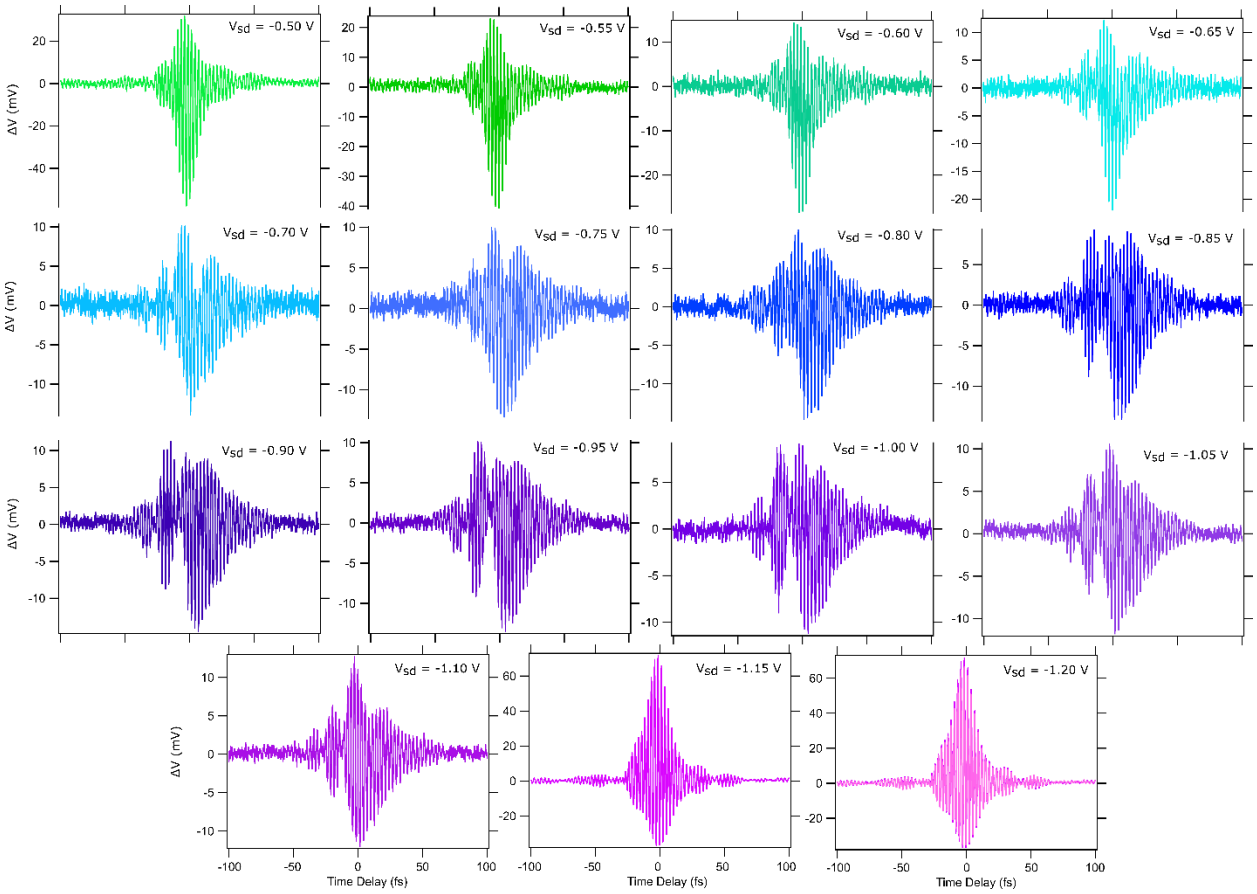

Figure 55: Source-Drain Bias-Dependent Time-Domain Signals.

The optical response of GNR/LAO/STO nanostructures is measured as a function of the side gate bias V_{sg}, illustrated in Figure 54(c). Five representative time-domain signals $\Delta V(\tau)$, acquired at different V_{sg} values, are plotted in Figure 54(a-e), along with their corresponding power spectra Figure 54 (f-j). Two sharp VIS-NIR extinction features are observed in the LNR response at 395 THz when $V_{sg} = -0.1$ V. An additional extinction feature is observed in the SHG response at $V_{sg} = 0.4$ V. These spectrally sharp extinction features are similar to those observed in graphene/LAO/STO nanojunctions[67]. Additionally, the integrated spectral response over four regions of interest (Figure 54 (k-n)) reveal correlations between the linear and nonlinear responses of the device. The integrated amplitude of the DFG (0-100 THz) response is correlated with the

LNR (300-450 THz) response, while the SHG (675-850 THz) response is correlated with the THG (1050-1250 THz) response. In particular, the SHG and THG are maximal near the V_{sg} value where the VIS-NIR extinction feature appears. Finally, the sign of the envelope of the time-domain photovoltage signal at $V_{sg} = -1.2$ V is opposite to what is measured for $V_{sg} = 1.0$ V. A similar sign reversal is also observed as a function of the source-drain bias V_{SD}.

Indeed, the optical response of the GNR/LAO/STO nanojunction can also be tuned as a function of the source-drain bias V_{SD}. For this experiment, $V_{sg} = 0$ V, $T = 5$ K. Figure 55 shows time-domain photovoltage signals as a function of V_{SD}, and corresponding power spectra and integrals of the regions of interest are plotted in Figure 56. A compelling similarity in the power spectra integrals appears: the SHG and THG signals have local maxima when VIS-NIR extinction features appear. Furthermore, once the time-domain signal "flips," there is a sudden jump in the power spectra integrals, denoting a sharp change in the behavior of the GNRs. Notice that the sign of the envelope of the time domain signal flips near $V_{SD} = -1$ V, in a similar manner as the V_{sg} dependence experiment.

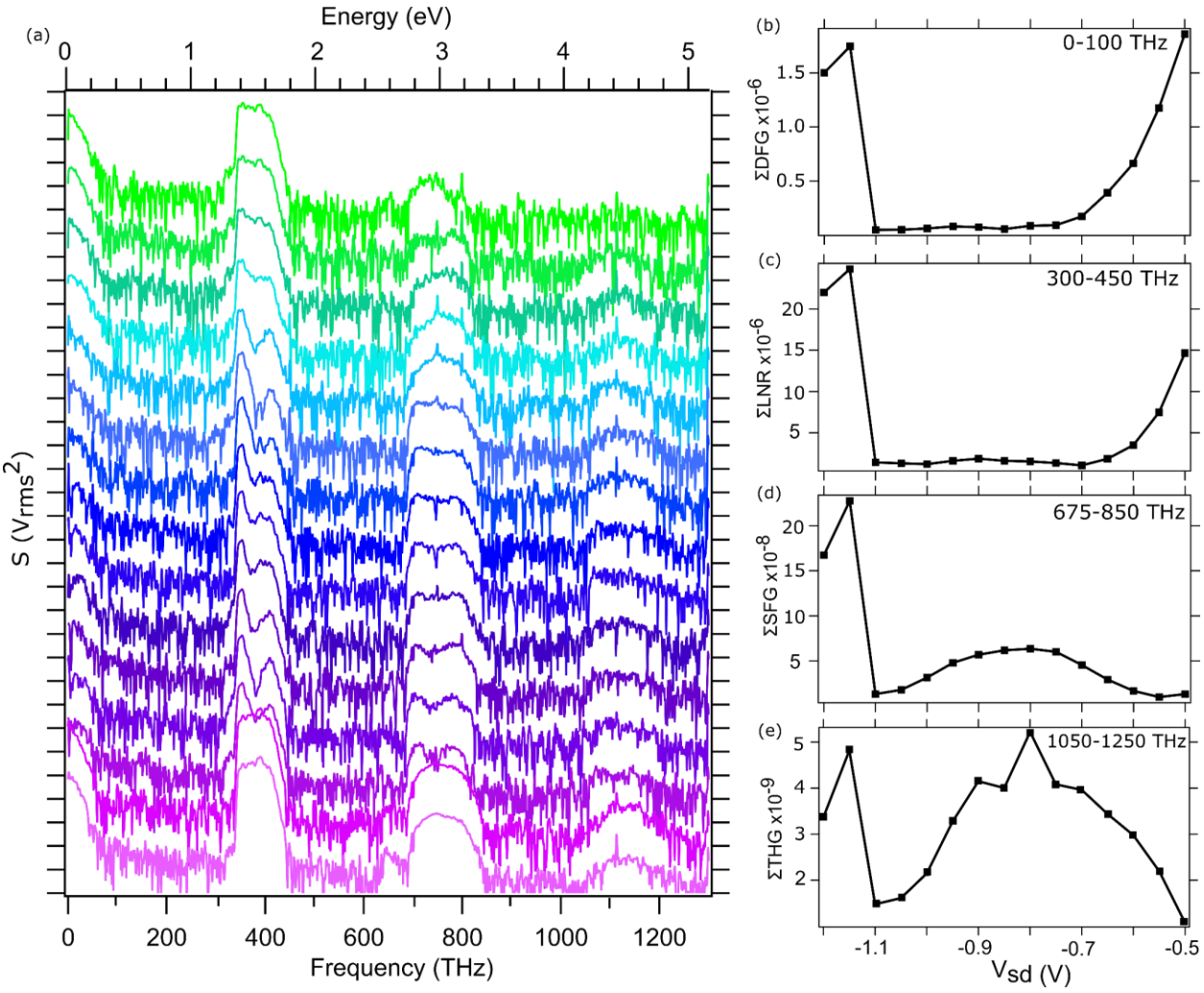

Figure 56: Source-Drain Bias-Dependent Power Spectra and Integrals.

To study the power dependence of the extinction feature, an ultrafast pulse shaper was used to vary the input power to the device between 3 μW and 6 μW, while otherwise preserving the temporal profile of the optical pulse. This experiment, summarized in Figure 57**,** shows that the extinction depth and local minimum location exhibits a sensitivity to the power that is similar to what was reported for a graphene/LAO/STO nanojunction, in that the input power can be used to finely tune the extinction ratio and frequency.

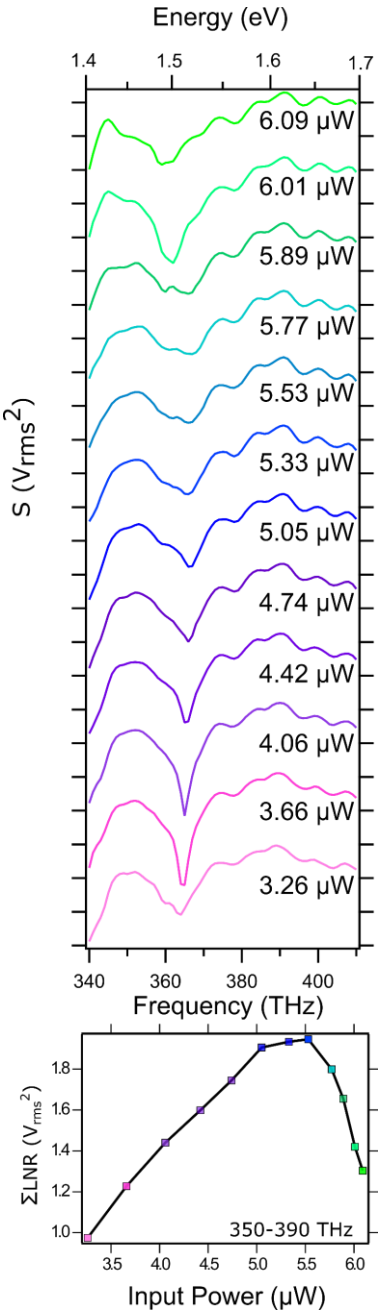

Figure 57: Power Dependence of GNR/LAO/STO Extinction. Top: Waterfall plot of VIS-NIR region of power spectra zoomed in to the vicinity of an extinction feature. Each tick mark denotes two orders of magnitude and plots are vertically offset for clarity. $T = 50$ K, $V_{SD} = -500$ mV, $V_{sg} = 0$ V. Bottom: integral of power spectrum from 350-390 THz, revealing the gate-dependent depth of the extinction feature.

A particularly striking example of a VIS-NIR extinction feature in a GNR/LAO/STO device is shown in Figure 58(a). We can estimate the extinction percentage by taking the amplitude of the power spectrum at the extinction frequency (366 THz) and comparing it to the amplitude of the same spectrum at 355 THz, just to the left of the extinction feature. A simple division of the two amplitudes results in a 99.93% estimated extinction of light. Figure 58(b) shows a qualitatively similar extinction feature in a graphene/LAO/STO nanojunction device under similar experimental conditions.

5.4 Discussion

Graphene integrated with LAO/STO nanojunctions exhibits gate-tunable, >99.9% extinction of VIS-NIR light and an associated enhanced nonlinear optical response[67]. Similar VIS-NIR extinction features appear in GNR/LAO/STO nanojunctions and graphene/LAO/STO nanojunctions under similar experimental conditions, and exhibit similar gate-dependent and power-dependent behavior. What's more, the SHG and THG responses are both maximized when the VIS-NIR extinction feature appears. It is important to note that both the SHG and THG responses are enhanced, despite the fact that SHG is an even-ordered harmonic and THG is an odd-ordered harmonic. This is in contrast to previous work, in which only THG is enhanced[142].

The exact physical mechanism underlying the remarkable optical extinction in both graphene and GNR/LAO/STO nanojunctions is still unresolved. However, the fact that such

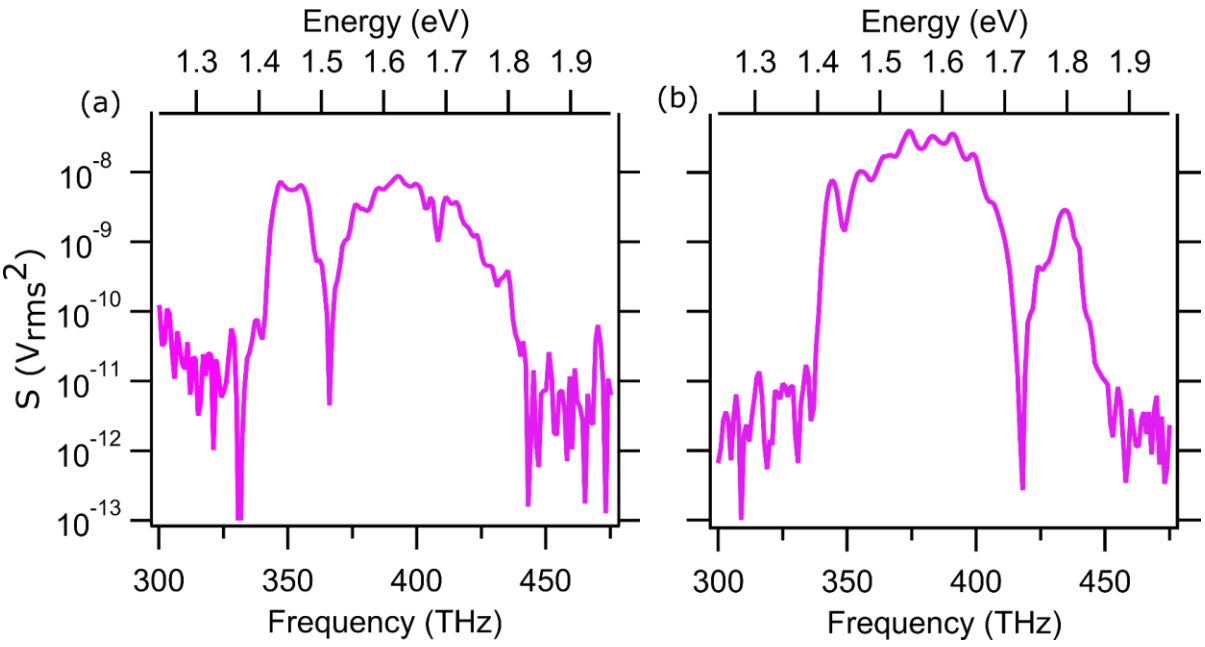

Figure 58: Extinction Features in Graphene and GNRs.VIS-NIR extinction features in (a) GNR/LAO/STO nanojunction ($T = 5$ K, $V_{SD} = -25$ mV, $V_{sg} = -350$ mV) and (b) graphene/LAO/STO nanojunction ($T = 10$ K, $V_{SD} = -1.25$ V).

similar behavior is observed in both systems indicates that the mechanism in graphene is localized at the junction and very likely involves the generation of gate-tunable plasmons. LAO/STO nanojunctions confine a ~1 V source-drain bias to a ~ 10 nm region, creating extremely large dipole electric fields directly beneath the GNR nanocluster. Such strong electric fields, on the order of 1 MV/cm, should strongly couple to the plasmonic modes of the GNRs and push them to the highly gated regime. It has been shown that in this regime, nanostructured graphene can host VIS-NIR plasmons[83], and in that case, plasmon absorption should lead to extinction of VIS-NIR light at the plasmon energy. The clear resemblance between the graphene and GNR LAO/STO nanojunction responses implies that the extinction features in graphene are likely the result of a confined GNR-like structure induced by the large electric field.

Graphene plasmons concentrate light into nanometer-scale volumes, significantly intensifying the electric fields upon which nonlinear optical phenomena depend[140,141,155,156]. Previous theoretical results have shown that doped graphene nanostructures exhibit plasmon-assisted high harmonic generation at odd and even harmonics[139]. Therefore, the observed robust SHG and THG in GNRs could be attributed to a plasmon-enhanced nonlinear optical response. It is important to note that in graphene/LAO/STO nanojunctions, the DFG response is maximized when VIS-NIR extinctions appear[67], while in GNR/LAO/STO nanojunctions, the DFG enhancement occurs elsewhere. Planar graphene has been shown to exhibit plasmon-enhanced optical rectification when inversion symmetry is broken [157]. This effect is not necessarily present in GNRs, which could explain why the behavior of the DFG response varied between graphene and GNR nanocluster junctions.

Finally, as shown in Figure 54, the sign of the envelope of the time domain signal changes at a particular V_{sg} value. Switching behavior is also observed as a function of the source-drain bias V_{SD}. One possible explanation could be that the sign change is associated with a doping change within the GNRs from *n*-type to *p*-type[158-161].

Although GNRs may play an important role in next-generation electronics, photonics, and possibly quantum information applications[144,162], integrating single- or few-GNRs into nanoscale devices remains difficult[131,163], as is achieving desired electrical performance[159]. The deposition technique utilized in this work allows for the placement and integration of GNR clusters as small as 1-2 GNRs in size with nanoscale control. Furthermore, c-AFM-defined LAO/STO nanostructures can effectively contact and gate the deposited clusters without requiring complex nanofabrication methods, and gate-dependent optical studies reveal VIS-NIR extinction features

and strong optical nonlinearities. Indeed, >99.9% extinction of light is achieved in a GNR nanocluster in a frequency range where graphene typically absorbs only ≈ 2% of light[71].

We have performed nonlinear optical spectroscopy on GNR nanoclusters deposited on LAO/STO. GNR/LAO/STO nanojunctions are shown to exhibit gate-tunable, narrow-band, near-total (> 99.9 %) extinction of light across a broad range of VIS-NIR frequencies as well as strong second-order and third-order optical nonlinearities. The observed extinction features and nonlinear response bear a strong resemblance to those observed in graphene/LAO/STO junctions. The integration of GNRs with LAO/STO nanostructures opens up the possibility for many new device concepts, such as programmable nanoplasmonic arrays and GNR/LAO/STO electron waveguides. These and other devices further advance GNRs as a candidate material in nanophotonic and quantum information applications.

6.0 Measurements of Two-Junction Graphene/LAO/STO Devices

6.1.1 Two-Junction Correlation Measurement

A deeper understanding of the interaction between the two LAO/STO junctions separated by 7 μm can be obtained by measuring their responses in a cross-correlation configuration, as shown in Figure 59 (a). Pump and probe beams are separated, with one beam focused on each junction. The two nanojunction devices are both located on a single sheet of graphene.

In this experiment, the bottom nanowire gate V_{NW}^{1} is swept from 0 V to 3 V at $T = 5\ K$, $V_G = 0\ V$, $V_{SD}^{2} = -2.5$ V, $V_{SD}^{1} = -1.5$ V and input power 109 μW. The main result of this experiment is shown in Figure 59(b,c). Interference fringes are observed in the LNR response of both devices. These fringes are separated by 9-10 THz, which corresponds to a 100-111 fs travel time. When we divide the distance between the two junctions, by this travel time, we get:

$$\frac{7\ \mu m}{100\ fs} = \frac{7\ \times 10^{7} m}{s} = \sim 0.21c \qquad \textbf{Equation 32}$$

which is a plausible velocity for propagating graphene plasmons. In gated structures, the velocity of graphene plasmons can be tuned by the voltage applied. At low bias voltages the plasmons are strongly damped due to interband transitions of electrons. At high bias voltages, however, these transitions are forbidden by Pauli blocking, and the voltage and propagation length of plasmons is limited only by Drude absorption[164].

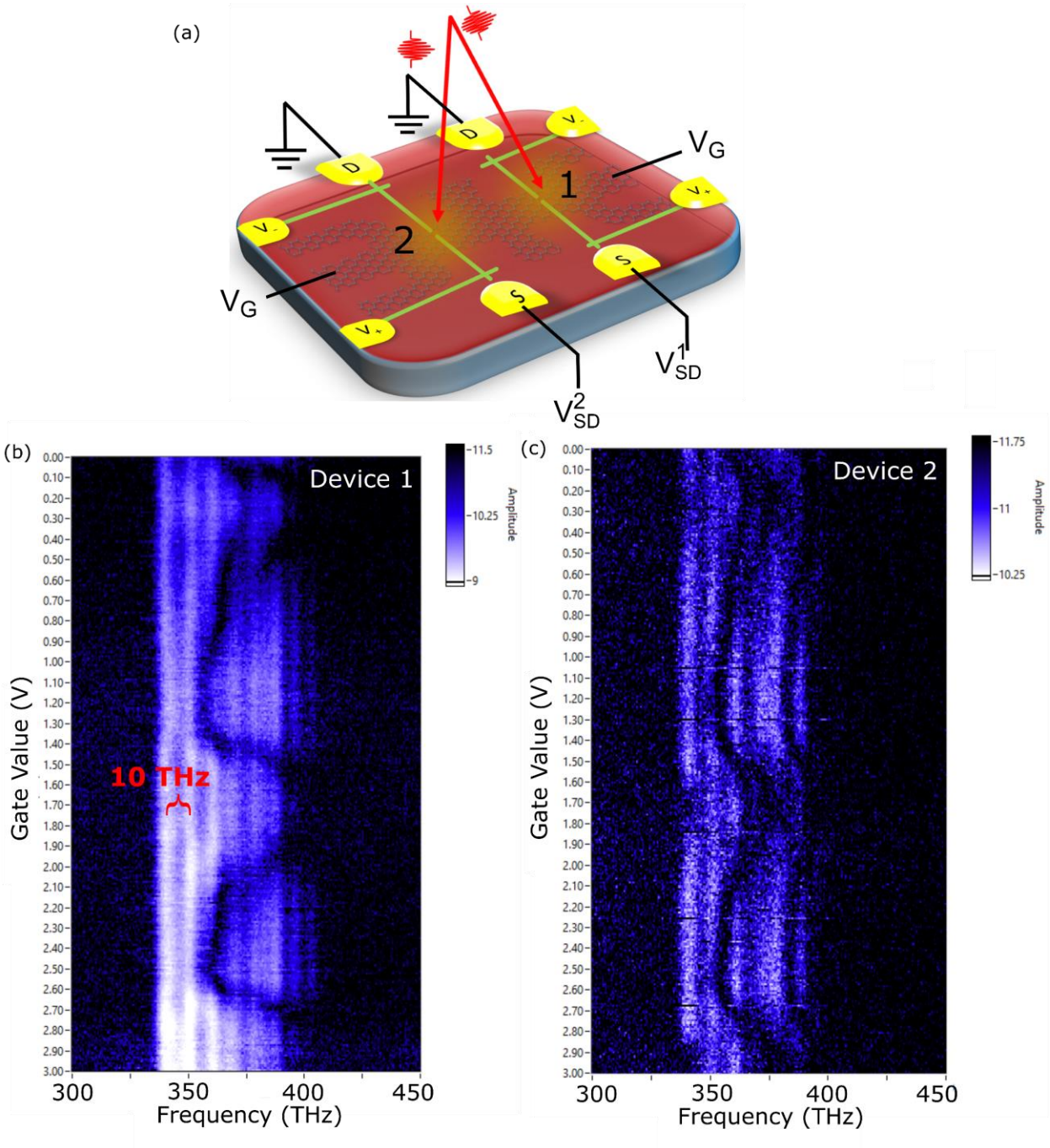

Figure 59: Two graphene nanojunction correlation measurement. (a) Experimental configuration. (b,c) Simultaneously measured spectra from devices 1 and 2 as a function of V_G.

6.1.2 Possible Observation of Extreme Nonlinear Optical Effects

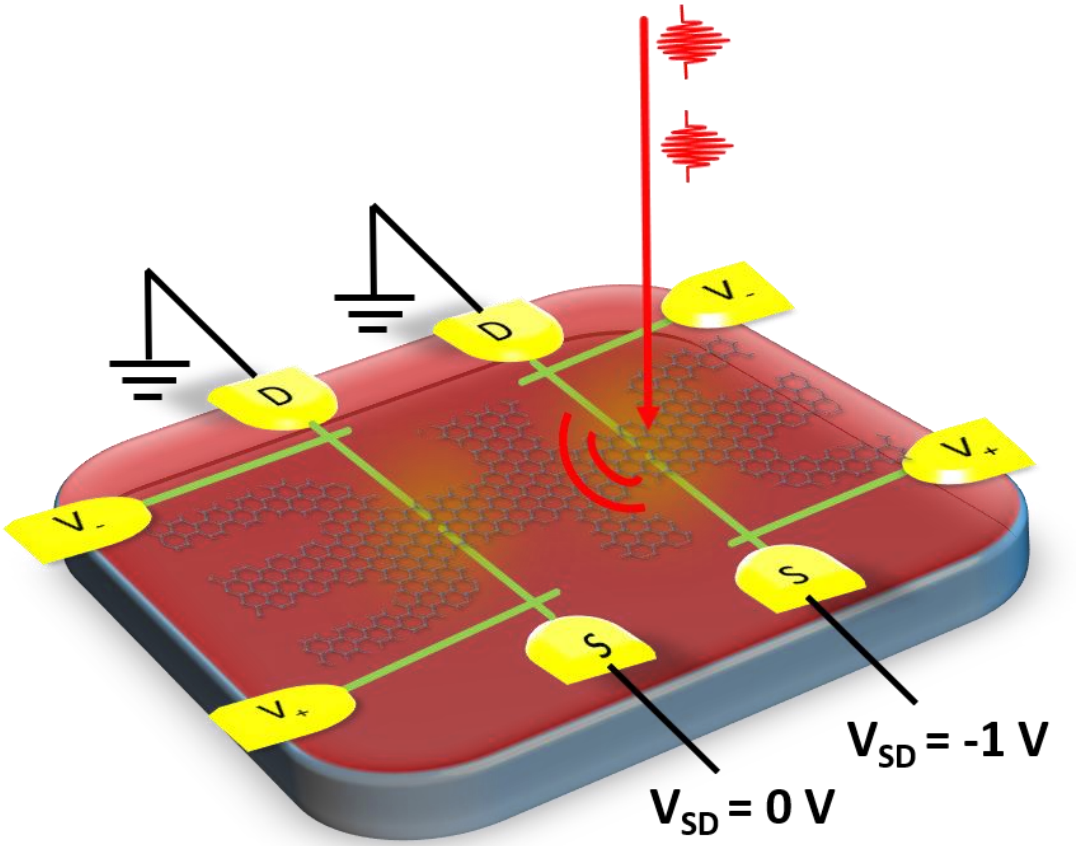

Figure 60: Two-junction generator and detector geometry.

Preliminary results on two-junction graphene/LAO/STO nanojunction devices, where the input light is focused on one junction (called the "generator") and a second junction is unbiased and unilluminated (called "the detector") may reveal signatures of high-order harmonic generation in graphene. The configuration is summarized in Figure 60. This phenomenon remains under study, and these results will be the subject of future work.

7.0 Future Directions

7.1 Pulse compensation with LAO/STO Nanoscale Junctions

As the LAO/STO nanojunction has a nonlinear optical response, it should act as a nonlinear detector for the MIIPS pulse compensation algorithm. Specifically, the nonlinear BBO crystal can in principle be replaced by the second harmonic response of the junction. Using the junction or pulse compensation carries the advantage of compensating a pulse directly at the sample surface-providing a means for the most accurate possible compensation. Experiments to realize this application of LAO/STO junctions are currently in preparation.

7.2 Graphene Nanoribbon Qubit Platform

The work put forth in this thesis, especially in Chapter 5.0, lays the foundation for a unique and promising platform for solid-state quantum bits and quantum memory. The Levy Lab is currently working to use graphene nanoribbons (GNRs), to build new families of spin qubits. The ultimate goal of this project is to lay the groundwork for a scalable solid-state quantum information processing platform.

The unique structural characteristics of GNRs, combined with unique electrical gating and sensing provided by these partnering materials, can give rise to new families of topologically stabilized spin qubits, and create new modalities for controllable entanglement and efficient transfer of spin quantum information. These new capabilities do not exist in competing platforms,

and would represent a breakthrough in the development of solid-state quantum information technology. The work contained in this thesis has established that individual GNRs can be integrated with LAO/STO nanostructures. Future versions of these structures will be equipped with multiple lateral gates that will enable strong local modification of electronic properties, which will in turn be used to create and manipulate quantum information within the GNRs.

7.2.1 Optical Spectroscopy of Conducting GNRs

One milestone experiment will be to measure the predicted dimerization gap within a metallic spin chain GNR as a function of the applied transverse electric field. The gap energy (Figure 7(c)) provides a direct measurement of an important engineerable energy scale that will provide direct control over the electron spin degrees of freedom and therefore any type of logical spin qubit. With two transverse gates it will be possible to perform time-domain THz spectroscopy to reveal the induced semiconducting gap.

Furthermore, fast addressing and readout of spin qubits can be achieved by indirectly addressing the spin states via optically active electronic excitations. Ultrafast drive pulses can be used to implement single-qubit and multi-qubit quantum gates using approaches based on optical control. This optical addressing can ultimately be integrated with silicon photonic devices, which are likely going to form the backbone of quantum communication channels, and thus allow for interfacing of the GNR-based qubits with quantum networks.

7.2.2 GNR/LAO/STO Waveguides

In addition to the described optical experiments, the group will perform milli-Kelvin magneto-transport experiments designed to initialize, read out and gate GNR based spin qubits. The measurement and control of the qubits will be enabled through the detection and control of the charged/uncharged state of the GNR in an LAO/STO waveguide device.

7.3 Signatures of harmonic generation in graphene

Preliminary results hint at the possibility that high-order harmonics can be generated by graphene/LAO/STO nanojunctions under intense illumination. Continued studies of the interactions of two-nanojunction graphene/LAO/STO devices will explore this possibility further.

7.3.1 Carrier Envelope Phase Stabilization

Device functionality and could also expanded by introducing carrier envelope phase stabilization to the ultrafast pulses[165,166]. In perturbative nonlinear optical phenomena, the nonlinear polarization can be understood in terms of envelope functions and an input intensity averaged over a few optical cycles. In contrast, nonperturbative phenomena in the strong-field regime arise from the sub-cycle dynamics of bound electrons, meaning the extreme nonlinear responds directly to the instantaneous (carrier) field within a single cycle.

7.3.2 EBL nanolithography

Additionally, given recent advances in LAO/STO nanolithography techniques, it will be straightforward to increase the nanojunction number from two to many[167], enabling the creation of an electronically controllable array of extreme ultraviolet high harmonic generators and detectors.

7.3.3 Second harmonic emission measurement

It is desirable to have a non-interferometric, direct observation of the light generated via the nonlinear response of an LAO/STO nanojunction. To that end, work is currently underway to build an experiment where the second harmonic generated light from a nanojunction is output from the Michelson interferometer and measured with an avalanche photodetector. The second harmonic light from VIS-NIR input pulses should be at an energy of ~ 3 eV, which should be visible as blue-violet light.

To direct the blue light from the device to a photodetector, the VIS-NIR 50/50 beamsplitter used to measure reflection is replaced with a dichroic mirror. This mirror separates the VIS-NIR light from the blue light as shown in Figure 61. Dichroic mirrors (or beamsplitters) spectrally separate light by transmitting and reflecting light as a function of wavelength. Longpass dichroic mirrors, like the one used here, have transmission and reflection bands that are divided by what is called the cut-on wavelength. The mirror is highly reflective below the cut-on wavelength and highly transmissive above it.

This experiment is currently underway.

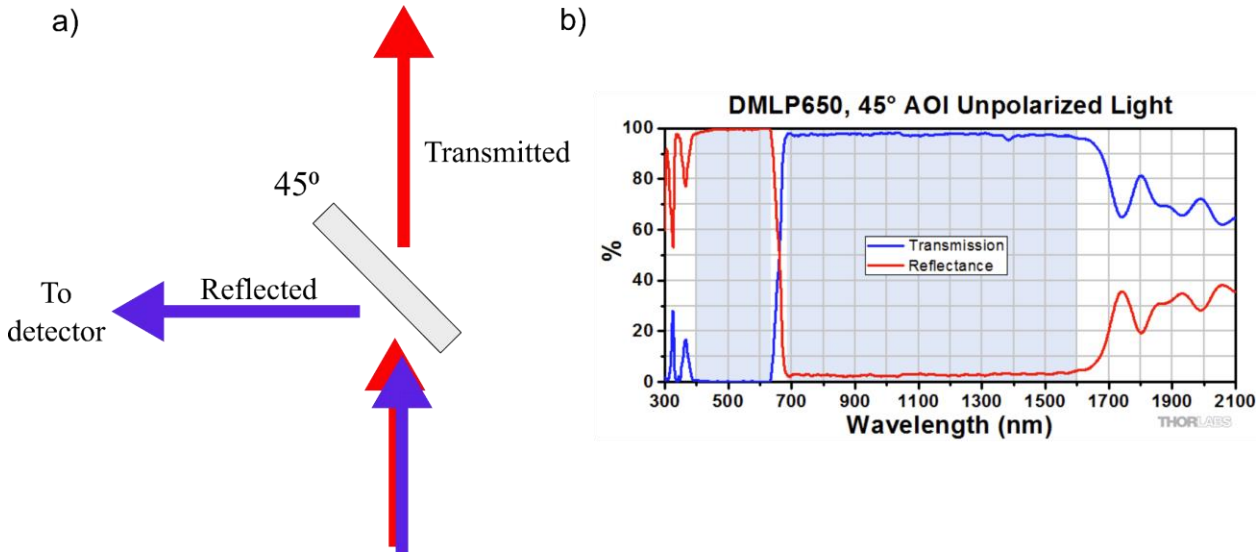

Figure 61: Dichroic mirror. (a) Diagram of dichroic mirror used within interferometer to output blue light. (b) Measured reflectance and transmittance of mirror as a function of wavelength.

Appendix A Pulse Shaper Calibration

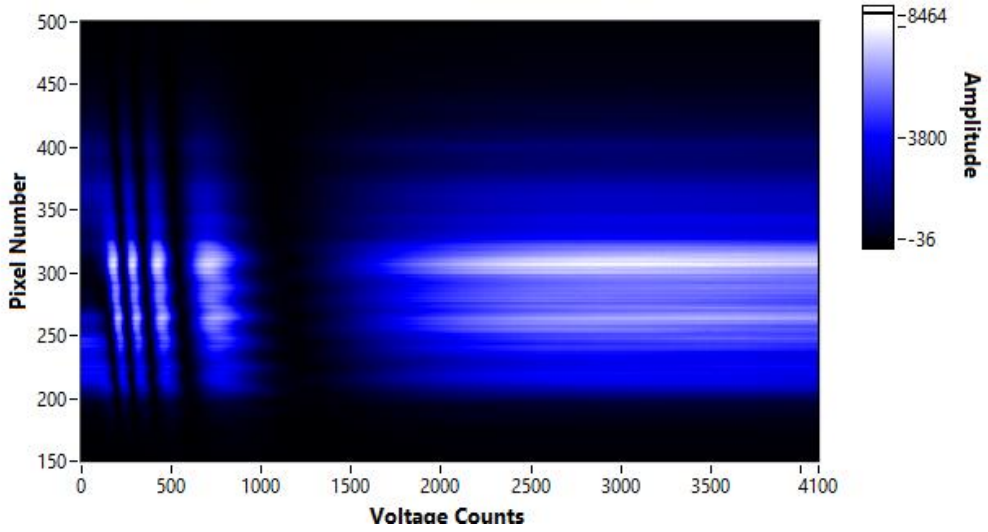

Appendix Figure 1: Voltage-Transmission Calibration. Example experimentally measured voltage-transmission calibration plot across an SLM mask.

In order to accurately use the liquid crystal arrays of the SLM to shape pulses, the SLM must be accurately calibrated. First, one must perform a calibration to obtain a defined relationship between applied voltage and transmission for each pixel of the array. Second, one must perform an additional calibration to assign each pixel to a specific wavelength of the input light.

We first describe voltage-transmission calibrations. Each mask of the dual-mask SLM must be calibrated separately. To do this, the mask not in use is set to its maximum voltage, or "open." The mask to be calibrated starts with all pixels set to the minimum voltage. With the same voltage applied to every pixel, the voltage is swept while the pulse shaper output is measured with a spectrometer. The result is shown in Appendix Figure 1.

Wavelength-pixel calibrations are obtained after an initial voltage-transmission calibration. Voltage values are chosen which roughly maximize and minimize the transmission; V_{max} and

V_{min}, respectively. V_{min} is applied across all pixels, then V_{max} is applied to five predetermined pixels. The pulse shaper output is measured with a spectrometer, and the five pixel values are matched to their corresponding wavelength values. A linear fit is performed using these five (pixel, wavelength) pairs, as shown in Appendix Figure 2; the output of this fit constitutes the wavelength calibration.

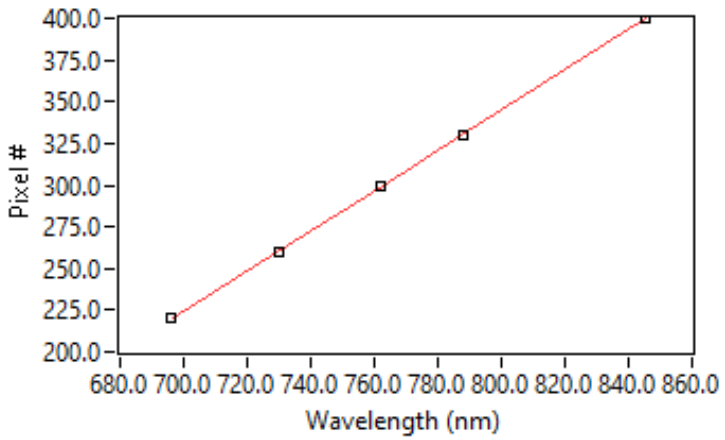

Appendix Figure 2: Wavelength-Pixel Calibration. Example experimentally obtained wavelength calibration.

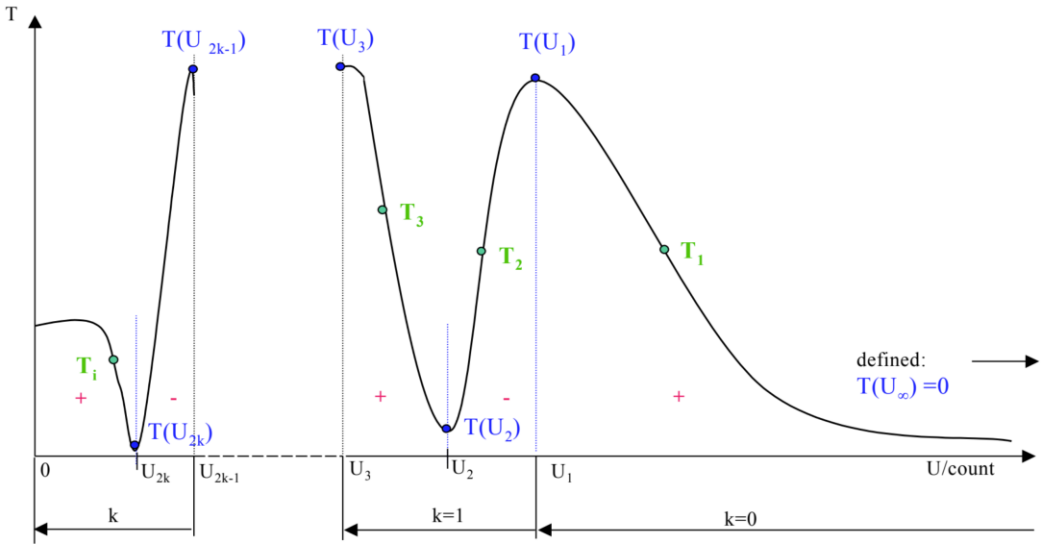

Appendix Figure 3:Ideal voltage-transmission curve.

The SLM voltage/transmission calibration allows us to extract the phase modulation applied by each pixel in each of the two liquid crystal masks. We must find convert the voltage-transmission curve for each pixel (and each mask) to a voltage-phase curve, as shown in Appendix Figure 3. For an ideal voltage-transmission curve, the transmission can be written as

$$T(V) = T_0 \sin^2\left(\frac{\Delta\phi(V)}{2} \pm k\pi\right) \qquad \textbf{Appendix Equation 1}$$

where $k = 0,1,2$ ... This expression can be solved for the phase retardation:

$$\Delta\phi(V) = 2k\pi \pm 2\arcsin\left(\sqrt{\frac{T}{T_0}}\right) \qquad \textbf{Appendix Equation 2}$$

In the ideal case, the transmission graph reaches the value 0 at all of its minima and the same value T at its maxima. For calculation of $\Delta\phi(V)$, the transmission plot must be considered from the right to the left. This means that the calculation has to begin with maximum voltage counts; in our case, the maximum voltage (4095 Counts) is assumed to be close to zero phase retardation. The calculation in practice involves a piecewise function. For example,

$$\Delta\phi(V) = \begin{cases} 0 + 2\arcsin\sqrt{\dfrac{T(V) - 0}{T(V_1) - 0}} & V_1 < V \\ 2\pi - 2\arcsin\sqrt{\dfrac{T(V) - T(V_2)}{T(V_1) - T(V_2)}} & V_2 \le V \le V_1 \\ 2\pi + 2\arcsin\sqrt{\dfrac{T(V) - T(V_3)}{T(V_2) - T(V_3)}} & V_3 \le V \le V_2 \end{cases} \qquad \textbf{Appendix Equation 3}$$

etc. See an ideal transmission curve (Appendix Figure 3) and experimentally measured curve (Appendix Figure 4(a)).

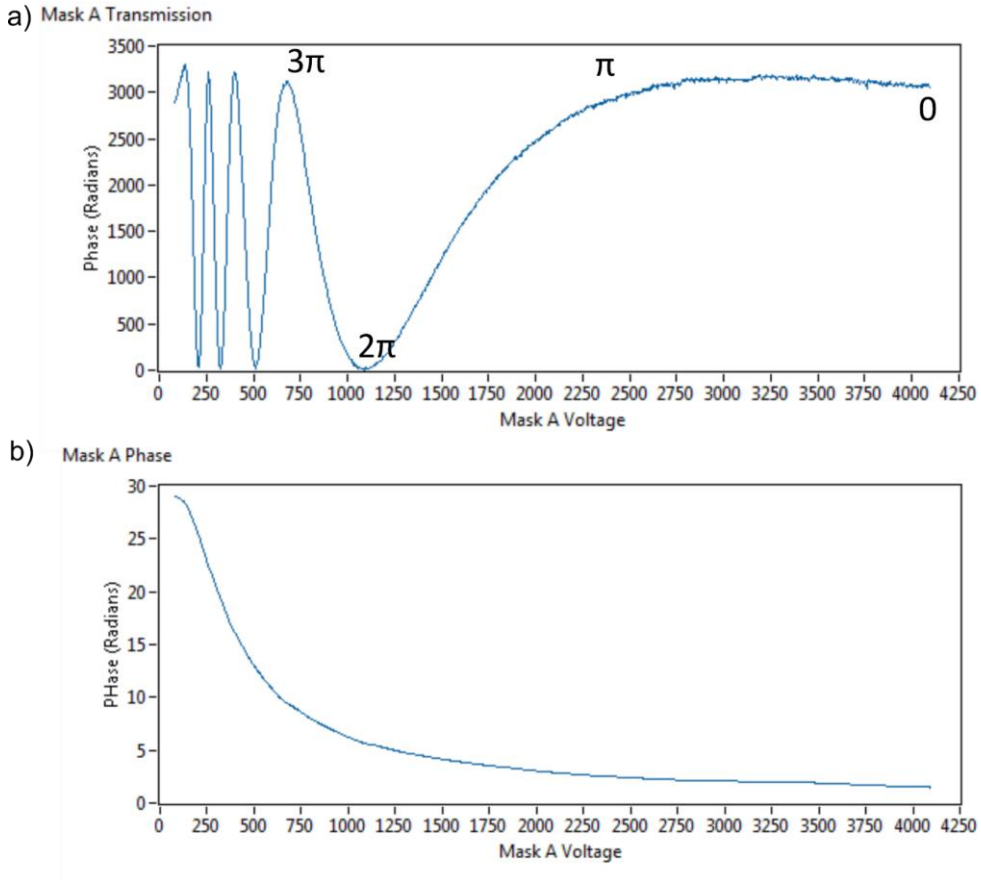

Appendix Figure 4: Transmission-phase conversion. (a) Example voltage-transmission calibration curve for an SLM pixel. (b) Corresponding voltage-phase curve after conversion.

Bibliography

1 Pai, Y.-Y., Tylan-Tyler, A., Irvin, P. & Levy, J. Physics of SrTiO3-based heterostructures and nanostructures: a review. *Reports on Progress in Physics* **81**, 036503, doi:10.1088/1361-6633/aa892d (2018).

2 Benthem, K. v., Elsässer, C. & French, R. H. Bulk electronic structure of SrTiO3: Experiment and theory. *Journal of Applied Physics* **90**, 6156-6164, doi:10.1063/1.1415766 (2001).

3 Whangbo, M.-H., Gordon, E. E., Bettis Jr., J. L., Bussmann-Holder, A. & Köhler, J. Tolerance Factor and Cation–Anion Orbital Interactions Differentiating the Polar and Antiferrodistortive Structures of Perovskite Oxides ABO3. *Zeitschrift für anorganische und allgemeine Chemie* **641**, 1043-1052, doi:https://doi.org/10.1002/zaac.201500058 (2015).

4 Lytle, F. W. X-Ray Diffractometry of Low-Temperature Phase Transformations in Strontium Titanate. *Journal of Applied Physics* **35**, 2212-2215, doi:10.1063/1.1702820 (1964).

5 Shirane, G. & Yamada, Y. Lattice-Dynamical Study of the 110\ifmmode^\circ\else\textdegree\fi{}K Phase Transition in SrTiO3. *Physical Review* **177**, 858-863, doi:10.1103/PhysRev.177.858 (1969).

6 Müller, K. A., Berlinger, W. & Waldner, F. Characteristic Structural Phase Transition in Perovskite-Type Compounds. *Physical Review Letters* **21**, 814-817, doi:10.1103/PhysRevLett.21.814 (1968).

7 Hünnefeld, H. *et al.* Influence of defects on the critical behavior at the 105 K structural phase transition of ${\mathrm{SrTiO}}_{3}:$ On the origin of the two length scale critical fluctuations. *Physical Review B* **66**, 014113, doi:10.1103/PhysRevB.66.014113 (2002).

8 de Lima, B. S. *et al.* Interplay between antiferrodistortive, ferroelectric, and superconducting instabilities in Sr1−xCaxTiO3−δ. *Physical Review B* **91**, 045108, doi:10.1103/PhysRevB.91.045108 (2015).

9 Ariando *et al.* Electronic phase separation at the LaAlO3/SrTiO3 interface. *Nature Communications* **2**, 188, doi:10.1038/ncomms1192 (2011).

10 Caprara, S. *et al.* Multiband superconductivity and nanoscale inhomogeneity at oxide interfaces. *Physical Review B* **88**, 020504, doi:10.1103/PhysRevB.88.020504 (2013).

11 Piskunov, S., Heifets, E., Eglitis, R. I. & Borstel, G. Bulk properties and electronic structure of SrTiO3, BaTiO3, PbTiO3 perovskites: an ab initio HF/DFT study. *Computational Materials Science* **29**, 165-178, doi:https://doi.org/10.1016/j.commatsci.2003.08.036 (2004).

12 Shirai, K. & Yamanaka, K. Mechanism behind the high thermoelectric power factor of SrTiO3 by calculating the transport coefficients. *Journal of Applied Physics* **113**, 053705, doi:10.1063/1.4788809 (2013).

13 Nakamura, R. & Kanematsu, Y. Femtosecond spectral snapshots based on electronic optical Kerr effect. *Review of Scientific Instruments* **75**, 636-644, doi:10.1063/1.1646739 (2004).

14 Kawasaki, M. *et al.* Atomic Control of the SrTiO₃ Crystal Surface. *Science* **266**, 1540-1542, doi:doi:10.1126/science.266.5190.1540 (1994).

15 Rijnders, G. J. H. M., Koster, G., Blank, D. H. A. & Rogalla, H. In situ monitoring during pulsed laser deposition of complex oxides using reflection high energy electron diffraction under high oxygen pressure. *Applied Physics Letters* **70**, 1888-1890, doi:10.1063/1.118687 (1997).

16 Chen, Y. *et al.* Creation of High Mobility Two-Dimensional Electron Gases via Strain Induced Polarization at an Otherwise Nonpolar Complex Oxide Interface. *Nano Letters* **15**, 1849-1854, doi:10.1021/nl504622w (2015).

17 Chen, L. *et al.* Extreme Reconfigurable Nanoelectronics at the CaZrO3/SrTiO3 Interface. *Advanced Materials* **30**, 1801794, doi:https://doi.org/10.1002/adma.201801794 (2018).

18 Niu, W. *et al.* Giant Tunability of the Two-Dimensional Electron Gas at the Interface of γ-Al2O3/SrTiO3. *Nano Letters* **17**, 6878-6885, doi:10.1021/acs.nanolett.7b03209 (2017).

19 Goossens, A. S., Leiviskä, M. A. T. & Banerjee, T. Anisotropy and Current Control of Magnetization in SrRuO3/SrTiO3 Heterostructures for Spin-Memristors. *Frontiers in Nanotechnology* **3**, doi:10.3389/fnano.2021.680468 (2021).

20 Moetakef, P. *et al.* Quantum oscillations from a two-dimensional electron gas at a Mott/band insulator interface. *Applied Physics Letters* **101**, 151604, doi:10.1063/1.4758989 (2012).

21 Ohtomo, A. & Hwang, H. Y. A high-mobility electron gas at the LaAlO3/SrTiO3 heterointerface. *Nature* **427**, 423-426, doi:10.1038/nature02308 (2004).

22 Ron, A. & Dagan, Y. One-Dimensional Quantum Wire Formed at the Boundary between Two Insulating ${\mathrm{LaAlO}}_{3}/{\mathrm{SrTiO}}_{3}$ Interfaces. *Physical Review Letters* **112**, 136801, doi:10.1103/PhysRevLett.112.136801 (2014).

23 Tomczyk, M. *et al.* Micrometer-Scale Ballistic Transport of Electron Pairs in ${\mathrm{LaAlO}}_{3}/{\mathrm{SrTiO}}_{3}$ Nanowires. *Physical Review Letters* **117**, 096801, doi:10.1103/PhysRevLett.117.096801 (2016).

24 Irvin, P. *et al.* Anomalous High Mobility in LaAlO3/SrTiO3 Nanowires. *Nano Letters* **13**, 364-368, doi:10.1021/nl3033729 (2013).

25 Thiel, S., Hammerl, G., Schmehl, A., Schneider, C. W. & Mannhart, J. Tunable Quasi-Two-Dimensional Electron Gases in Oxide Heterostructures. **313**, 1942-1945, doi:10.1126/science.1131091 %J Science (2006).

26 Cen, C. *et al.* Nanoscale control of an interfacial metal–insulator transition at room temperature. *Nature Materials* **7**, 298-302, doi:10.1038/nmat2136 (2008).

27 Li, J. Graphene Complex Oxide Heterostructure. Doctoral Dissertation. (2019).

28 Cen, C., Thiel, S., Mannhart, J. & Levy, J. Oxide Nanoelectronics on Demand. *Science* **323**, 1026-1030, doi:10.1126/science.1168294 (2009).

29 Bi, F. *et al.* "Water-cycle" mechanism for writing and erasing nanostructures at the LaAlO3/SrTiO3 interface. *Applied Physics Letters* **97**, 173110, doi:10.1063/1.3506509 (2010).

30 Bogorin, D. F. *et al.* Nanoscale rectification at the LaAlO3/SrTiO3 interface. *Applied Physics Letters* **97**, 013102, doi:10.1063/1.3459138 (2010).

31 Cheng, G. *et al.* Sketched oxide single-electron transistor. *Nature Nanotechnology* **6**, 343-347, doi:10.1038/nnano.2011.56 (2011).

32 Irvin, P. *et al.* Rewritable nanoscale oxide photodetector. *Nature Photonics* **4**, 849-852, doi:10.1038/nphoton.2010.238 (2010).

33 Ma, Y. *et al.* Broadband Terahertz Generation and Detection at 10 nm Scale. *Nano Letters* **13**, 2884-2888, doi:10.1021/nl401219v (2013).

34 Tang, Y. *et al.* Long-Range Non-Coulombic Electron–Electron Interactions between LaAlO3/SrTiO3 Nanowires. *Advanced Materials Interfaces* **6**, 1900301, doi:https://doi.org/10.1002/admi.201900301 (2019).

35 Cheng, G. *et al.* Shubnikov--de Haas--like Quantum Oscillations in Artificial One-Dimensional LaAlO3/SrTiO3 Electron Channels. *Physical Review Letters* **120**, 076801, doi:10.1103/PhysRevLett.120.076801 (2018).

36 Veazey, J. P. *et al.* Oxide-based platform for reconfigurable superconducting nanoelectronics. *Nanotechnology* **24**, 375201, doi:10.1088/0957-4484/24/37/375201 (2013).

37 Pai, Y.-Y. *et al.* One-Dimensional Nature of Superconductivity at the LaAlO3/SrTiO3 Interface. *Physical Review Letters* **120**, 147001, doi:10.1103/PhysRevLett.120.147001 (2018).

38 Cheng, G. *et al.* Electron pairing without superconductivity. *Nature* **521**, 196-199, doi:10.1038/nature14398 (2015).

39 Briggeman, M. *et al.* Pascal conductance series in ballistic one-dimensional LaAlO3/SrTiO3 channels. *Science* **367**, 769-772, doi:doi:10.1126/science.aat6467 (2020).

40 Briggeman, M. *et al.* One-dimensional Kronig–Penney superlattices at the LaAlO3/SrTiO3 interface. *Nature Physics* **17**, 782-787, doi:10.1038/s41567-021-01217-z (2021).

41 Huang, M. *et al.* Direct imaging of LaAlO3/SrTiO3 nanostructures using piezoresponse force microscopy. *APL Materials* **1**, 052110, doi:10.1063/1.4831855 (2013).

42 Weiner, A. in *Ultrafast Optics* 362-421 (2009).

43 Kalkbrenner, S. SLM-S640d USB Technical Documentation. (2015).

44 Lozovoy, V. V., Pastirk, I. & Dantus, M. Multiphoton intrapulse interference. IV. Ultrashort laser pulse spectral phase characterization and compensation. *Opt. Lett.* **29**, 775-777, doi:10.1364/OL.29.000775 (2004).

45 Xu, B., Gunn, J. M., Cruz, J. M. D., Lozovoy, V. V. & Dantus, M. Quantitative investigation of the multiphoton intrapulse interference phase scan method for simultaneous phase measurement and compensation of femtosecond laser pulses. *J. Opt. Soc. Am. B* **23**, 750-759, doi:10.1364/JOSAB.23.000750 (2006).

46 Kane, D. J. & Trebino, R. Characterization of arbitrary femtosecond pulses using frequency-resolved optical gating. *IEEE Journal of Quantum Electronics* **29**, 571-579, doi:10.1109/3.199311 (1993).

47 Iaconis, C. & Walmsley, I. A. Spectral phase interferometry for direct electric-field reconstruction of ultrashort optical pulses. *Opt. Lett.* **23**, 792-794, doi:10.1364/OL.23.000792 (1998).

48 Gamouras, A., Mathew, R. & Hall, K. C. Optically engineered ultrafast pulses for controlled rotations of exciton qubits in semiconductor quantum dots. *Journal of Applied Physics* **112**, 014313, doi:10.1063/1.4731723 (2012).

49 Ma, Y. Nonlinear Optical Properties of Semiconductor and Oxide Nanostructures. Doctoral Dissertation. (2013).

50 Hu, B. B., Zhang, X. C. & Auston, D. H. Terahertz Radiation Induced by Subband-Gap Femtosecond Optical Excitation of GaAs. *Phys. Rev. Lett.* **67**, 2709 (1991).

51 Hu, B. B., Weling, A. S., Auston, D. H., Kuznetsov, A. V. & Stanton, C. J. DC-electric-field Dependence of THz Radiation Induced by Femtosecond Optical Excitation of Bulk GaAs. *Phys. Rev. B* **49**, 2234 (1994).

52 Leonelli, R. & Brebner, J. L. Time-Resolved Spectroscopy of the Visible Emission Band in Strontium Titanate. *Phys. Rev. B* **33**, 8649-8656 (1986).

53 Kanemitsu, Y. & Yamada, Y. Light Emission from $SrTiO_3$. *Phys. Status Solidi B* **248**, 416-421 (2011).

54 Ristic, Z. *et al.* Photodoping and In-Gap Interface States Across the Metal-Insulator Transition in $LaAlO_3$ / $SrTiO_3$ Heterostructures. *Phys. Rev. B* **86**, 045127 (2012).

55 Kim, M. *et al.* Photoconductivity and Non-exponential Relaxation at Insulating $LaAlO_3$ / $SrTiO_3$ Interfaces. *submitted to Solid State Commun* (2012).

56 Herranz, G. *et al.* Hight Mobility in $LaAlO_3$ / $SrTiO_3$ Heterostructures: Origin, Dimensionality, and Perspectives. *Phys. Rev. Lett.* **98**, 216803 (2007).

57 Kalabukhov, A. *et al.* Effect of Oxygen Vacancies in the $SrTiO_3$ Substrate on the Electrical Properties of the $LaAlO_3$ / $SrTiO_3$ Interface. *Phys. Rev. B* **75**, 121404(R) (2007).

58 Basletic, M. *et al.* Mapping the Spatial Distribution of Charge Carriers in $LaAlO_3$ / $SrTiO_3$ Heterostructures. *Nature Mater.* **7**, 621-625 (2008).

59 Seo, S. S. A. *et al.* Multiple Conducting Carriers Generated in $LaAlO_3$ / $SrTiO_3$ Heterostructures. *Appl. Phys. Lett.* **95**, 082107 (2009).

60 Feng, T. Anomalous Photoelectronic Processes in $SrTiO_3$. *Phys. Rev. B* **25**, 627-642 (1982).

61 Okamura, H. *et al.* Photogenerated Carriers in $SrTiO_3$ Probed by Mid-Infrared Absorption. *J. Phys. Soc. Jpn* **75**, 023703 (2006).

62 Brebner, J. L., Jandl, S. & Lépine, Y. Infrared Defect Absorption in Strontium Titanate. *Phys. Rev. B* **23**, 3816-3822 (1981).

63 Irvin, P. *et al.* Rewritable Nanoscale Oxide Photodetector. *Nature Photon.* **4**, 849-852 (2010).

64 Lytle, F. W. X-Ray Diffractometry of Low-Temperature Phase Transformations in Strontium Titanate. *J. Appl. Phys.* **35**, 2212-2215 (1964).

65 Neville, R. C., Hoeneisen, B. & Mead, C. A. Permittivity of Strontium Titanate. *J. Appl. Phys.* **43**, 2124-2131 (1972).

66 Hemberger, J., Lunkenheimer, P., Viana, R., Böhmer, R. & Loidl, A. Electric-Field-Dependent Dielectric Constant and Nonlinear Susceptibility in $SrTiO_3$. *Phys. Rev. B* **52**, 13159-13162 (1995).

67 Sheridan, E. *et al.* Gate-Tunable Optical Nonlinearities and Extinction in Graphene/LaAlO3/SrTiO3 Nanostructures. *Nano Letters* **20**, 6966-6973, doi:10.1021/acs.nanolett.0c01379 (2020).

68 Novoselov, K. S. *et al.* Electric Field Effect in Atomically Thin Carbon Films. **306**, 666-669, doi:10.1126/science.1102896 %J Science (2004).

69 Nguyen, B. H. & Nguyen, V. H. Advances in graphene-based optoelectronics, plasmonics and photonics. *Advances in Natural Sciences: Nanoscience and Nanotechnology* **7**, 013002, doi:10.1088/2043-6262/7/1/013002 (2016).

70 Romagnoli, M. *et al.* Graphene-based integrated photonics for next-generation datacom and telecom. *Nature Reviews Materials* **3**, 392-414, doi:10.1038/s41578-018-0040-9 (2018).

71 Nair, R. R. *et al.* Fine Structure Constant Defines Visual Transparency of Graphene. *Science* **320**, 1308-1308, doi:10.1126/science.1156965 (2008).

72 Wang, F. *et al.* Gate-Variable Optical Transitions in Graphene. *Science* **320**, 206-209, doi:10.1126/science.1152793 (2008).

73 Li, Z. Q. *et al.* Dirac charge dynamics in graphene by infrared spectroscopy. *Nat Phys* **4**, 532, doi:10.1038/nphys989 (2008).

74 Wassei, J. K. & Kaner, R. B. Graphene, a promising transparent conductor. *Materials Today* **13**, 52-59, doi:https://doi.org/10.1016/S1369-7021(10)70034-1 (2010).

75 Xia, F., Mueller, T., Lin, Y.-m., Valdes-Garcia, A. & Avouris, P. Ultrafast graphene photodetector. *Nat Nanotechnol* **4**, 839-843, doi:10.1038/nnano.2009.292 (2009).

76 Jablan, M., Buljan, H. & Soljačić, M. Plasmonics in graphene at infrared frequencies. *Physical Review B* **80**, 245435, doi:10.1103/PhysRevB.80.245435 (2009).

77 Fang, Z. *et al.* Gated Tunability and Hybridization of Localized Plasmons in Nanostructured Graphene. *ACS Nano* **7**, 2388-2395, doi:10.1021/nn3055835 (2013).

78 Fang, Z. *et al.* Active Tunable Absorption Enhancement with Graphene Nanodisk Arrays. *Nano Lett* **14**, 299-304, doi:10.1021/nl404042h (2014).

79 Thongrattanasiri, S., Koppens, F. H. L. & García de Abajo, F. J. Complete Optical Absorption in Periodically Patterned Graphene. *Physical Review Letters* **108**, 047401, doi:10.1103/PhysRevLett.108.047401 (2012).

80 Grigorenko, A. N., Polini, M. & Novoselov, K. S. Graphene plasmonics. *Nature Photonics* **6**, 749, doi:10.1038/nphoton.2012.262 (2012).

81 Cen, C. *et al.* Nanoscale control of an interfacial metal–insulator transition at room temperature. *Nature Materials* **7**, 298, doi:10.1038/nmat2136 (2008).

82 Schmidt, H., Rode, J. C., Belke, C., Smirnov, D. & Haug, R. J. Mixing of edge states at a bipolar graphene junction. *Physical Review B* **88**, 075418, doi:10.1103/PhysRevB.88.075418 (2013).

83 García de Abajo, F. J. Graphene Plasmonics: Challenges and Opportunities. *Acs Photonics* **1**, 135-152, doi:10.1021/ph400147y (2014).

84 Zhao, B., Zhao, J. M. & Zhang, Z. M. Resonance enhanced absorption in a graphene monolayer using deep metal gratings. *J. Opt. Soc. Am. B* **32**, 1176-1185, doi:10.1364/JOSAB.32.001176 (2015).

85 Hashemi, M., Farzad, M. H., Asger Mortensen, N. & Xiao, S. Enhanced absorption of graphene in the visible region by use of plasmonic nanostructures. *Journal of Optics* **15**, 055003, doi:10.1088/2040-8978/15/5/055003 (2013).

86 Kim, S. *et al.* Electronically Tunable Perfect Absorption in Graphene. *Nano Lett* **18**, 971-979, doi:10.1021/acs.nanolett.7b04393 (2018).

87 Wan, Y. & Deng, L. Modulation and enhancement of optical absorption of graphene-loaded plasmonic hybrid nanostructures in visible and near-infrared regions. *J Appl Phys* **121**, 163102, doi:10.1063/1.4982074 (2017).

88 Huang, M. *et al.* Electric field effects in graphene/LaAlO3/SrTiO3 heterostructures and nanostructures. *APL Materials* **3**, 062502, doi:10.1063/1.4916098 (2015).

89 Li, J. *et al.* Reconfigurable edge-state engineering in graphene using LaAlO3/SrTiO3 nanostructures. *Applied Physics Letters* **114**, 123103, doi:10.1063/1.5080251 (2019).

90 Li, J. *et al.* Reconfigurable edge-state engineering in graphene using LaAlO3/SrTiO3 nanostructures. **114**, 123103, doi:10.1063/1.5080251 (2019).

91 Irvin, P. *et al.* Rewritable nanoscale oxide photodetector. *Nat Photonics* **4**, 849, doi:10.1038/nphoton.2010.238 (2010).

92 Chen, L. *et al.* Over 100-THz bandwidth selective difference frequency generation at LaAlO3/SrTiO3 nanojunctions. *Light: Science & Applications* **8**, 24, doi:10.1038/s41377-019-0135-0 (2019).

93 Jnawali, G. *et al.* Photoconductive response of a single Au nanorod coupled to $LaAlO_3/SrTiO_3$ nanowires. *Applied Physics Letters* **106**, 211101, doi:10.1063/1.4921750 (2015).

94 Wan, M. *et al.* Strong tunable absorption enhancement in graphene using dielectric-metal core-shell resonators. *Scientific Reports* **7**, 32, doi:10.1038/s41598-017-00056-4 (2017).

95 Liu, Y. *et al.* Approaching total absorption at near infrared in a large area monolayer graphene by critical coupling. *Applied Physics Letters* **105**, 181105, doi:10.1063/1.4901181 (2014).

96 Vakil, A. & Engheta, N. Transformation Optics Using Graphene. *Science* **332**, 1291-1294, doi:10.1126/science.1202691 (2011).

97 Freitag, N. M. *et al.* Electrostatically Confined Monolayer Graphene Quantum Dots with Orbital and Valley Splittings. *Nano Lett* **16**, 5798-5805, doi:10.1021/acs.nanolett.6b02548 (2016).

98 Mishchenko, E. G., Shytov, A. V. & Silvestrov, P. G. Guided Plasmons in Graphene $p\mathrm{\text{\ensuremath{-}}}n$ Junctions. *Physical Review Letters* **104**, 156806, doi:10.1103/PhysRevLett.104.156806 (2010).

99 Yu, R. & García de Abajo, F. J. Electrical Detection of Single Graphene Plasmons. *ACS Nano* **10**, 8045-8053, doi:10.1021/acsnano.6b04139 (2016).

100 Cox, J. D. & García de Abajo, F. J. Plasmon-Enhanced Nonlinear Wave Mixing in Nanostructured Graphene. *Acs Photonics* **2**, 306-312, doi:10.1021/ph500424a (2015).

101 Karimi, F. & Knezevic, I. Plasmons in graphene nanoribbons. *Physical Review B* **96**, 125417, doi:10.1103/PhysRevB.96.125417 (2017).

102 Soavi, G. *et al.* Broadband, electrically tunable third-harmonic generation in graphene. *Nat Nanotechnol* **13**, 583-588, doi:10.1038/s41565-018-0145-8 (2018).

103 Jiang, T. *et al.* Gate-tunable third-order nonlinear optical response of massless Dirac fermions in graphene. *Nat Photonics* **12**, 430-436, doi:10.1038/s41566-018-0175-7 (2018).

104 Hendry, E., Hale, P. J., Moger, J., Savchenko, A. K. & Mikhailov, S. A. Coherent Nonlinear Optical Response of Graphene. *Physical Review Letters* **105**, 097401, doi:10.1103/PhysRevLett.105.097401 (2010).

105 Zhang, Y. *et al.* Doping-Induced Second-Harmonic Generation in Centrosymmetric Graphene from Quadrupole Response. *Physical Review Letters* **122**, 047401, doi:10.1103/PhysRevLett.122.047401 (2019).

106 Alexander, K., Savostianova, N. A., Mikhailov, S. A., Kuyken, B. & Van Thourhout, D. Electrically Tunable Optical Nonlinearities in Graphene-Covered SiN Waveguides Characterized by Four-Wave Mixing. *ACS Photonics* **4**, 3039-3044, doi:10.1021/acsphotonics.7b00559 (2017).

107 Bykov, A. Y., Murzina, T. V., Rybin, M. G. & Obraztsova, E. D. Second harmonic generation in multilayer graphene induced by direct electric current. *Physical Review B* **85**, 121413, doi:10.1103/PhysRevB.85.121413 (2012).

108 An, Y. Q., Nelson, F., Lee, J. U. & Diebold, A. C. Enhanced Optical Second-Harmonic Generation from the Current-Biased Graphene/SiO2/Si(001) Structure. *Nano Lett* **13**, 2104-2109, doi:10.1021/nl4004514 (2013).

109 Cheng, J. L., Vermeulen, N. & Sipe, J. E. DC current induced second order optical nonlinearity in graphene. *Opt Express* **22**, 15868-15876, doi:10.1364/OE.22.015868 (2014).

110 Karimi, F., Davoody, A. H. & Knezevic, I. Nonlinear optical response in graphene nanoribbons: The critical role of electron scattering. *Physical Review B* **97**, 245403, doi:10.1103/PhysRevB.97.245403 (2018).

111 Wang, Y. & Andersen, D. R. Third-order terahertz response of gapped, nearly-metallic armchair graphene nanoribbons. *Journal of Physics: Condensed Matter* **28**, 475301, doi:10.1088/0953-8984/28/47/475301 (2016).

112 Cox, J. D., Marini, A. & de Abajo, F. J. G. Plasmon-assisted high-harmonic generation in graphene. *Nature Communications* **8**, 14380, doi:10.1038/ncomms14380 (2017).

113 Cox, J. D. & García de Abajo, F. J. Transient nonlinear plasmonics in nanostructured graphene. *Optica* **5**, 429-433, doi:10.1364/OPTICA.5.000429 (2018).

114 Butscher, S., Milde, F., Hirtschulz, M., Malić, E. & Knorr, A. Hot electron relaxation and phonon dynamics in graphene. *Applied Physics Letters* **91**, 203103, doi:10.1063/1.2809413 (2007).

115 Brida, D. *et al.* Ultrafast collinear scattering and carrier multiplication in graphene. *Nature Communications* **4**, 1987, doi:10.1038/ncomms2987 (2013).

116 Soavi, G. *et al.* Hot Electrons Modulation of Third-Harmonic Generation in Graphene. *ACS Photonics* **6**, 2841-2849, doi:10.1021/acsphotonics.9b00928 (2019).

117 Ma, Q. *et al.* Giant intrinsic photoresponse in pristine graphene. *Nat Nanotechnol* **14**, 145-150, doi:10.1038/s41565-018-0323-8 (2019).

118 Olmon, R. L. & Raschke, M. B. Antenna–load interactions at optical frequencies: impedance matching to quantum systems. *Nanotechnology* **23**, 444001, doi:10.1088/0957-4484/23/44/444001 (2012).

119 Fei, Z. *et al.* Gate-tuning of graphene plasmons revealed by infrared nano-imaging. *Nature* **487**, 82-85, doi:10.1038/nature11253 (2012).

120 Erin Sheridan, G. L., Mamun Sarker, Shan Hao, Ki-Tae Eom, Chang-Beom Eom, Alexander Sinitskii, Patrick Irvin, Jeremy Levy. Gate-Tunable Optical Extinction of Graphene Nanoribbon Nanoclusters. doi:arXiv:2103.07346 (2021).

121 Bolotin, K. I. *et al.* Ultrahigh electron mobility in suspended graphene. *Solid State Communications* **146**, 351-355, doi:https://doi.org/10.1016/j.ssc.2008.02.024 (2008).

122 Pop, E., Varshney, V. & Roy, A. K. Thermal properties of graphene: Fundamentals and applications. *MRS Bulletin* **37**, 1273-1281, doi:10.1557/mrs.2012.203 (2012).

123 Chen, Z., Lin, Y.-M., Rooks, M. J. & Avouris, P. Graphene nano-ribbon electronics. *Physica E: Low-dimensional Systems and Nanostructures* **40**, 228-232, doi:https://doi.org/10.1016/j.physe.2007.06.020 (2007).

124 Celis, A. *et al.* Graphene nanoribbons: fabrication, properties and devices. *Journal of Physics D: Applied Physics* **49**, 143001, doi:10.1088/0022-3727/49/14/143001 (2016).

125 Marmolejo-Tejada, J. M. & Velasco-Medina, J. Review on graphene nanoribbon devices for logic applications. *Microelectronics Journal* **48**, 18-38, doi:https://doi.org/10.1016/j.mejo.2015.11.006 (2016).

126 Jacobse, P. H. *et al.* Electronic components embedded in a single graphene nanoribbon. *Nature Communications* **8**, 119, doi:10.1038/s41467-017-00195-2 (2017).

127 Son, Y.-W., Cohen, M. L. & Louie, S. G. Energy Gaps in Graphene Nanoribbons. *Physical Review Letters* **97**, 216803, doi:10.1103/PhysRevLett.97.216803 (2006).

128 Han, M. Y., Özyilmaz, B., Zhang, Y. & Kim, P. Energy Band-Gap Engineering of Graphene Nanoribbons. *Physical Review Letters* **98**, 206805, doi:10.1103/PhysRevLett.98.206805 (2007).

129 Nakada, K., Fujita, M., Dresselhaus, G. & Dresselhaus, M. S. Edge state in graphene ribbons: Nanometer size effect and edge shape dependence. *Physical Review B* **54**, 17954-17961, doi:10.1103/PhysRevB.54.17954 (1996).

130 Chen, Y.-C. *et al.* Tuning the Band Gap of Graphene Nanoribbons Synthesized from Molecular Precursors. *ACS Nano* **7**, 6123-6128, doi:10.1021/nn401948e (2013).

131 Jänsch, D. *et al.* Ultra-Narrow Low-Bandgap Graphene Nanoribbons from Bromoperylenes—Synthesis and Terahertz-Spectroscopy. *Chemistry – A European Journal* **23**, 4870-4875, doi:https://doi.org/10.1002/chem.201605859 (2017).

132 Barone, V., Hod, O. & Scuseria, G. E. Electronic Structure and Stability of Semiconducting Graphene Nanoribbons. *Nano Letters* **6**, 2748-2754, doi:10.1021/nl0617033 (2006).

133 Cai, J. *et al.* Atomically precise bottom-up fabrication of graphene nanoribbons. *Nature* **466**, 470-473, doi:10.1038/nature09211 (2010).

134 Rizzo, D. J. *et al.* Inducing metallicity in graphene nanoribbons via zero-mode superlattices. *Science* **369**, 1597-1603, doi:10.1126/science.aay3588 (2020).

135 Chung, H.-C., Chang, C.-P., Lin, C.-Y. & Lin, M.-F. Electronic and optical properties of graphene nanoribbons in external fields. *Physical Chemistry Chemical Physics* **18**, 7573-7616, doi:10.1039/C5CP06533J (2016).

136 Ryzhii, V., Mitin, V., Ryzhii, M., Ryabova, N. & Otsuji, T. Device Model for Graphene Nanoribbon Phototransistor. *Applied Physics Express* **1**, 063002, doi:10.1143/apex.1.063002 (2008).

137 Fei, Z. *et al.* Edge and Surface Plasmons in Graphene Nanoribbons. *Nano Letters* **15**, 8271-8276, doi:10.1021/acs.nanolett.5b03834 (2015).

138 Hu, F. *et al.* Imaging the Localized Plasmon Resonance Modes in Graphene Nanoribbons. *Nano Letters* **17**, 5423-5428, doi:10.1021/acs.nanolett.7b02029 (2017).

139 Cox, J. D., Marini, A. & de Abajo, F. J. G. Plasmon-assisted high-harmonic generation in graphene. *Nature Communications* **8**, 14380, doi:10.1038/ncomms14380 (2017).

140 Cox, J. D. & García de Abajo, F. J. Nonlinear Graphene Nanoplasmonics. *Accounts of Chemical Research* **52**, 2536-2547, doi:10.1021/acs.accounts.9b00308 (2019).

141 Cox, J. D., Silveiro, I. & García de Abajo, F. J. Quantum Effects in the Nonlinear Response of Graphene Plasmons. *ACS Nano* **10**, 1995-2003, doi:10.1021/acsnano.5b06110 (2016).

142 Trenti, A. *et al.* in *Quantum Information and Measurement (QIM) V: Quantum Technologies.* T5A.26 (Optical Society of America).

143 Huang, Y. *et al.* Intrinsic Properties of Single Graphene Nanoribbons in Solution: Synthetic and Spectroscopic Studies. *Journal of the American Chemical Society* **140**, 10416-10420, doi:10.1021/jacs.8b06028 (2018).

144 Alonso Calafell, I. *et al.* Quantum computing with graphene plasmons. *npj Quantum Information* **5**, 37, doi:10.1038/s41534-019-0150-2 (2019).

145 Chong, M. C. *et al.* Bright Electroluminescence from Single Graphene Nanoribbon Junctions. *Nano Letters* **18**, 175-181, doi:10.1021/acs.nanolett.7b03797 (2018).

146 Jnawali, G. *et al.* Graphene-Complex-Oxide Nanoscale Device Concepts. *ACS Nano* **12**, 6128-6136, doi:10.1021/acsnano.8b02457 (2018).

147 Liu, X. *et al.* Chevron-type graphene nanoribbons with a reduced energy band gap: Solution synthesis, scanning tunneling microscopy and electrical characterization. *Nano Research* **13**, 1713-1722, doi:10.1007/s12274-020-2797-6 (2020).

148 Radocea, A. *et al.* Solution-Synthesized Chevron Graphene Nanoribbons Exfoliated onto H:Si(100). *Nano Letters* **17**, 170-178, doi:10.1021/acs.nanolett.6b03709 (2017).

149 Piner, R. D., Zhu, J., Xu, F., Hong, S. & Mirkin, C. A. "Dip-Pen" Nanolithography. *Science* **283**, 661-663, doi:10.1126/science.283.5402.661 (1999).

150 Suzuki, T., Levy, J. & Yates, J. T. Localized Deposition of Coronene Molecules on Si(001)-2×1 Using a Scanning Tunneling Microscope Tip Source. *Nano Letters* **6**, 138-143, doi:10.1021/nl0519635 (2006).

151 Kühnle, A., Meyer, G., Hla, S. W. & Rieder, K. H. Understanding atom movement during lateral manipulation with the STM tip using a simple simulation method. *Surface Science* **499**, 15-23, doi:https://doi.org/10.1016/S0039-6028(01)01848-9 (2002).

152 Hla, S.-W. & Rieder, K.-H. STM Control of Chemical Reactions: Single-Molecule Synthesis. *Annual Review of Physical Chemistry* **54**, 307-330, doi:10.1146/annurev.physchem.54.011002.103852 (2003).

153 Eigler, D. M. & Schweizer, E. K. Positioning single atoms with a scanning tunnelling microscope. *Nature* **344**, 524-526, doi:10.1038/344524a0 (1990).

154 Nečas, D. & Klapetek, P. Gwyddion: an open-source software for SPM data analysis. *Central European Journal of Physics* **10**, 181-188, doi:10.2478/s11534-011-0096-2 (2012).

155 Cox, J. D., Yu, R. & García de Abajo, F. J. Analytical description of the nonlinear plasmonic response in nanographene. *Physical Review B* **96**, 045442, doi:10.1103/PhysRevB.96.045442 (2017).

156 Mikhailov, S. A. Theory of the giant plasmon-enhanced second-harmonic generation in graphene and semiconductor two-dimensional electron systems. *Physical Review B* **84**, 045432, doi:10.1103/PhysRevB.84.045432 (2011).

157 Bahk, Y.-M. *et al.* Plasmon Enhanced Terahertz Emission from Single Layer Graphene. *ACS Nano* **8**, 9089-9096, doi:10.1021/nn5025237 (2014).

158 Hammam, A. M. M., Schmidt, M. E., Muruganathan, M. & Mizuta, H. Sharp switching behaviour in graphene nanoribbon p-n junction. *Carbon* **121**, 399-407, doi:https://doi.org/10.1016/j.carbon.2017.05.097 (2017).

159 Llinas, J. P. *et al.* Short-channel field-effect transistors with 9-atom and 13-atom wide graphene nanoribbons. *Nature Communications* **8**, 633, doi:10.1038/s41467-017-00734-x (2017).

160 Yoon, Y. & Salahuddin, S. Dissipative transport in rough edge graphene nanoribbon tunnel transistors. *Applied Physics Letters* **101**, 263501, doi:10.1063/1.4772532 (2012).

161 Yan, Q. *et al.* Intrinsic Current−Voltage Characteristics of Graphene Nanoribbon Transistors and Effect of Edge Doping. *Nano Letters* **7**, 1469-1473, doi:10.1021/nl070133j (2007).

162 Sanz, S., Brandimarte, P., Giedke, G., Sánchez-Portal, D. & Frederiksen, T. Crossed graphene nanoribbons as beam splitters and mirrors for electron quantum optics. *Physical Review B* **102**, 035436, doi:10.1103/PhysRevB.102.035436 (2020).

163 Koch, M., Ample, F., Joachim, C. & Grill, L. Voltage-dependent conductance of a single graphene nanoribbon. *Nature Nanotechnology* **7**, 713-717, doi:10.1038/nnano.2012.169 (2012).

164 Svintsov, D., Vyurkov, V., Ryzhii, V. & Otsuji, T. Voltage-controlled surface plasmon-polaritons in double graphene layer structures. *Journal of Applied Physics* **113**, 053701, doi:10.1063/1.4789818 (2013).

165 Ishii, N. *et al.* Carrier-envelope phase-dependent high harmonic generation in the water window using few-cycle infrared pulses. *Nature Communications* **5**, 3331, doi:10.1038/ncomms4331 (2014).

166 Heide, C., Boolakee, T., Higuchi, T. & Hommelhoff, P. Sub-cycle temporal evolution of light-induced electron dynamics in hexagonal 2D materials. *Journal of Physics: Photonics* **2**, 024004, doi:10.1088/2515-7647/ab7d82 (2020).

167 Yang, D. *et al.* Nanoscale control of LaAlO3/SrTiO3 metal–insulator transition using ultra-low-voltage electron-beam lithography. *Applied Physics Letters* **117**, 253103, doi:10.1063/5.0027480 (2020).